

Effect of Calcium on the Formation and Protectiveness of the Iron Carbonate Layer in  
CO<sub>2</sub> Corrosion

A thesis presented to  
the faculty of  
the Russ College of Engineering and Technology of Ohio University

In partial fulfillment  
of the requirement for the degree Masters of Science

Saba Navabzadeh Esmaeely

August 2013

© 2013 Saba Navabzadeh Esmaeely. All Rights Reserved

This thesis entitled

Effect of Calcium on the Formation and Protectiveness of the Iron Carbonate Layer in

CO<sub>2</sub> Corrosion

by

SABA NAVABZADEH ESMAEELY

has been approved for

the Department of Chemical and Biomolecular Engineering

and the Russ College of Engineering and Technology by

Srdjan Nesic

Professor of Chemical and Biomolecular Engineering

Dennis Irwin

Dean, Russ College of Engineering and Technology

## ABSTRACT

NAVABZADEH ESMAEELY, SABA, M.S., August 2013, Chemical and Biomolecular Engineering

Effect of Calcium on the Formation and Protectiveness of the Iron Carbonate Layer in CO<sub>2</sub> Corrosion (123 pp.)

Director of Thesis: Srdjan Nešić

Due to the isostructurality between calcite ( $\text{CaCO}_3$ ) and siderite ( $\text{FeCO}_3$ ), the  $\text{Ca}^{2+}$  ion incorporates in the hexagonal  $\text{FeCO}_3$  lattice and *vice versa* the  $\text{Fe}^{2+}$  ion incorporates in the hexagonal  $\text{CaCO}_3$  lattice. Thus, in aqueous  $\text{CO}_2$  environments, where both  $\text{Ca}^{2+}$  and  $\text{Fe}^{2+}$  are present, such as in gas reservoirs or deep saline aquifers, following  $\text{CO}_2$  injection, mixed metal carbonates with the formula  $\text{Fe}_x\text{Ca}_y\text{CO}_3$  ( $x+y=1$ ) will be expected to form. This will likely have implications for corrosion, so that corrosion product layers will have the potential to be inhomogeneous, with behavior that deviates from that of pure  $\text{FeCO}_3$ . In the present study, the effect of  $\text{Ca}^{2+}$  on the  $\text{CO}_2$  corrosion behavior of mild steel was investigated with different concentrations of  $\text{Ca}^{2+}$  (10, 100, 1,000 and 10,000 ppm). Electrochemical methods (open circuit potential (OCP) and linear polarization resistance (LPR) measurements) were used to measure the corrosion rate with time. Surface analysis techniques (scanning electron microscopy (SEM), energy dispersive X-ray spectroscopy (EDS) and X-ray diffraction (XRD)), were used to characterize the morphology and composition of the corrosion products. The results showed that with low concentrations of  $\text{Ca}^{2+}$  (10 and 100 ppm), the corrosion rate decreased with time due to the formation of protective  $\text{FeCO}_3$  and/or  $\text{Fe}_x\text{Ca}_y\text{CO}_3$  ( $x + y$

=1). However, the presence of high concentrations of  $\text{Ca}^{2+}$  (1,000 and 10,000 ppm) resulted in the change of corrosion product from protective  $\text{FeCO}_3$  to non-protective  $\text{CaCO}_3$  and  $\text{Fe}_x\text{Ca}_y\text{CO}_3$  ( $x + y = 1$ ) and an increasing corrosion rate with time. While the general corrosion rate was high for both 1,000 and 10,000 ppm  $\text{Ca}^{2+}$ , surface analysis data revealed that localized corrosion was observed in the presence of 10,000 ppm  $\text{Ca}^{2+}$ . Since  $\text{Ca}^{2+}$  was added in the tested conditions as  $\text{CaCl}_2$ , the possible effect of  $\text{Cl}^-$  on the non-uniform attack was studied by testing with the equivalent concentration of  $\text{Cl}^-$  using a  $\text{NaCl}$  solution. However, the result showed that  $\text{Cl}^-$  had no effect on the non-uniform corrosion behavior. Although non-uniform corrosion behavior may be due to many factors, an increasing number of experimental results link the non-homogeneous corrosion product layer to non-uniform corrosion attack. The determination of the relative concentrations of  $\text{Ca}^{2+}$  and  $\text{Fe}^{2+}$  in  $\text{Fe}_x\text{Ca}_y\text{CO}_3$  is of key importance in understanding and predicting the relative properties and stabilities of such mixed metal carbonates. Using Bragg's law and equations to relate interplanar spacings to unit cell parameters, X-ray diffraction (XRD) data can yield precise values for incorporation of  $\text{Ca}^{2+}$  in  $\text{Fe}_x\text{Ca}_y\text{CO}_3$  solid solutions. The results show that as the concentration of  $\text{Ca}^{2+}$  in the structure of this mixed metal carbonate increases the general corrosion rate increases. Non-uniform corrosion behavior was observed with 90% concentration of  $\text{Ca}^{2+}$  in the  $\text{Fe}_x\text{Ca}_y\text{CO}_3$  structure.<sup>1</sup>

---

<sup>1</sup> Elements of this abstract have been reproduced in a paper that was presented at NACE 2013 conference.

**DEDICATION**

*To*

*Parivash Jahanshahi and Heshmat Navabzadeh Esmaeely (my parents)*

*Arash Mojab (my husband)*

*And to*

*All those Iranians who are struggling for freedom and peace in Iran*

## ACKNOWLEDGEMENTS

I would like to sincerely thank my advisor Prof. Srdjan Nešić for his constant support, guidance and understanding during my Masters study at Ohio University. I have always been inspired by his generosity in teaching and supporting his students in all aspects. Under his supervision I have been taught challenges are there to be solved, not to stop me.

I would also like to thank Dr. David Young for supporting me and believing in me even when I did not believe in myself. His friendship kept me sane. I gratefully appreciate his advice on the chemistry aspects of my research.

I would like to take the chance to thank Dr. Yoon-Seok Choi and Mr. Bruce Brown, my project leaders for their invaluable suggestions on my project. The assistance and help of the technicians and especially the lab engineer Mr. Cody Shafer at the Institute for Corrosion and Multiphase Technology (ICMT) is highly appreciated.

I would like to express my appreciation to the committee members, Prof. Kevin Crist and Prof. Lauren McMills for their agreement to be my thesis committee.

I would like to thank the students and staff at ICMT for making me feel supported.

At the end I express my appreciation for the department of Chemical and Biomolecular Engineering for the financial support of my study.

**TABLE OF CONTENTS**

	Page
Abstract .....	3
Dedication .....	5
Acknowledgements .....	6
List of tables .....	9
List of figures .....	10
Chapter 1: Introduction .....	19
Chapter 2: Literature review .....	21
CO <sub>2</sub> Corrosion of mild steel in high pressure CO <sub>2</sub> .....	24
Effect of the brine composition .....	25
Effect of Ca <sup>2+</sup> on corrosion .....	30
Chapter 3: Research objectives and test matrices .....	33
Project objectives and hypotheses .....	33
Experimental setup and test matrixes .....	33
Weight loss measurement procedure .....	41
Pitting corrosion rate measurement procedure .....	41
Effect of calcium concentrations on corrosion .....	42
Effect of pH fluctuation on corrosion in the presence of calcium .....	61

Chloride or calcium; which one is to be blamed for localized attack .....	82
Effect of initial pH at 10,000 ppm Ca <sup>2+</sup> on corrosion behavior .....	93
Quantitative XRD analysis.....	108
Chapter 5: Conclusions and future work .....	113
Conclusions .....	113
Future work .....	113
References.....	115
Appendix 1: Kinetic study of the scale formation .....	121

## LIST OF TABLES

	Page
Table 1. Brine composition (in mg/kg) of Rose Run, Clinton, Mt. Simon and Grand Rapids deep saline aquifers [1]. .....	27
Table 2. Chemical composition carbon steel CS1018 (%, balance Fe). .....	33
Table 3. Experimental parameters for electrochemical measurements. ....	35
Table 4. Test conditions.....	36
Table 5. Test matrix for low to high Ca <sup>2+</sup> concentrations.....	37
Table 6. Test matrix for the effect of Cl <sup>-</sup> .....	38
Table 7. Test matrix for the effect of initial pH.....	39
Table 8. Corresponded data to the tests with 10,000 ppm Ca <sup>2+</sup> with different initial pH. .....	106
Table 9. Composition of the solid solution for the experiments with different initial Ca <sup>2+</sup> . .....	111
Table 10. Composition of the solid for 10,000 ppm Ca <sup>2+</sup> experiments with different initial pH.....	112

## LIST OF FIGURES

	Page
Figure 1. Variation of carbonic species concentration versus pH in an open system with 1.0 bar total pressure at 80°C and pCO <sub>2</sub> 0.5 bar.....	23
Figure 2. Example of a Pourbaix diagram for an Fe-H <sub>2</sub> O system at 80°C;.....	28
Figure 3. Solubility product of CaCO <sub>3</sub> and FeCO <sub>3</sub> at different temperatures.....	29
Figure 4. Experimental setup.....	34
Figure 5. Variations of corrosion rate of CS1018 versus time for 5 experiments with different initial conditions of 0, 10, 100, 1000, 10000 ppm Ca <sup>2+</sup> .....	43
Figure 6. Variations of open circuit potential of CS1018 versus time for 5 experiments with different initial conditions of 0, 10, 100, 1000, 10000 ppm Ca <sup>2+</sup> .....	44
Figure 7. Variations of the bulk pH versus time for 5 experiments with different initial conditions of 0, 10, 100, 1000, 10000 ppm Ca <sup>2+</sup> .....	45
Figure 8. Variations of the bulk Fe <sup>2+</sup> concentration versus time for 5 experiments with different initial conditions of 0, 10, 100, 1000, 10000 ppm Ca <sup>2+</sup> .....	46
Figure 9. Variations of the bulk Fe <sup>2+</sup> and Ca <sup>2+</sup> concentrations versus time for the experiment with the initial 1000 ppm Ca <sup>2+</sup> .....	47
Figure 10. Variations of the FeCO <sub>3</sub> and CaCO <sub>3</sub> saturation degree versus time for the experiment with the initial 1000 ppm Ca <sup>2+</sup> .....	47
Figure 11. Variations of the bulk FeCO <sub>3</sub> saturation degree versus time for 5 experiments with different initial conditions of 0, 10, 100, 1000, 10000 ppm Ca <sup>2+</sup> .....	48

Figure 12. SEM images taken on carbon steel specimen (CS1018) surface of the bulk solution with 10 ppm Fe <sup>2+</sup> (a) no Ca <sup>2+</sup> (b) 10 ppm Ca <sup>2+</sup> (c) 100 ppm Ca <sup>2+</sup> (d) 1,000 ppm Ca <sup>2+</sup> (e) 10,000 ppm Ca <sup>2+</sup> at 80 °C and pCO <sub>2</sub> 0.5 bar after 7 days.....	50
Figure 13. EDS spectra taken on carbon steel specimen (CS1018) surface of the bulk solution with 10 ppm Fe <sup>2+</sup> (a) no Ca <sup>2+</sup> (b) 10 ppm Ca <sup>2+</sup> (c) 100 ppm Ca <sup>2+</sup> (d) 1,000 ppm Ca <sup>2+</sup> (e) 10,000 ppm Ca <sup>2+</sup> at 80 °C and pCO <sub>2</sub> 0.5 bar after 7 days.....	52
Figure 14. XRD data of recovered carbon steel specimen (CS1018) from bulk solution at 80°C and pCO <sub>2</sub> 0.5 bar with 10 ppm Fe <sup>2+</sup> and no Ca <sup>2+</sup> .....	54
Figure 15. XRD data of recovered carbon steel specimen (CS1018) from bulk solution at 80°C and pCO <sub>2</sub> 0.5 bar with 10 ppm Fe <sup>2+</sup> and 10 ppm Ca <sup>2+</sup> .....	54
Figure 16. XRD data of recovered carbon steel specimen (CS1018) from bulk solution at 80°C and pCO <sub>2</sub> 0.5 bar with 10 ppm Fe <sup>2+</sup> and 100 ppm Ca <sup>2+</sup> .....	55
Figure 17. XRD data of recovered carbon steel specimen (CS1018) from bulk solution at 80°C and pCO <sub>2</sub> 0.5 bar with 10 ppm Fe <sup>2+</sup> and 1,000 ppm Ca <sup>2+</sup> .....	55
Figure 18. XRD data of recovered carbon steel specimen (CS1018) from bulk solution at 80°C and pCO <sub>2</sub> 0.5 bar with 10 ppm Fe <sup>2+</sup> and 10,000 ppm Ca <sup>2+</sup> .....	56
Figure 19. Cross section image and EDS spectra taken on carbon steel specimen (CS1018) surface of the bulk solution with 10 ppm Fe <sup>2+</sup> (a) no Ca <sup>2+</sup> (b) 10 ppm Ca <sup>2+</sup> (c) 100 ppm Ca <sup>2+</sup> (d) 10,000 ppm Ca <sup>2+</sup> at 80 °C and pCO <sub>2</sub> 0.5 bar after 7 days.....	58
Figure 20. Surfaces after corrosion product removal of the carbon steel specimen (CS1018) surface of the bulk solution with 10 ppm Fe <sup>2+</sup> (a) no Ca <sup>2+</sup> (b) 10 ppm Ca <sup>2+</sup> (c)	

100 ppm Ca <sup>2+</sup> (d) 1,000 ppm Ca <sup>2+</sup> (e) 10,000 ppm Ca <sup>2+</sup> at 80 °C and pCO <sub>2</sub> 0.5 bar after 7 days.....	60
Figure 21. IFM of carbon steel specimen (CS1018) after removal of corrosion product for the experiment conducted at 80°C and pCO <sub>2</sub> 0.5 bar with 10 ppm Fe <sup>2+</sup> + 10,000ppm Ca <sup>2+</sup> . .....	60
Figure 22. Variations of open circuit potential of carbon steel specimen (CS1018) for the experiments with different initial concentrations of Ca <sup>2+</sup> (0, 10 and 100 ppm).....	62
Figure 23. Variations of corrosion rate of carbon steel specimen (CS1018) for the experiments with different initial concentrations of Ca <sup>2+</sup> (0, 10 and 100 ppm).....	63
Figure 24. Variations of pH of the system for the experiments with different initial concentrations of Ca <sup>2+</sup> (0, 10 and 100 ppm). .....	64
Figure 25. Variations of Fe <sup>2+</sup> concentration of the system for the experiments with different initial concentrations of Ca <sup>2+</sup> (0, 10 and 100 ppm). .....	65
Figure 26. Variation of FeCO <sub>3</sub> saturation degree for the experiments with different initial concentrations of Ca <sup>2+</sup> (0, 10 and 100 ppm). .....	65
Figure 27. SEM images and EDS spectra taken on carbon steel specimen (CS1018) surface of the bulk solution with 10 ppm Fe <sup>2+</sup> and no Ca <sup>2+</sup> at 80 °C and pCO <sub>2</sub> 0.5 bar before changing the pH.....	67
Figure 28. SEM images and EDS spectra taken on carbon steel specimen (CS1018) surface of the bulk solution with 10 ppm Fe <sup>2+</sup> and no Ca <sup>2+</sup> at 80 °C and pCO <sub>2</sub> 0.5 bar after changing the pH.....	68

Figure 29. Cross section image and EDS spectra taken on carbon steel specimen (CS1018) of the bulk solution with 10 ppm $\text{Fe}^{2+}$ and no $\text{Ca}^{2+}$ at 80 °C and $\text{pCO}_2$ 0.5 bar.	69
Figure 30. Surfaces after corrosion product removal of the carbon steel specimen (CS1018) surface of the bulk solution with 10 ppm $\text{Fe}^{2+}$ and no $\text{Ca}^{2+}$ at 80 °C and $\text{pCO}_2$ 0.5 bar.	70
Figure 31. SEM images and EDS spectra taken on carbon steel specimen (CS1018) surface of the bulk solution with 10 ppm $\text{Fe}^{2+}$ and 10 ppm $\text{Ca}^{2+}$ at 80 °C and $\text{pCO}_2$ 0.5 bar before changing the pH.	71
Figure 32. SEM images and EDS spectra taken on carbon steel specimen (CS1018) surface of the bulk solution with 10 ppm $\text{Fe}^{2+}$ and 10 ppm $\text{Ca}^{2+}$ at 80 °C and $\text{pCO}_2$ 0.5 bar after the 1 <sup>st</sup> drop in the pH.	73
Figure 33. SEM images and EDS spectra taken on carbon steel specimen (CS1018) surface of the bulk solution with 10 ppm $\text{Fe}^{2+}$ and 10 ppm $\text{Ca}^{2+}$ at 80 °C and $\text{pCO}_2$ 0.5 bar after the 2 <sup>nd</sup> drop in the pH.	74
Figure 34. Cross section image and EDS spectra taken on carbon steel specimen (CS1018) of the bulk solution with 10 ppm $\text{Fe}^{2+}$ and 10 ppm $\text{Ca}^{2+}$ at 80 °C and $\text{pCO}_2$ 0.5 .	75
Figure 35. Surfaces after corrosion product removal of the carbon steel specimen (CS1018) surface of the bulk solution with 10 ppm $\text{Fe}^{2+}$ and 10 ppm $\text{Ca}^{2+}$ at 80 °C and $\text{pCO}_2$ 0.5 bar	76

Figure 36. SEM images and EDS spectra taken on carbon steel specimen (CS1018) surface of the bulk solution with 10 ppm $\text{Fe}^{2+}$ and 100 ppm $\text{Ca}^{2+}$ at 80 °C and $\text{pCO}_2$ 0.5 bar before changing the pH.....	78
Figure 37. SEM images and EDS spectra taken on carbon steel specimen (CS1018) surface of the bulk solution with 10 ppm $\text{Fe}^{2+}$ and 100 ppm $\text{Ca}^{2+}$ at 80 °C and $\text{pCO}_2$ 0.5 bar after the 1 <sup>st</sup> drop in the pH .....	79
Figure 38. SEM images and EDS spectra taken on carbon steel specimen (CS1018) surface of the bulk solution with 10 ppm $\text{Fe}^{2+}$ and 100 ppm $\text{Ca}^{2+}$ at 80 °C and $\text{pCO}_2$ 0.5 bar after the 2 <sup>nd</sup> drop in the pH .....	80
Figure 39. Cross section image and EDS spectra taken on carbon steel specimen (CS1018) of the bulk solution with 10 ppm $\text{Fe}^{2+}$ and 100 ppm $\text{Ca}^{2+}$ at 80 °C and $\text{pCO}_2$ 0.5.....	81
Figure 40. Surfaces after corrosion product removal of the carbon steel specimen (CS1018) surface of the bulk solution with 10 ppm $\text{Fe}^{2+}$ and 100 ppm $\text{Ca}^{2+}$ at 80 °C and $\text{pCO}_2$ 0.5 bar.....	82
Figure 41. Variations of corrosion rate versus time of carbon steel specimen (CS1018) for two experiments with different initial concentrations of $\text{Ca}^{2+}$ (0 and 10,000 ppm) and the same $[\text{Cl}^-]$ .....	84
Figure 42. Variations of open circuit potential versus time of carbon steel specimen (CS1018) for two experiments with different initial concentrations of $\text{Ca}^{2+}$ (0 and 10,000 ppm) and the same $[\text{Cl}^-]$ .....	85

Figure 43. Variations of pH of the system for two experiments with different initial concentrations of $\text{Ca}^{2+}$ (0 and 10,000 ppm) and the same $[\text{Cl}^-]$ .....	86
Figure 44. Variations of $\text{Fe}^{2+}$ concentration of the system for two experiments with different initial concentrations of $\text{Ca}^{2+}$ (0 and 10,000 ppm) and the same $[\text{Cl}^-]$ .....	87
Figure 45. Variations of $\text{FeCO}_3$ saturation degree of the system for two experiments with different initial concentrations of $\text{Ca}^{2+}$ (0 and 10,000 ppm) and the same $[\text{Cl}^-]$ .....	87
Figure 46. SEM images taken on carbon steel specimen (CS1018) surface of the bulk solution with (a) 4wt% NaCl (b) 10 ppm $\text{Fe}^{2+}$ and 10,000 ppm $\text{Ca}^{2+}$ at 80 °C and $\text{pCO}_2$ 0.5 bar after 6 days.....	89
Figure 47. EDS spectra taken on carbon steel specimen (CS1018) surface of the bulk solution with (a) 4wt% NaCl (b) 10 ppm $\text{Fe}^{2+}$ and 10,000 ppm $\text{Ca}^{2+}$ at 80 °C and $\text{pCO}_2$ 0.5 bar after 6 days.....	90
Figure 48. Cross section image taken on carbon steel specimen (CS1018) of the bulk solution with (a) 4wt% NaCl (b) 10 ppm $\text{Fe}^{2+}$ and 10,000 ppm $\text{Ca}^{2+}$ at 80 °C and $\text{pCO}_2$ 0.5 bar after 6 days.....	91
Figure 49. Surfaces after corrosion product removal of the carbon steel specimen (CS1018) surface of the bulk solution with (a) 4wt% NaCl (b) 10 ppm $\text{Fe}^{2+}$ and 10,000 ppm $\text{Ca}^{2+}$ at 80 °C and $\text{pCO}_2$ 0.5 bar.....	92
Figure 50. Variations of open circuit potential of carbon steel specimen (CS1018) for the experiments with 10,000 ppm $\text{Ca}^{2+}$ at different initial pH (pH 6.6 or pH 5.3).....	94
Figure 51. Corrosion rate versus time of carbon steel specimen (CS1018) for the experiments with 10,000 ppm $\text{Ca}^{2+}$ at different initial pH (pH 6.6 or pH 5.3).....	94

Figure 52. Variations of pH of the system for the experiments with 10,000 ppm Ca <sup>2+</sup> at different initial pH (pH 6.6 or pH 5.3).....	95
Figure 53. Variations of Fe <sup>2+</sup> concentration of the system for the experiments with 10,000 ppm Ca <sup>2+</sup> at different initial pH (pH 6.6 or pH 5.3). ..	96
Figure 54. Variations of degree of FeCO <sub>3</sub> saturation of the system for the experiments with 10,000 ppm Ca <sup>2+</sup> at different initial pH (pH 6.6 or pH 5.3). .....	96
Figure 55. Variations of Ca <sup>2+</sup> concentration of the system for the experiments with 10,000 ppm Ca <sup>2+</sup> at different initial pH (pH 6.6 or pH 5.3). .....	98
Figure 56. Variations of degree of CaCO <sub>3</sub> saturation of the system for the experiments with 10,000 ppm Ca <sup>2+</sup> at different initial pH (pH 6.6 or pH 5.3). .....	98
Figure 57. SEM images taken on carbon steel specimen (CS1018) surface of the bulk solution with 10,000 ppm Ca <sup>2+</sup> and initial pH 5.3 at 80°C and pCO <sub>2</sub> 0.5 .....	100
Figure 58. EDS spectra taken on carbon steel specimen (CS1018) surface of the bulk solution with 10,000 ppm Ca <sup>2+</sup> and initial pH 5.3 at 80°C and pCO <sub>2</sub> 0.5 .....	101
Figure 59. SEM images taken on carbon steel specimen (CS1018) surface of the bulk solution with 10,000 ppm Ca <sup>2+</sup> at 80°C and pCO <sub>2</sub> 0.5 bar (a) initial pH 6.6 (b) initial pH 5.3 .....	102
Figure 60. EDS spectra taken on carbon steel specimen (CS1018) surface of the bulk solution at 80°C and pCO <sub>2</sub> 0.5 bar with 10,000 ppm Ca <sup>2+</sup> (a) pH 6.6 (b) and pH 5.3....	103
Figure 61. Cross section image taken on carbon steel specimen (CS1018) of the bulk solution at 80°C and pCO <sub>2</sub> 0.5 bar with 10000 ppm Ca <sup>2+</sup> (a) pH 6.6 (b) and pH 5.3. ....	104

Figure 62. Surfaces after corrosion product removal of the carbon steel specimen (CS1018) surface of the bulk solution at 80°C and pCO <sub>2</sub> 0.5 bar with 10,000 ppm Ca <sup>2+</sup> (a) pH 6.6 (b) and pH 5.3 .....	105
Figure 63. IFM of carbon steel specimen (CS1018) after removal of corrosion product for the experiment conducted at 80°C and pCO <sub>2</sub> 0.5 bar with different initial pH (a) pH 6.6 (b) pH 5.3 .....	106
Figure 64. XRD data of recovered carbon steel specimen (CS1018) from bulk solution at 80°C and pCO <sub>2</sub> 0.5 bar with 10,000 ppm Ca <sup>2+</sup> with initial pH 6.6 .....	107
Figure 65. XRD data of recovered carbon steel specimen (CS1018) from bulk solution at 80°C and pCO <sub>2</sub> 0.5 bar with 10,000 ppm Ca <sup>2+</sup> with initial pH 5.3 .....	107
Figure 66. lattice image of (a) calcite (CaCO <sub>3</sub> ; blue = Ca, red = O, black =C) (b) siderite (FeCO <sub>3</sub> ; tan = Fe, red = O, black =C).....	109
Figure 67. Hexagonal unit cell.....	110
Figure 68. Unit cell parameter c versus the concentration of Ca <sup>2+</sup> in the structure of solid solution for experiments with different initial conditions of 0, 10, 100, 1000, 10000 ppm Ca <sup>2+</sup> .....	110
Figure 69. Unit cell parameter “c” versus concentration of Ca <sup>2+</sup> in the structure of corrosion products for experiments with 10,000 ppm Ca <sup>2+</sup> and initial pH values of 5.3 and 6.6.....	112
Figure 70. SEM images taken on carbon steel specimen (CS1018) surface of the bulk solution with 10,000 ppm Ca <sup>2+</sup> and initial pH 6.6 at 80°C, pCO <sub>2</sub> 0.5 bar and 10 ppm Fe <sup>2+</sup> and 1,000 ppm Ca <sup>2+</sup> (a) after 4 days, (b) after 7 days.....	122

Figure 71. XRD data taken on carbon steel specimen (CS1018) surface of the bulk solution with 10,000 ppm  $\text{Ca}^{2+}$  and initial pH 6.6 at 80°C,  $\text{pCO}_2$  0.5 bar and 10 ppm  $\text{Fe}^{2+}$

and 1,000 ppm  $\text{Ca}^{2+}$  after 4 days..... 122

Figure 72. XRD data taken on carbon steel specimen (CS1018) surface of the bulk solution with 10,000 ppm  $\text{Ca}^{2+}$  and initial pH 6.6 at 80°C,  $\text{pCO}_2$  0.5 bar and 10 ppm  $\text{Fe}^{2+}$

and 1,000 ppm  $\text{Ca}^{2+}$  after 7 days..... 123

## CHAPTER 1: INTRODUCTION

$\text{CO}_2$  corrosion of mild steel has been studied in laboratory and field operating conditions over the past several decades. In reality, corrosion happens in brines with complicated chemistries, but most of the lab studies have been done in various dilute solutions of  $\text{NaCl}$ . In addition to  $\text{Na}^+$  and  $\text{Cl}^-$ , there are many other ions in the brine. Cations which can form various carbonate layers have the potential to play a major role in the corrosion behavior of mild steel, particularly downhole. Among these cations,  $\text{Ca}^{2+}$  and  $\text{Mg}^{2+}$  are usually found at the highest concentration in reservoir fluids [1]. These two cations can change the mechanism of the corrosion process since their carbonate crystal structures, calcite and magnesite, are isomorphous with siderite ( $\text{FeCO}_3$ ). Thus, they have the potential to change the morphology, composition and physicochemical properties of  $\text{FeCO}_3$  by substitution into the metal ion positions of the  $\text{FeCO}_3$  crystal structure [2]. The formation and protectiveness of  $\text{FeCO}_3$  is known to have a significant role in  $\text{CO}_2$  corrosion processes for mild steel, but effects of  $\text{Ca}^{2+}$  on corrosion mechanisms have not been well documented.

Increasing oil demand has led to considerable investment in and implementation of enhanced oil recovery (EOR) systems, including using  $\text{CO}_2$ . On the other hand, the threat of global climate change, hypothesized to be related to anthropogenic  $\text{CO}_2$  emissions, has become one of the most serious concerns of the 21<sup>st</sup> Century. Major research efforts are underway to understand how it occurs and to develop ways to mitigate its impact on the environment. Since  $\text{CO}_2$  emission is directly proportional to fossil fuel consumption, the capturing and subsequent geologic storage of  $\text{CO}_2$  is a

candidate technology for controlling its emission. The carbon capture and storage (CCS) process contains three stages: CO<sub>2</sub> capture at its generation source (coal or gas fired power plant, refinery, syngas unit, cement works or some other industrial process), transportation to the geologic storage site (usually by pipeline transmission) followed by injection into geologic host reservoirs [3]. This bears a striking similarity to the utilization of CO<sub>2</sub> for EOR.

Research activities largely concentrate on development of the capture technologies to reduce the cost, and on assessing the technical feasibility of injecting and monitoring the CO<sub>2</sub> within the geological reservoirs themselves. Little work is being conducted which identifies and quantifies corrosion damage to structures and facilities in CCS systems, but this remains a critical component that should not be overlooked. For example, corrosion is one of the largest concerns for the sequestration of CO<sub>2</sub> in deep geologic formation [4] since it can lead to loss of wellbore integrity and consequent leakage of sequestered CO<sub>2</sub>. This is a key part of any risk assessment relating to CCS implementation.

Brine chemistry has a considerable effect on both CO<sub>2</sub>-EOR and CO<sub>2</sub> storage in deep saline aquifers. Therefore, the effect of Ca<sup>2+</sup> on the formation and protectiveness of FeCO<sub>3</sub> is studied in this research.

## CHAPTER 2: LITERATURE REVIEW

There are several options for capturing and storing CO<sub>2</sub>. Among these options, the injection and storage of CO<sub>2</sub> in deep saline aquifers, similarly to CO<sub>2</sub>-based enhanced oil recovery, has the potential to lead to severe casing corrosion. With smaller quantities of water in other environments corrosion may not be as critical an issue. Since casing corrosion leads to loss of wellbore integrity, the focus of this study is on casing corrosion while injecting and storing CO<sub>2</sub> in deep saline aquifers and related enhanced oil recovery processes.

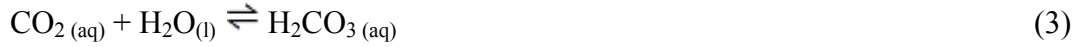
In the oil and gas industry, CO<sub>2</sub> corrosion has been widely studied over several decades [4]. The difference in CO<sub>2</sub> injection is that the process involves a very high pressure of CO<sub>2</sub> that is in direct contact with the saline aquifer. In a recent publication, Pfennig and Kranzmann stated that the “interface of the cap rock and the reservoir where the brine may be in contact with the casing and tubing is the most susceptible part to corrosion (injection pipe)” [4]. If casing is always exposed to the corrosive environment [4] with the high pressure CO<sub>2</sub>, in addition to a considerable amount of brine, severe corrosion is expected. Such a situation would occur if cementing within the annular space was somehow compromised [5]. Table 1 shows brine compositions for four different deep saline aquifers from the Rose Run, Clinton, Mt. Simon and Grand Rapids geologic formations. These brines typically reside in sandstones of varying porosity. Since the corrosion rate of casing steel is dependent on the formation of iron carbonate (FeCO<sub>3</sub>), those brine species which can form a carbonate layer are very important in a corrosion study as they can compete with Fe<sup>2+</sup> in formation of carbonate and there is a possibility of

changing the corrosion product morphology and its physicochemical characteristics.

According to Table 1, the listed brines have a high concentration of  $\text{Ca}^{2+}$ . If  $\text{CO}_2$  is injected into such aquifers then it will become saturated with respect to the  $\text{CaCO}_3$  precipitation, with potential deposition as scale on a corroding steel surface.

$\text{CO}_2$  corrosion of mild steel is a function of several factors such as temperature,  $\text{CO}_2$  partial pressure, pH, flow, presence of organic acids, the composition and the concentration of aqueous salts in brine [6].

The  $\text{CO}_2$  corrosion mechanism in aqueous solution is affected by the following homogeneous and heterogeneous chemical reactions [6]:



The equilibrium concentration of species can be calculated by writing the equilibria expressions for reactions (1) to (5) [7]:

$$K_{sol} = \frac{C_{CO_2}}{p_{CO_2}} \quad (7)$$

$$K_{wa} = C_{H^+} C_{OH^-} \quad (8)$$

$$K_{hy} = \frac{C_{H_2CO_3}}{C_{CO_2}} \quad (9)$$

$$K_{ca} = \frac{C_{H^+} C_{HCO_3^-}}{C_{H_2CO_3}} \quad (10)$$

$$K_{bi} = \frac{C_{H^+} C_{CO_3^{2-}}}{C_{HCO_3^-}} \quad (11)$$

and considering the charge balance (electroneutrality) expression.

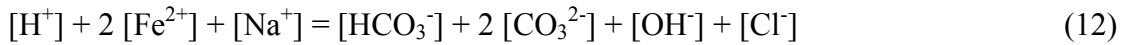


Figure 1 shows the carbonic species variation vs. pH value for an open system with CO<sub>2</sub> partial pressure of 0.5 bar. [7]

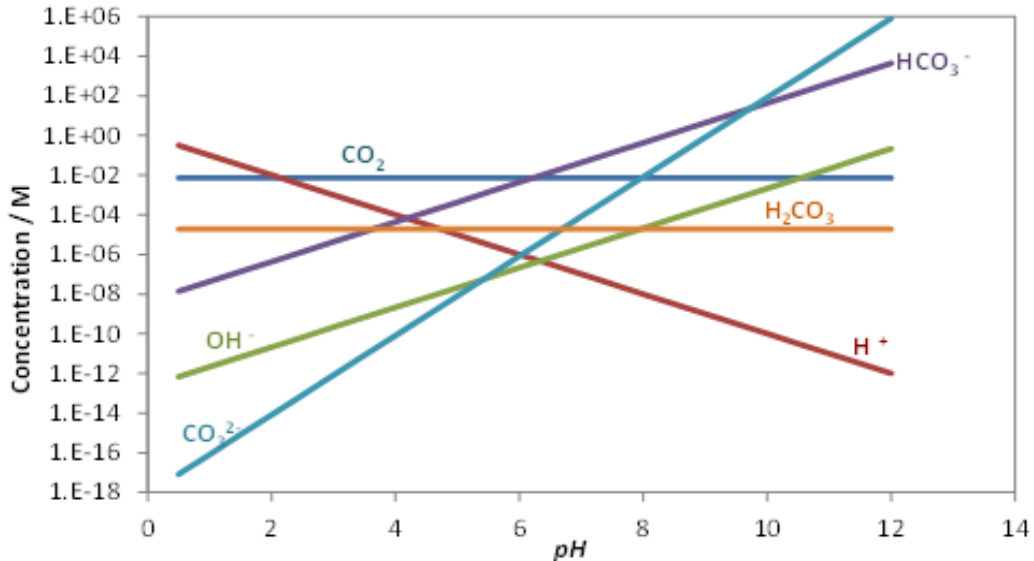


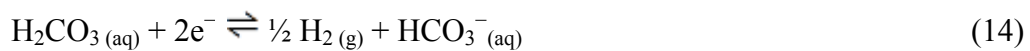
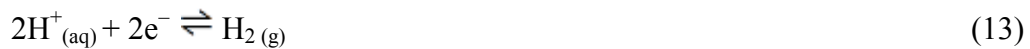
Figure 1. Variation of carbonic species concentration versus pH in an open system with 1.0 bar total pressure at 80°C and pCO<sub>2</sub> 0.5 bar.

As pointed-out earlier, the composition and concentration of salts in brine have a dramatic effect on the corrosion behavior of casing steel. The presence of different

species in brines can change the corrosion process in several ways; one way is by ionic strength effects. The other possible effect may be due to the presence cations other than  $\text{Fe}^{2+}$  which have the ability to form carbonate layers. Thus, the  $\text{FeCO}_3$  formation can be perturbed or altered by the newly formed metal carbonates. This will be discussed in more detail below.

### **CO<sub>2</sub> Corrosion of mild steel in high pressure CO<sub>2</sub>**

Some studies have been performed on CO<sub>2</sub> corrosion at high pressures. Studies conducted at 70 bar CO<sub>2</sub> [8], [9] showed that the initial corrosion rate is high (above 10mm/y). For high pressure CO<sub>2</sub> in wet environments, due to generation of excessive amounts of carbonic acid ( $\text{H}_2\text{CO}_3$ ) and its consequent dissociation, the concentration of hydrogen ions ( $[\text{H}^+]$ ) is high. This provides species for a cathodic reaction, as shown in Reaction (13). The direct reduction of H<sub>2</sub>CO<sub>3</sub>, Reaction (14), can increase the corrosion rate by acting as another oxidant [8].



When the system reaches a favorable condition for the formation of FeCO<sub>3</sub>, the corrosion rate decreases due to the formation of protective FeCO<sub>3</sub> [9]. Even though the bulk pH may be very low in high pressure CO<sub>2</sub> (as low as pH3.1), there is a high concentration of  $\text{Fe}^{2+}$  near the surface because of the high corrosion rate. This creates favorable conditions for heterogeneous nucleation of FeCO<sub>3</sub> and its crystal growth.

The corrosion protection conferred by FeCO<sub>3</sub> is highly dependent on its growth rate [10], if the rate of corrosion is higher than FeCO<sub>3</sub> formation then it won't be

protective [6]. Consequently any phenomena that can change the rate of  $\text{FeCO}_3$  formation/precipitation can change the corrosion behavior. Furthermore, the protectiveness of the  $\text{FeCO}_3$  layer is independent of its thickness; rather it is related to the porosity and steel surface coverage by the corrosion product layer. Good protection implies lesser porosity/better coverage, and *vice versa* [10],[11].

### **Effect of the brine composition**

The effect of  $\text{FeCO}_3$  on corrosion has been a common area of research over the past several decades. [11–16] The protective effect of an adhesive and dense layer of  $\text{FeCO}_3$  was described by Nesić [6]. Formation of  $\text{FeCO}_3$  has the potential to block the surface area and retard the corrosion processes. When the  $\text{FeCO}_3$  saturation degree gets higher than unity (supersaturated), the precipitation of  $\text{FeCO}_3$  becomes possible, particularly heterogeneously through its nucleation on the steel surface. To form a dense and protective  $\text{FeCO}_3$  the saturation degree should be significantly larger than unity [6]. The saturation degree is calculated from the known concentration of  $\text{Fe}^{2+}$  and  $\text{CO}_3^{2-}$  [16], as shown in Equation (15) , with the  $\text{FeCO}_3$  solubility product ( $K_{\text{SP}}$ ) calculated according to Equation (16) [17]. Note that, the concentration of  $\text{CO}_3^{2-}$  is calculated from a known pH by using an equilibrium model for aqueous  $\text{CO}_2$  species [18].

$$S_{\text{FeCO}_3} = \frac{C_{\text{Fe}^{2+}} * C_{\text{CO}_3^{2-}}}{K_{\text{SP},\text{FeCO}_3}} \quad (15)$$

$$\begin{aligned} \text{Log}K_{\text{SP},\text{FeCO}_3} = & -59.3498 - 0.041377 * T - \frac{2.11963}{T} + 24.5724 \text{Log}(T) \\ & + 2.518 * I^{0.5} - 0.6578 * I \end{aligned} \quad (7)$$

The  $\text{FeCO}_3$  layer is not always protective, to be so it needs to be dense and adherent to the steel surface, providing good coverage [6]. At higher temperatures and pH in pure  $\text{NaCl}$  solution the formation of a protective  $\text{FeCO}_3$  is likely due to the high concentration of  $\text{CO}_3^{2-}$  and accelerated chemical reactions because of the elevated temperature [6];  $\text{FeCO}_3$  solubility also decreases with temperature. The protectiveness of  $\text{FeCO}_3$  is determined by both the mechanical and chemical properties of the layer. Thus, many studies have been done related to these properties [19–22].  $\text{FeCO}_3$  formation and protectiveness are subjected to change due to different environmental parameters. [6], [23] The mechanical and chemical properties of the corrosion product layer change as a result of temperature, saturation degree and brine chemical compositions.[23–25] An enhancement in the protective properties of the corrosion product layer was reported by Ingham, *et al.*, in the presence of a small amount of  $\text{MgCl}_2$ . [25]

As noted earlier,  $\text{Ca}^{2+}$  should play an important role in  $\text{CO}_2$  corrosion due to the  $\text{CaCO}_3$  isostructurality [2] with  $\text{FeCO}_3$ . In the presence of  $\text{Ca}^{2+}$  the formation of a solid solution is more probable than the formation of pure  $\text{FeCO}_3$  [2][26] as shown in Reaction (18). Figure 2 shows the species stability diagram known as Pourbaix diagram<sup>2</sup> for  $\text{Fe}-\text{H}_2\text{O}$  system in the absence of  $\text{Ca}^{2+}$ . Depending upon pH and corrosion potential  $\text{FeCO}_3$  may form on the surface and stays stable. However,  $\text{Ca}^{2+}$  changes the nature of corrosion product and makes the Pourbaix diagram more complicated. According to Table 1, the listed brines have high concentration of  $\text{Ca}^{2+}$ . The morphology and chemical properties of  $\text{FeCO}_3$  would be expected to change in the presence of  $\text{Ca}^{2+}$ . Thus, the degree and nature

---

<sup>2</sup> Pourbaix diagram courtesy of Tanaporn Tanupabungsun

of  $\text{Ca}^{2+}$  substitution for  $\text{Fe}^{2+}$  into the  $\text{FeCO}_3$  would be expected to govern its protectiveness [27], [28]; this was the initial research hypothesis in the present work. Although effects of many parameters on the formation and protectiveness of  $\text{FeCO}_3$  have been studied [6], [10], [15], [23], [27–29], the effect of individual species in the brine has not been thoroughly addressed. [25] One such species is  $\text{Ca}^{2+}$ .

Table 1. Brine compositon (in mg/kg) of Rose Run, Clinton, Mt. Simon and Grand Rapids deep saline aquifers [1].

Ion	Rose Run	Clinton	Mt. Simon (mg/kg)	Grand Rapids
$\text{Na}^+$	60122	67000	32000	26539
$\text{K}^+$	3354	850	1060	636
$\text{Ca}^{2+}$	37600	23200	12400	2737
$\text{Mg}^{2+}$	5880.6	1840	2190	533
$\text{Sr}^{2+}$	455.52	753	236	-
$\text{Fe}^{2+}$	140	5	1.54	4.6E-5
$\text{Cl}^-$	191203	160400	78700	47549
$\text{Br}^-$	3760	-	362	-
$\text{SO}_4^{2-}$	326.4	523	1180	337
$\text{HCO}_3^-$	122	200	71	182
TDS	277571	250000	150000	90000
pH	6.4	6.5	6.65	7.2

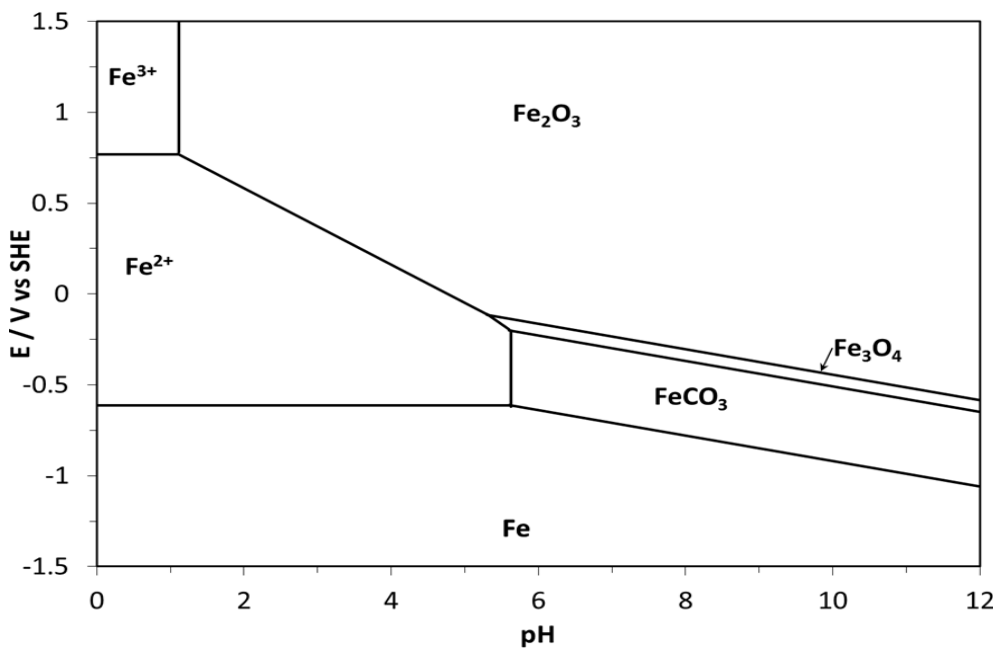
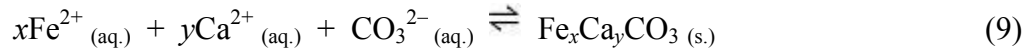


Figure 2. Example of a Pourbaix diagram for an Fe-H<sub>2</sub>O system at 80°C;  
 $C_{Fe^{2+}} = 10$  ppm,  $pCO_2 = 0.5$  bar.

In a system with high Ca<sup>2+</sup> concentration, formation of FeCO<sub>3</sub> becomes difficult.

In an open system, due to the formation of CaCO<sub>3</sub>, as shown in Reaction (12), the pH can drop due to the imposed imbalance in the electroneutrality relationship as shown in Equation (12); this is presented in a revised form as Equation (19) to account for the presence of Ca<sup>2+</sup> in the solution. This imposed imbalance affects the dissociation of H<sub>2</sub>CO<sub>3</sub> and HCO<sub>3</sub><sup>-</sup>, according to Reaction (4) and (5) [18],[7] and adversely affects the formation of FeCO<sub>3</sub>. In closed systems most of the CO<sub>3</sub><sup>2-</sup> can be consumed by the formation of CaCO<sub>3</sub>. Even though the K<sub>SP</sub> of CaCO<sub>3</sub>, calculated from Reaction (21) [30], is around 2 orders of magnitude larger than the K<sub>SP</sub> of FeCO<sub>3</sub> in Equation (16) [17], it should be taken into consideration as the concentration of Ca<sup>2+</sup> can be very high; thus it

can easily get above the saturation degree. Figure 3 shows the plotted  $K_{SP}$  values for  $\text{CaCO}_3$  and  $\text{FeCO}_3$  *versus* temperature.



$$S_{\text{CaCO}_3} = \frac{C_{\text{Ca}^{2+}} * C_{\text{CO}_3^{2-}}}{K_{SP,\text{CaCO}_3}} \quad (11)$$

$$\begin{aligned} \log K_{SP,\text{CaCO}_3} = & -1128.732 - 0.2994444 * T - \frac{35512.75}{T} \\ & + 485.818 \log(T) \end{aligned} \quad (21)$$

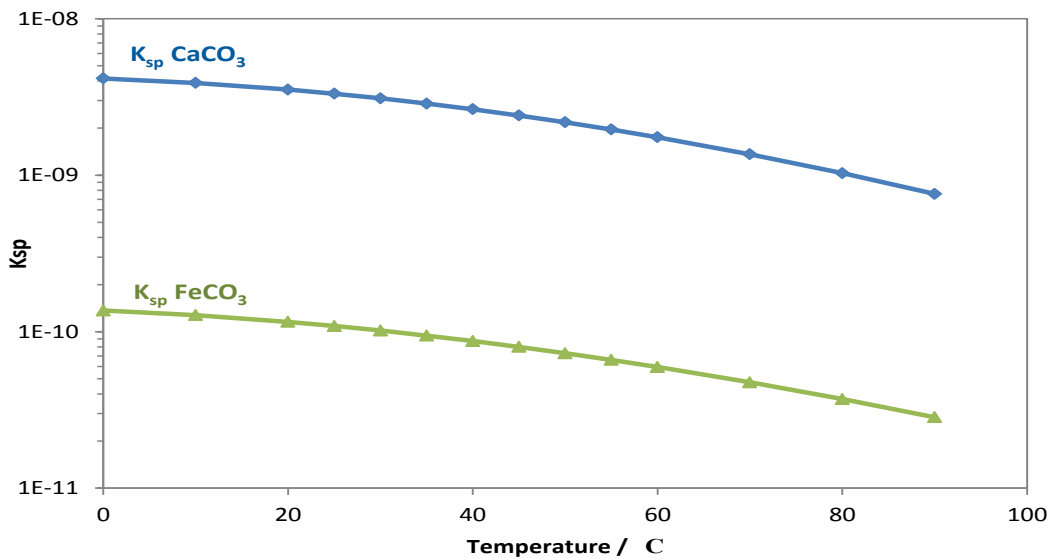


Figure 3. Solubility product of  $\text{CaCO}_3$  and  $\text{FeCO}_3$  at different temperatures.

### **Effect of Ca<sup>2+</sup> on corrosion**

Little has been reported on the effect of Ca<sup>2+</sup> on CO<sub>2</sub> corrosion in the literature, with findings often appearing contradictory as is discussed below.

Eriksrud and Sontvedt indicated that in the presence of Ca<sup>2+</sup> and HCO<sub>3</sub><sup>-</sup> ions at concentrations found in real produced water, the corrosion rate decreased due to the formation of protective FeCO<sub>3</sub> layers “enriched” with Ca<sup>2+</sup>. The tests were conducted in three different formation waters with concentrations of 538, 3960, and 54200 ppm of Ca<sup>2+</sup> at 20°C and 1 bar. The reported pH range was 5.80 to 7.39 [31].

Zhao, *et al.*, further claimed that the corrosion rate decreased in the “short term” in the presence of Ca<sup>2+</sup> and Mg<sup>2+</sup>, but that there was no special difference for “long term exposure”. They conducted experiments at 90°C and CO<sub>2</sub> partial pressure of 25 bars with 1000 ppm Mg<sup>2+</sup> and 6000 ppm Ca<sup>2+</sup>. In addition to corrosion behavior, the corrosion products’ morphology and composition had been changed by the presence of new cations (Ca<sup>2+</sup> and Mg<sup>2+</sup>) in the solution. They described the primary corrosion product as “Fe(Ca,Mg)(CO<sub>3</sub>)<sub>2</sub>” [32][33].

X. Jiang, *et al.*, reported an effect of Ca<sup>2+</sup> on pitting phenomena. They conducted three experiments with 3 wt.% NaCl, 3 wt.% NaCl + 1.5 wt.% CaCl<sub>2</sub> and 4.6 wt.% NaCl. The reported pitting initiation times were 70 hours for the experiment with 3 wt. % NaCl, 41 hours for the 3 wt.% NaCl + 1.5 wt.% CaCl<sub>2</sub> electrolyte, and 23 hours for 4.6% wt.% NaCl. They claimed that while Cl<sup>-</sup> caused pitting, the presence of Ca<sup>2+</sup> delayed the pitting initiation time [34].

Ding, *et al.*, conducted experiments at 75°C and a pressure of 10 bar CO<sub>2</sub> with 64, 128, 256, and 512 ppm of Ca<sup>2+</sup>; in common with other studies, pH was not reported. They claimed that the corrosion rate increased with an increase in the Ca<sup>2+</sup> concentration and that its presence changed the corrosion product layer's grain/crystal size; the addition of Ca<sup>2+</sup> made the corrosion product layer crystals "bigger" and "looser", so that they did not act as a sufficiently protective barrier and consequently allowed corrosive species to more readily diffuse to the metal surface. They also showed XRD data, with shifted peaks from the FeCO<sub>3</sub> peak position with increasing Ca<sup>2+</sup> concentration in the electrolyte, and hence the corrosion product layer. This shift is the result of the change in the unit cell of the corrosion products with the formation of Fe<sub>1-x</sub>Ca<sub>x</sub>CO<sub>3</sub> [35].

Ren, *et al.*, carried out experiments at 7 MPa and 80°C with three different electrolyte species; Na<sub>2</sub>SO<sub>4</sub>, NaHCO<sub>3</sub> and CaCl<sub>2</sub>. They reported a higher pitting corrosion rate for the experiments with CaCl<sub>2</sub>. As was claimed before by Jiang, *et al.*, [34] Ren, *et al.*, ascribed the pitting to the presence of Cl<sup>-</sup> in the solution. pH was also not reported in their studies [36].

Zhu, *et al.*, conducted a failure analysis on the samples taken from a Tarim oil field well. They reported the presence of CaCO<sub>3</sub> along with FeCO<sub>3</sub> on the surface as the scale and corrosion products, respectively. The observed pitting mostly referred to the presence of Cl<sup>-</sup> as was claimed by previous researchers [34], [36], [37]; it does not seem that Ca<sup>2+</sup> had been taken into consideration as a potential contributory factor relating to pitting [38].

Gao, *et al.*, carried out corrosion experiments with a simulated water stream from the east of China. The experiment conditions were different for flow (0, 0.5 and 1 m/s) and pressure of CO<sub>2</sub> (0.1, 0.3 and 1 MPa). The temperature was set to 65°C, with 64 ppm CaCl<sub>2</sub>, and 78 ppm MgCl<sub>2</sub>. The corrosion product was reported as being comprised mostly of FeCO<sub>3</sub> at lower pCO<sub>2</sub> (0.1 MPa), while at a higher CO<sub>2</sub> partial pressure, due to the higher CO<sub>3</sub><sup>2-</sup> concentration, a solid solution was formed. They claimed the formation of “(Fe,Ca,Mg)CO<sub>3</sub>” at 0.3 MPa, and “(Fe,Ca)CO<sub>3</sub>” at 1MPa. According to their report, at higher CO<sub>2</sub> partial pressure both general and localized corrosion was higher. Although the pH plays a very important role in the corrosion study, it was not reported by the authors [39].

This study has been motivated by the incomplete understanding and lack of consistency in the reported information in the literature on the effect of Ca<sup>2+</sup> in the CO<sub>2</sub> environments.

## CHAPTER 3: RESEARCH OBJECTIVES AND TEST MATRICES

### **Project objectives and hypotheses**

The objective of the current study is to observe the effect of calcium carbonate precipitation/formation on mechanisms related to CO<sub>2</sub> corrosion, with particular emphasis on environments related to carbon sequestration in saline aquifers as well as production/injection wells and pipeline transmission systems in the oil and gas industry.

The central hypothesis of this study is that heterogeneity of the corrosion product layer changes the mode of attack from general to localized corrosion.

### **Experimental setup and test matrixes**

Experiments were carried out with the experimental set up as is shown in Figure 4. AISI 1018 mild steel specimens with a chemical composition according to Table 2. were used for electrochemical measurements and analysis specimen were wet-polished with grit silicon carbide (SiC) paper down to 600 grade, and rinsed with isopropyl alcohol in an ultrasonic bath and cool air dried, before immersion.

Table 2. Chemical composition carbon steel CS1018 (%), balance Fe).

<b><i>Al</i></b>	<b><i>As</i></b>	<b><i>C</i></b>	<b><i>Co</i></b>	<b><i>Cr</i></b>	<b><i>Cu</i></b>	<b><i>Mn</i></b>	<b><i>Mo</i></b>	<b><i>Nb</i></b>	<b><i>Ni</i></b>	<b><i>P</i></b>
0.008	0.006	0.18	0.003	0.12	0.18	0.75	0.02	0.002	0.065	0.011
<b><i>S</i></b>	<b><i>Sb</i></b>	<b><i>Si</i></b>	<b><i>Sn</i></b>	<b><i>Ta</i></b>	<b><i>Ti</i></b>	<b><i>V</i></b>	<b><i>W</i></b>	<b><i>Zn</i></b>	<b><i>Zi</i></b>	
0.021	0.009	0.16	0.009	0.028	0.002	0.003	0.014	0.004	0.003	

\*Data as given by the manufacturer

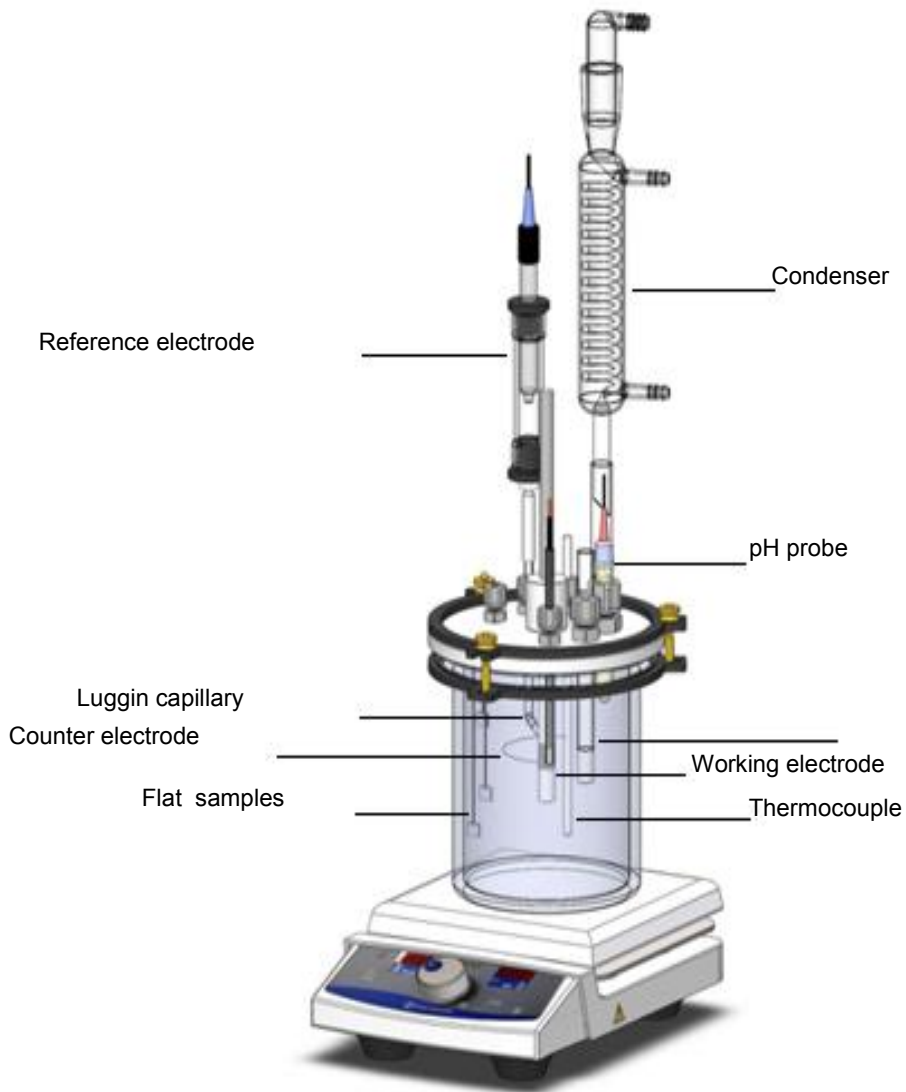


Figure 4. Experimental setup<sup>3</sup>.

Experiments were conducted in a 2 liter glass cell using a three electrode setup.

- Cylindrical mild steel sample as a working electrode (WE).
- Concentric platinum ring counter electrode (CE).
- Saturated silver/silver chloride (Ag/AgCl) reference electrode (RE).

<sup>3</sup> Drawing courtesy of Cody Shafer.

A potentiostat was connected to a personal computer that was used for electrochemical measurements, which were conducted under stagnant conditions. The pH and temperature were continuously monitored. However, the monitored pH was the bulk pH due to the difficulties associated with surface pH measurement.

The electrochemical measurements were conducted using a Gamry potentiostat with accompanying software. According to the details presented in Table 3, the measured solution resistance by EIS was used to correct the polarization resistance.

Table 3. Experimental parameters for electrochemical measurements.

Technique	Parameters
LPR	Scan Rate: 0.125 mV / s. Polarization range: $\pm 5$ mV (vs. EOC). B value: 26 mV
EIS	Frequency range: 10000 Hz ~ 0.001 Hz. Amplitude: 10 mV. DC Potential : 0 Vs. OCP

At adjusted conditions (pH to 6.6 at 80°C) in a 1 wt.% NaCl electrolyte saturated with CO<sub>2</sub> gas, FeCO<sub>3</sub> or CaCO<sub>3</sub> will be expected to precipitate once supersaturation conditions are achieved [6]. Therefore, any changes or unexpected behavior in FeCO<sub>3</sub> precipitation can be related to Ca<sup>2+</sup> effects. In the first series of experiments with favorable conditions for the formation of FeCO<sub>3</sub>, a test solution with 10 ppm Fe<sup>2+</sup> was chosen as the baseline experiment. It was decided to initially add 10 ppm Fe<sup>2+</sup>, as ferrous chloride, to accelerate the formation of FeCO<sub>3</sub>. The saturation degree of FeCO<sub>3</sub> is a very useful tool which can be manipulated to achieve the desired formation of a FeCO<sub>3</sub> layer. As reported by Nesic [6], to have the FeCO<sub>3</sub> layer form on the steel surface the saturation

degree should be significantly larger than unity. This value is calculated from the two measured values of  $\text{Fe}^{2+}$  and  $\text{CO}_3^{2-}$  concentration (via pH) [18].

Table 4 shows the four different series of experiments designed for this study:

1<sup>st</sup>: Effect of  $\text{Ca}^{2+}$  concentration on corrosion behavior.

2<sup>nd</sup>: Effect of pH fluctuation on the corrosion behavior of the system with low concentration of  $\text{Ca}^{2+}$ .

3<sup>rd</sup>: Evaluation of the effect of high concentration of  $\text{Cl}^-$  on corrosion behavior.

4<sup>th</sup>: Effect of initial pH and saturation degree of  $\text{CaCO}_3$  at high  $\text{Ca}^{2+}$  concentration on corrosion behavior.

Table 4. Test conditions.

	<b>Test</b>	<b>Initial concentrations of <math>\text{Fe}^{2+}</math> and <math>\text{Ca}^{2+}</math></b>
1 <sup>st</sup> series	1	1wt % NaCl + 10 ppm $\text{Fe}^{2+}$
	2	1wt % NaCl + 10 ppm $\text{Fe}^{2+}$ + 10 ppm $\text{Ca}^{2+}$
	3	1wt % NaCl + 10 ppm $\text{Fe}^{2+}$ + 100 ppm $\text{Ca}^{2+}$
	4	1wt % NaCl + 10 ppm $\text{Fe}^{2+}$ + 1,000 ppm $\text{Ca}^{2+}$
	5	1wt % NaCl + 10 ppm $\text{Fe}^{2+}$ + 10,000 ppm $\text{Ca}^{2+}$
2 <sup>nd</sup> series	1	1wt % NaCl + 10 ppm $\text{Fe}^{2+}$
	2	1wt % NaCl + 10 ppm $\text{Fe}^{2+}$ + 10 ppm $\text{Ca}^{2+}$
	3	1wt % NaCl + 10 ppm $\text{Fe}^{2+}$ + 100 ppm $\text{Ca}^{2+}$
3 <sup>rd</sup> series	1	1wt % NaCl + 10 ppm $\text{Fe}^{2+}$ + 10,000 ppm $\text{Cl}^-$
	2	1wt % NaCl + 3 wt % NaCl
4 <sup>th</sup> series	1	1wt % NaCl + 10,000 ppm $\text{Ca}^{2+}$ initial pH 6.6
	2	1wt % NaCl + 10,000 ppm $\text{Ca}^{2+}$ initial pH 5.3

Table 5 shows the test matrix for the first two experimental series. The test matrix for the experimental series designed to study the effect of chloride on the corrosion behavior is summarized in Table 6. A 3 wt.% NaCl solution has the equivalent Cl<sup>-</sup> concentration to 54.7 g CaCl<sub>2</sub> (17,800 ppm) for 2 litres of electrolyte; 54.7 gr of CaCl<sub>2</sub> corresponds to 2.7 wt.%. The initial pH for the experiments with 4 wt.% NaCl solution was set to pH 5.5, because as soon as 54.7 g CaCl<sub>2</sub> was added to the glass cell for the experiments with 10,000 ppm Ca<sup>2+</sup>, the pH immediately dropped to pH 5.5 due to the fast precipitation of CaCO<sub>3</sub> and its imposed effect on the equilibria and the electroneutrality equation as noted earlier.

Table 5. Test matrix for low to high Ca<sup>2+</sup> concentrations.

Parameters	Conditions
Total Pressure	1 bar
Temperature	80°C
Solution	1 wt.% NaCl
pH	6.6
Condition	Stagnant
Material	CS1018
Methods	OCP, LPR-EIS

Table 6. Test matrix for the effect of  $\text{Cl}^-$ .

Parameters	Conditions
Total Pressure	1 bar
Temperature	80°C
$\text{CO}_2$ Partial Pressure	0.5 bar
Solution	1 wt.% NaCl + 2.7 wt.% $\text{CaCl}_2$ and 1 wt.% NaCl + 3 wt.% NaCl
Condition	Stagnant
Material	AISI 1018
Methods	OCP, LPR, EIS

The  $\text{CaCO}_3$  saturation degree of a  $\text{CO}_2$  saturated solution with 10,000 ppm  $\text{Ca}^{2+}$  at 80°C, with a pH of 6.6 is around  $S=10,000$ . Thus, this solution is highly supersaturated with respect to  $\text{CaCO}_3$ . A second experiment was carried out with the pH set such that the saturation degree of  $\text{CaCO}_3$  is about  $S=10$ , *i.e.*, a considerably lower degree of supersaturation. No  $\text{Fe}^{2+}$  was added into the cell. Table 7 shows the experiments matrix for these experiments conditions.

Table 7. Test matrix for the effect of initial pH.

Parameters	Conditions
Total Pressure	1 bar
Temperature	80°C
CO <sub>2</sub> Partial Pressure	0.5 bar
Solution	10 ppm Fe <sup>2+</sup> + 10,000 ppm Ca <sup>2+</sup> <b><u>Initial pH 6.6</u></b> 0 ppm Fe <sup>2+</sup> + 10,000 ppm Ca <sup>2+</sup> <b><u>Initial pH 5.3</u></b>
Condition	Stagnant
Material	AISI 1018
Methods	OCP, LPR, EIS

The Fe<sup>2+</sup> concentration was measured by a spectrophotometer. Water samples were collected once or twice a day, and the CO<sub>3</sub><sup>2-</sup> concentration was calculated from the monitored pH. Thus, the FeCO<sub>3</sub> saturation degree was calculated using the measured Fe<sup>2+</sup> and CO<sub>3</sub><sup>2-</sup> concentrations according to Equation (15).

The cell was filled with 2 liters of 1 wt.% NaCl, prepared from deionized water. The solution was agitated with a magnetic stirrer and the temperature set to 80°C. To keep a positive pressure, CO<sub>2</sub> gas was continuously purged into the solution. The solution pH was adjusted to the desired value by the addition of a deoxygenated sodium bicarbonate solution. After the pH stabilized, the desired Fe<sup>2+</sup> and Ca<sup>2+</sup> concentrations were added by addition of FeCl<sub>2</sub> and CaCl<sub>2</sub>, respectively, into the electrolyte. One

cylindrical (for electrochemical measurements) and three flat square specimens (for surface analysis) of C1018 steel were inserted into the glass cell. No stirring was applied during the experiments, so that the solution was practically stagnant.

The corrosion behavior was monitored by electrochemical methods: open circuit potential (OCP), linear polarization resistance (LPR), and electrochemical impedance spectroscopy (EIS) measurements. All experiments were followed by surface analysis using X-ray diffraction (XRD), scanning electron microscopy (SEM), energy dispersive X-ray spectroscopy (EDS), and infinite focus microscopy (IFM) to investigate the effect of  $\text{Ca}^{2+}$  on the morphology of  $\text{FeCO}_3$ .

Using LPR data and Equation (24) [40], corrosion rate in (mm/yr) was calculated based on the corrosion current density  $i_{Cor}$  ( $\text{A}/\text{m}^2$ ) as follow:

$$B = \frac{b_a b_c}{2.303(b_a + b_c)} \quad (22)$$

$$i_{Cor} = \frac{B}{R_p * A} \quad (23)$$

$$CR = 1.16 * i_{Cor} \quad (24)$$

Where B is known as B value;  $b_a$  and  $b_c$  are respectively anodic and cathodic Tafel slopes.  $R_p$  is the corrosion resistance and A is the surface area in  $\text{cm}^2$ .

Prior to surface analysis, samples were washed with deoxygenated deionized water and rinsed with isopropyl alcohol then dried. Surface of the samples were cleaned with Clarke solution (1000 mL. HCl, 20 gr.  $\text{Sb}_2\text{O}_3$  plus 50 gr  $\text{SnCl}_2$ ) according to ASTM G1 [41] procedure prior to the weight loss measurements and subsequent surface analysis by SEM and IFM. Samples were weighed and then kept in the Clarke solution for 1

minute, rinsed with deionized water and isopropyl alcohol, respectively, dried and reweighed. The process was repeated until the weight was constant.

### **Weight loss measurement procedure**

A flat sample with a surface area of 3.4 cm<sup>2</sup> which was weighed prior to insertion into the glass cell to be used for weight loss measurements. At the end of the experiment, the sample was treated with Clarke solution [41] according to the previously explained procedure. Thereafter, the weight loss corrosion rate in (mm/yr) was calculated using Equation (25):

$$CR_{wl} = \frac{\Delta m(gr) * 24(hr) * 365(day)}{A(cm^2) * t(hr) * \rho(grcm^{-3}) * 1(day) * 1(1yr)} \quad (12)$$

### **Pitting corrosion rate measurement procedure**

SEM analysis was performed on the flat samples - the same ones which the weight loss measurement was performed with. In the case of a non-uniform corroded surface, IFM analysis was performed on the sample to measure the depth of the non-uniformed corroded area. Finally, the pitting corrosion rate in (mm/yr) was calculated using the deepest depth of pits measured by IFM, according to Equation (26):

$$CR_{pit} = \frac{pitdept(\mu m) * 0.001(mm\mu m^{-1}) * 365(days)}{t(days) * 1(1yr)} \quad (26)$$

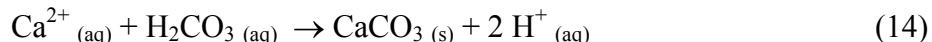
To identify the nature of corrosion, the pitting ratio was calculated using Equation (27) [42].

$$PittingRatio = \frac{CR_{pit}}{CR_{wl}} \quad (13)$$

## CHAPTER 4: RESULTS AND DISCUSSION

### **Effect of calcium concentrations on corrosion**

Figure 5 and Figure 6 show the variations of corrosion rate and OCP with time for each tested condition. The corrosion rates decreased with time in solutions with low concentrations of  $\text{Ca}^{2+}$  tested: no  $\text{Ca}^{2+}$ , 10 ppm  $\text{Ca}^{2+}$  and 100 ppm  $\text{Ca}^{2+}$  conditions. This indicates that a protective  $\text{FeCO}_3$  layer was formed on the steel surface at these conditions, hence corrosion rates decreased due to the blockage effect of the  $\text{FeCO}_3$  layer on the steel surface[6], [16]. However, the corrosion behavior of the experiments with higher  $\text{Ca}^{2+}$  concentrations (1,000 ppm  $\text{Ca}^{2+}$  and 10,000 ppm  $\text{Ca}^{2+}$ ) was completely different. The corrosion rate did not decrease with time, which may be due to the lack of formation of a protective layer on the steel surface as well as the lower pH, according to Figure 7. Note that bulk precipitation of  $\text{CaCO}_3$  as well as  $\text{FeCO}_3$  in aqueous  $\text{CO}_2$ , from formed  $\text{H}_2\text{CO}_3$ , will lead to generation of acidity. However, due to the higher available concentrations of  $\text{Ca}^{2+}$  in the bulk which leads to the higher saturation degree with respect to  $\text{CaCO}_3$ , a  $\text{CaCO}_3$  precipitation effect on the pH in the solution is more rapid according to Reaction (28). This reaction is a combination of Reactions (1) to (6) and Reaction (17) which explicitly shows the acidification process due to the formation of  $\text{CaCO}_3$ .



According to Figure 6, there was no noticeable difference in the corrosion potential behavior with time. It seemed that in the presence of 10,000ppm  $\text{Ca}^{2+}$  the cathodic reaction is more affected than the other conditions. The observed slight increase

in potential can be due to acceleration of the cathodic reaction. As is shown in Figure 2 the corrosion rate is high for this condition. The accelerated cathodic reaction is because of the lower pH, as reported in Figure 6 as well as formation of iron carbide which is a preferred site of the cathodic reaction. The greater availability of  $H^+$  provides the steel surface with more species available for cathodic reaction [6].

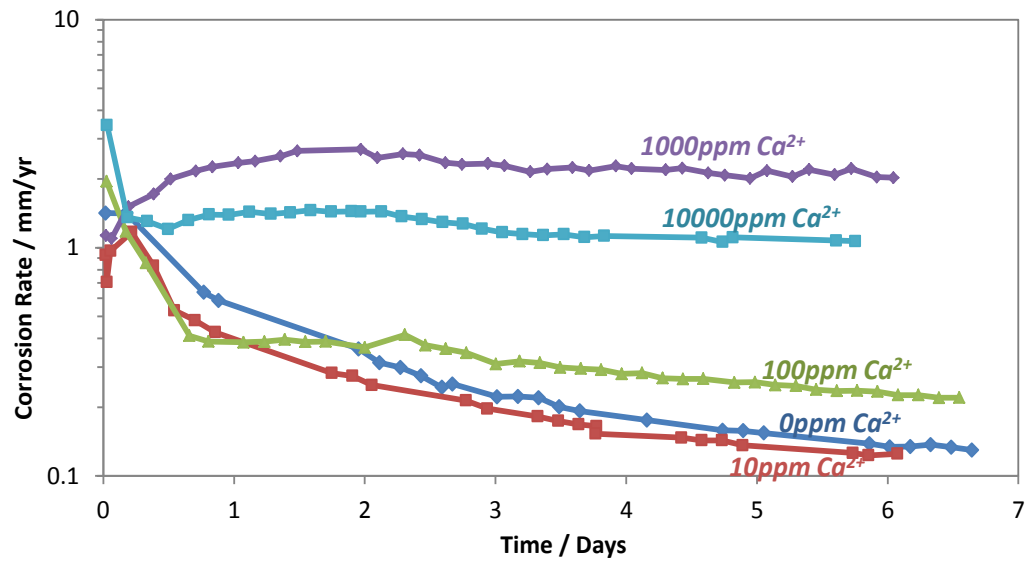


Figure 5. Variations of corrosion rate of CS1018 versus time for 5 experiments with different initial conditions of 0, 10, 100, 1000, 10000 ppm  $Ca^{2+}$ .

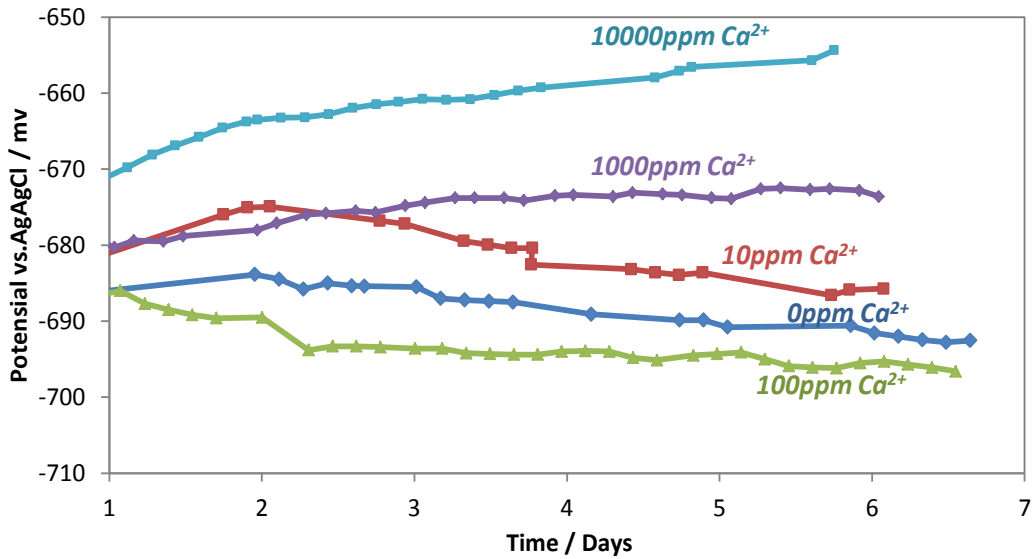


Figure 6. Variations of open circuit potential of CS1018 versus time for 5 experiments with different initial conditions of 0, 10, 100, 1000, 10000 ppm  $\text{Ca}^{2+}$ .

Figure 7 represents the variations of pH over time. With low  $\text{Ca}^{2+}$  concentrations (0, 10 and 100 ppm), the pH remained almost constant, close to the initially set value of pH 6.6, whereas it dropped to around pH 6.0 for the condition with 1,000 ppm  $\text{Ca}^{2+}$  and to around pH 5.4 for the condition with 10,000 ppm  $\text{Ca}^{2+}$ , this represents an order of magnitude increase in hydrogen ion concentration. This decrease in pH is due to the liberation of hydrogen ion upon the bulk precipitation of calcium carbonate according to Reaction (28).

The supersaturated solution, with respect to  $\text{CaCO}_3$ , leads to precipitation of  $\text{CaCO}_3$ . The pH drops as  $\text{Ca}^{2+}$  is consumed and affects speciation of carbonic species ( $\text{CO}_3^{2-}$  is consumed as well), shifting the equilibria and consequently changing all the concentrations in the solution as shown in Figure 1.

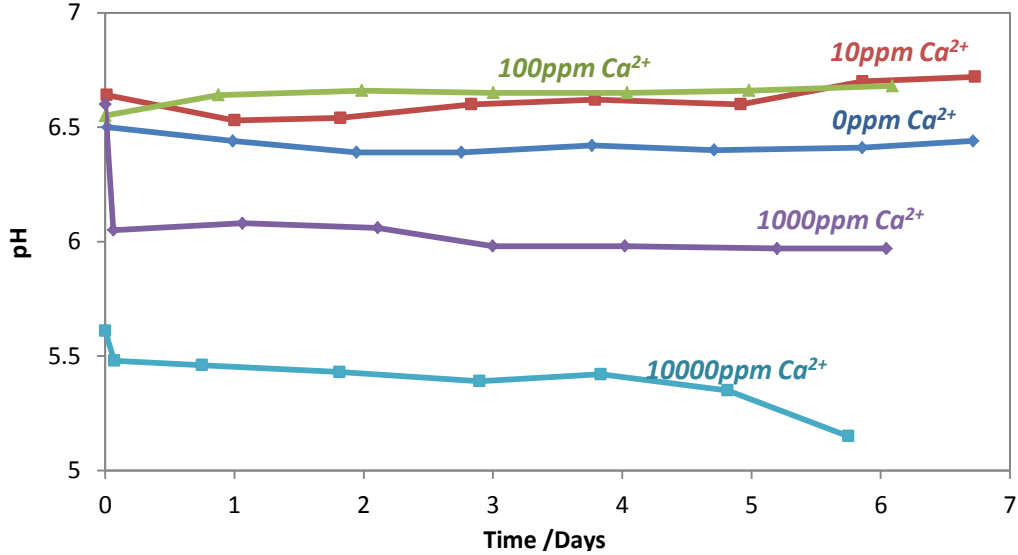


Figure 7. Variations of the bulk pH versus time for 5 experiments with different initial conditions of 0, 10, 100, 1000, 10000 ppm Ca<sup>2+</sup>.

Figure 8 shows the variation of Fe<sup>2+</sup> concentrations. The Fe<sup>2+</sup> concentrations decreased over time at low Ca<sup>2+</sup> concentrations, probably due to rapid precipitation of FeCO<sub>3</sub>. At 1,000 and 10,000 ppm Ca<sup>2+</sup>, the opposite happened, i.e. the Fe<sup>2+</sup> concentration increased with time. This is supported by the trends observed with the corrosion behavior in Figure 5. As time passed the corrosion rate stayed high in the elevated Ca<sup>2+</sup> concentration experiments (1,000 and 10,000 ppm) and it is likely that precipitation of FeCO<sub>3</sub> was slow, resulting in a net increase of Fe<sup>2+</sup> ions in solution.

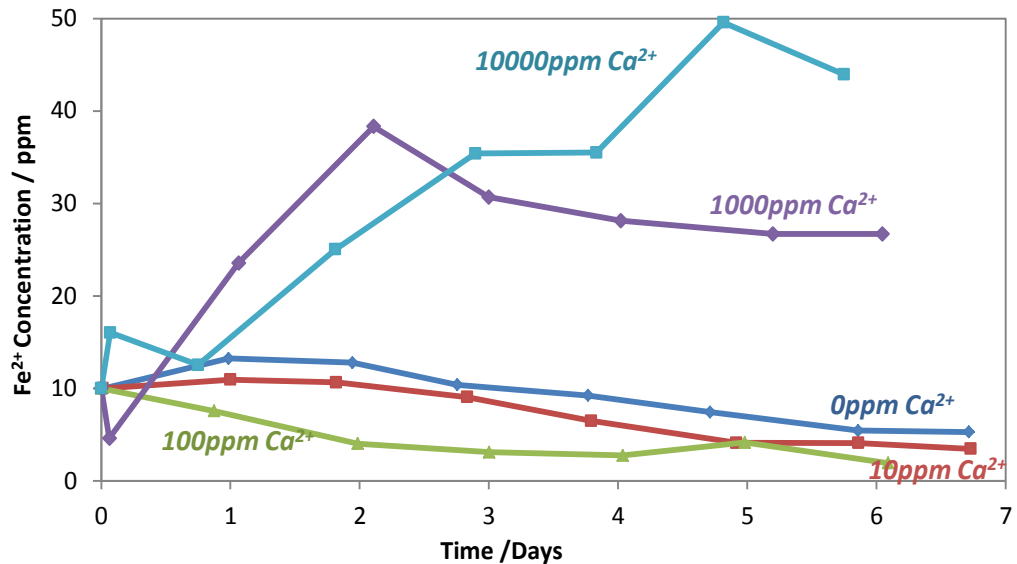


Figure 8. Variations of the bulk  $\text{Fe}^{2+}$  concentration versus time for 5 experiments with different initial conditions of 0, 10, 100, 1000, 10000 ppm  $\text{Ca}^{2+}$ .

Figure 9 shows the variation of  $\text{Fe}^{2+}$  and  $\text{Ca}^{2+}$  for the experiment with 1,000 ppm  $\text{Ca}^{2+}$ . The concentration of  $\text{Ca}^{2+}$  decreased rapidly in the first couple of hours, from the initial 1,000 ppm. This is because the solution supersaturated with respect to  $\text{CaCO}_3$  led to rapid precipitation of  $\text{CaCO}_3$  and a drop in  $\text{Ca}^{2+}$  concentration.

Figure 10 shows the saturation degree for  $\text{CaCO}_3$  and  $\text{FeCO}_3$ . The concentration of  $\text{Ca}^{2+}$  stabilized when the saturation degree of  $\text{CaCO}_3$  reached around 10 and the precipitation slowed down. The  $\text{Fe}^{2+}$  concentration dropped in the first two hours probably due to some precipitation of  $\text{FeCO}_3$ , but also due to a drop in pH caused by more rapid precipitation of  $\text{CaCO}_3$ . Subsequently the  $\text{Fe}^{2+}$  concentration increased and reached a plateau in step with the general corrosion rate trend. The solution was super saturated with respect to both  $\text{CaCO}_3$  and  $\text{FeCO}_3$  throughout the experiment.

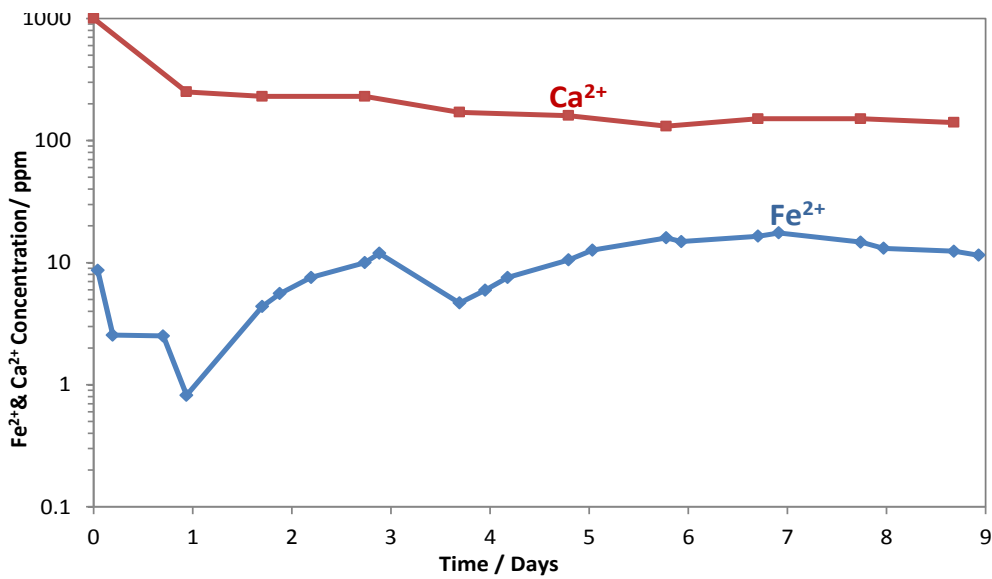


Figure 9. Variations of the bulk  $\text{Fe}^{2+}$  and  $\text{Ca}^{2+}$  concentrations versus time for the experiment with the initial 1000 ppm  $\text{Ca}^{2+}$ .

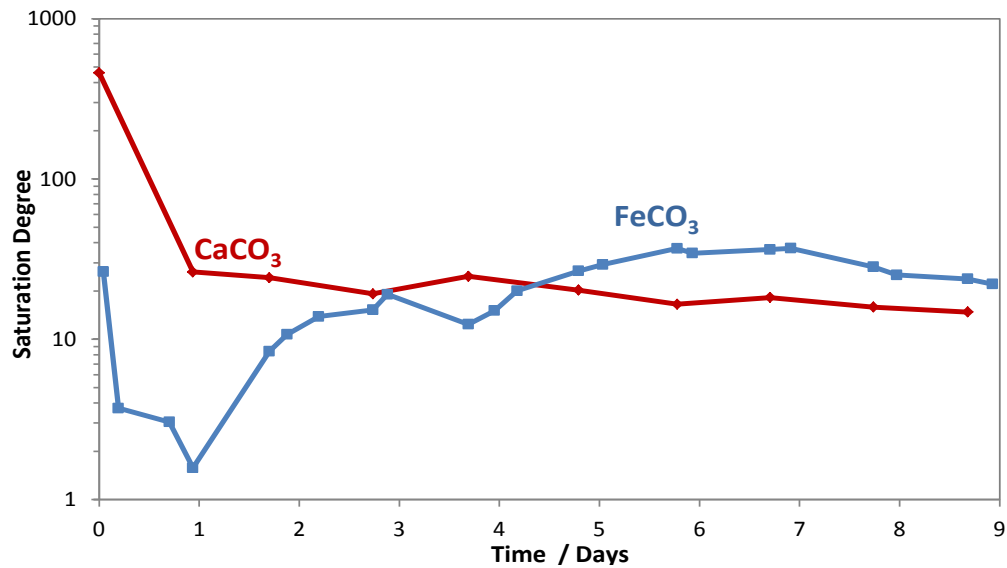


Figure 10. Variations of the  $\text{FeCO}_3$  and  $\text{CaCO}_3$  saturation degree versus time for the experiment with the initial 1000 ppm  $\text{Ca}^{2+}$ .

Figure 11 shows the experiments with no  $\text{Ca}^{2+}$ , 10 ppm  $\text{Ca}^{2+}$  and 100 ppm  $\text{Ca}^{2+}$ , the degree of  $\text{FeCO}_3$  saturation was higher than in the experiments with 1,000 ppm  $\text{Ca}^{2+}$  and 10,000 ppm  $\text{Ca}^{2+}$  due to a higher bulk pH.

According to Figure 5, the corrosion rate did not decrease significantly for the higher  $\text{Ca}^{2+}$  concentration experiments (1,000 ppm  $\text{Ca}^{2+}$  and 10,000 ppm  $\text{Ca}^{2+}$ ). This phenomenon is explained by the fact that the high concentration of  $\text{Ca}^{2+}$  changed the environment for  $\text{FeCO}_3$  formation and deposition. Given the fact that  $\text{CaCO}_3$  and  $\text{FeCO}_3$  are isostructural [2], it is expected that  $\text{Ca}^{2+}$  was incorporated into the  $\text{FeCO}_3$  lattice and may have changed its ability to retard corrosion.

Thus the expected carbonates are, as mentioned earlier,  $\text{FeCO}_3$  as shown in Reaction (6),  $\text{CaCO}_3$  as in Reaction (17) and  $\text{Fe}_x\text{Ca}_y\text{CO}_3$  ( $x+y=1$ ) as in (18).

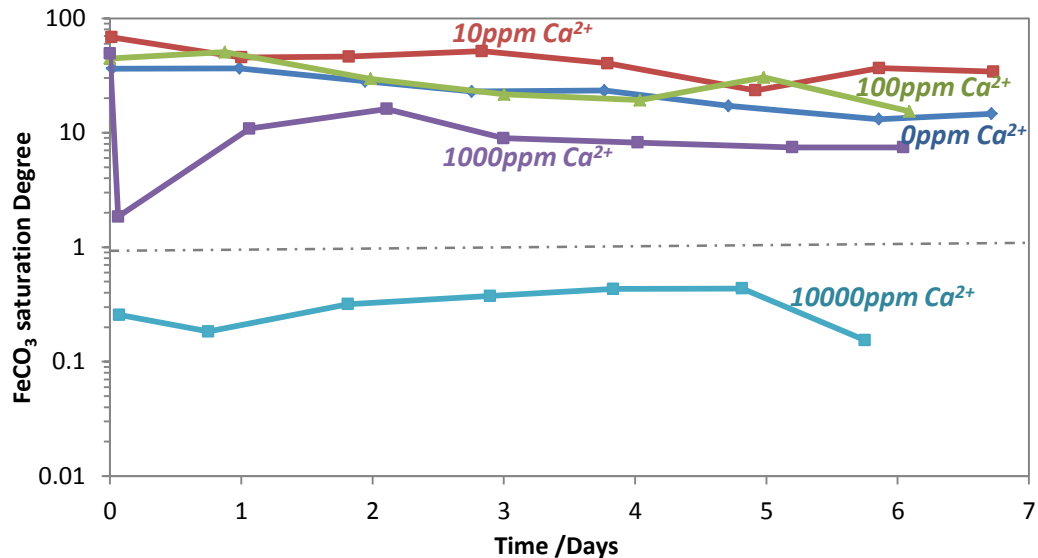


Figure 11. Variations of the bulk  $\text{FeCO}_3$  saturation degree versus time for 5 experiments with different initial conditions of 0, 10, 100, 1000, 10000 ppm  $\text{Ca}^{2+}$ .

Figure 12 shows the SEM images of the recovered samples from the bulk solution with different concentrations of  $\text{Ca}^{2+}$ . The morphology of  $\text{FeCO}_3$  at lower  $\text{C}(\text{Ca}^{2+})$  did not change while at higher  $\text{C}(\text{Ca}^{2+})$  it had changed dramatically. Figure 12 (a) is the image for no  $\text{Ca}^{2+}$  which gives a good baseline comparison. Figure 12 (b) and (c) are the images for 10ppm and 100ppm  $\text{Ca}^{2+}$ , respectively. A comparison of these images with Figure 12 (a) shows there was not a significant change in the morphology of formed layers on the surface of the tested samples. According to the corrosion rate plot in Figure 5, due to the similar corrosion behavior for solutions with 0 to 100 ppm  $\text{Ca}^{2+}$ , it was expected to see a relatively similar morphology of the surface layer. The solutions with 1,000 and 10,000 ppm  $\text{Ca}^{2+}$  had significantly different corrosion behavior. It was therefore anticipated to see a significantly different morphology at the surface for the 1,000 and 10,000 ppm  $\text{Ca}^{2+}$  experiments. This morphology was not only different to what can be observed for the lower  $\text{Ca}^{2+}$  concentrations, but it also varied from one to the other.

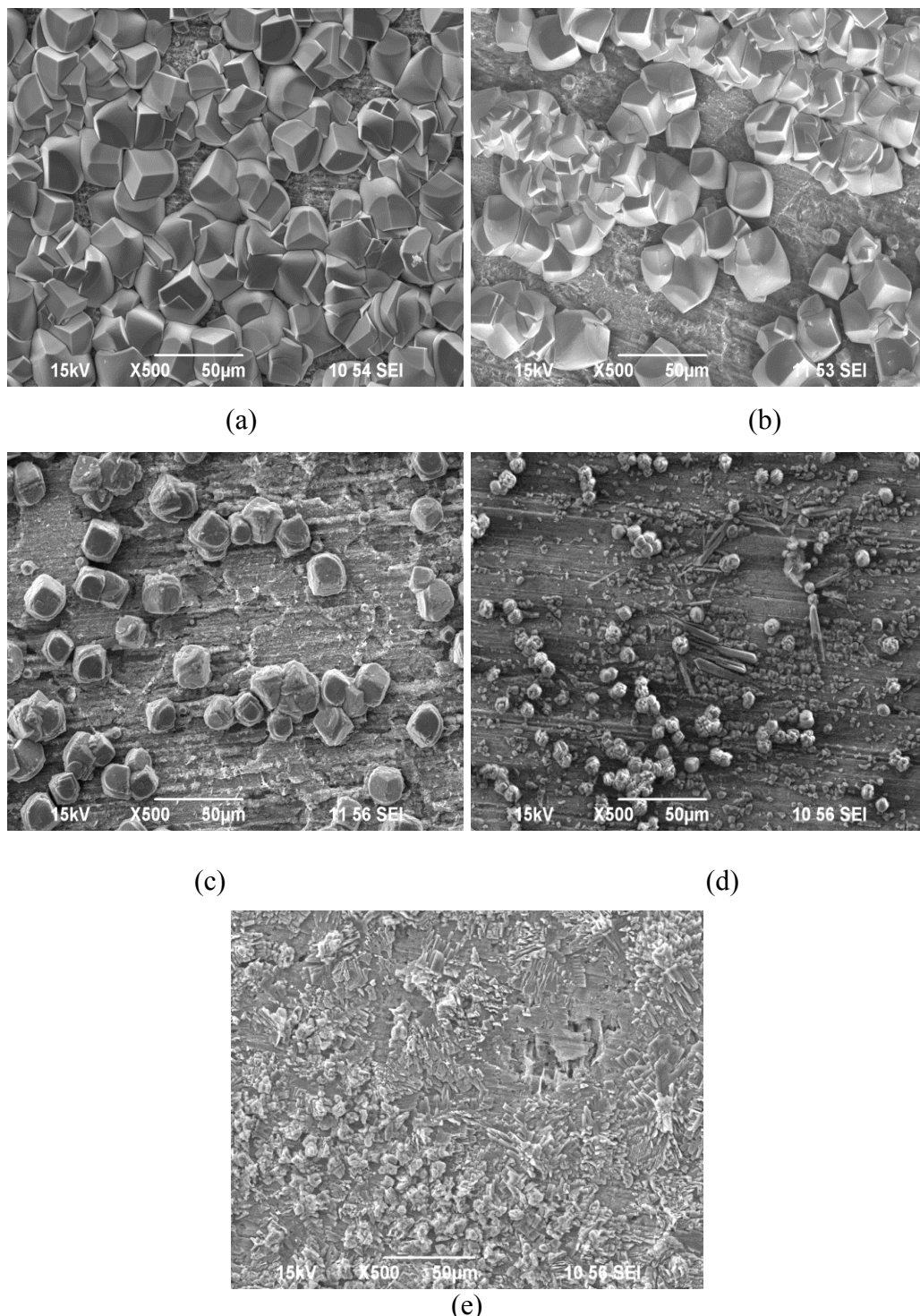
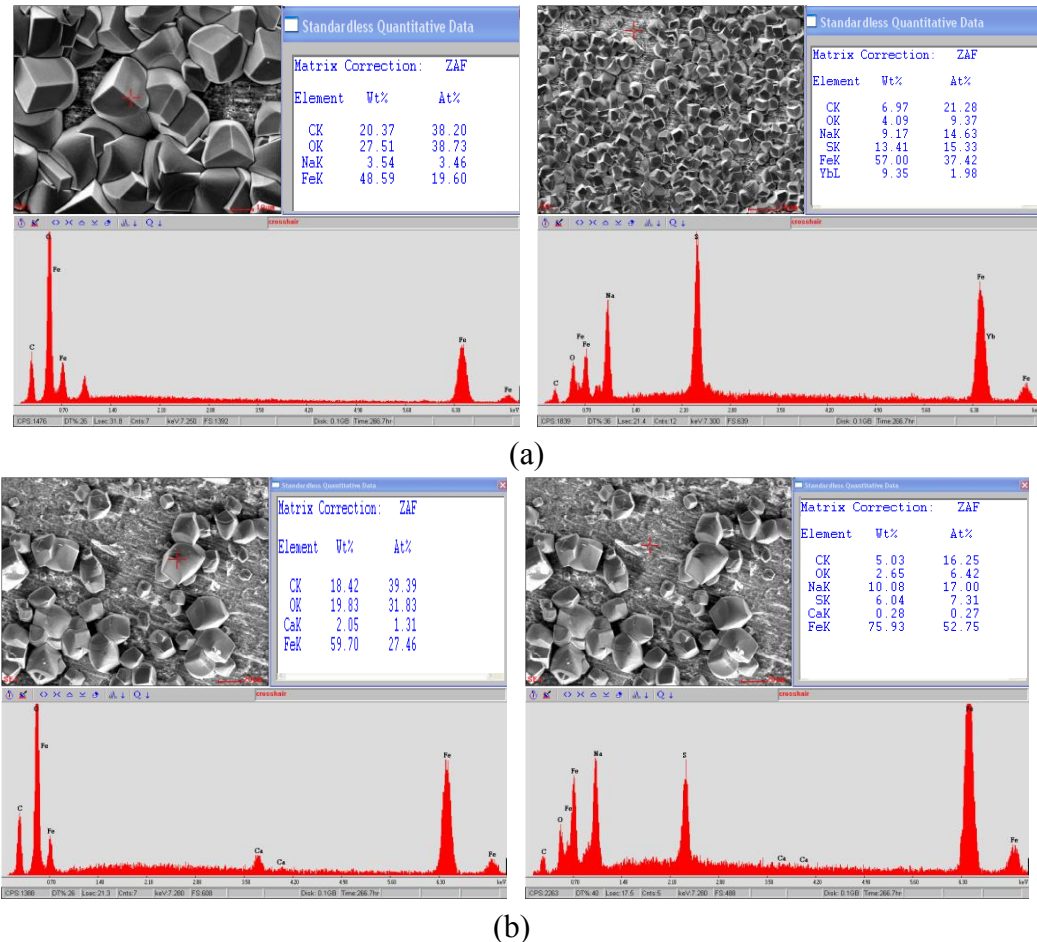


Figure 12. SEM images taken on carbon steel specimen (CS1018) surface of the bulk solution with 10 ppm  $\text{Fe}^{2+}$  (a) no  $\text{Ca}^{2+}$  (b) 10 ppm  $\text{Ca}^{2+}$  (c) 100 ppm  $\text{Ca}^{2+}$  (d) 1,000 ppm  $\text{Ca}^{2+}$  (e) 10,000 ppm  $\text{Ca}^{2+}$  at 80 °C and  $\text{pCO}_2$  0.5 bar after 7 days.

Figure 13 shows the EDS spectra of specimens from the solutions with no  $\text{Ca}^{2+}$ , 10ppm  $\text{Ca}^{2+}$ , 100ppm  $\text{Ca}^{2+}$ , 1,000ppm  $\text{Ca}^{2+}$  and 10,000ppm  $\text{Ca}^{2+}$ . A trace of  $\text{Ca}^{2+}$  could be detected by EDS even at very low concentration of 10ppm  $\text{Ca}^{2+}$ . The amount of substituted  $\text{Ca}^{2+}$  in the  $\text{FeCO}_3$  structure increased as the  $\text{Ca}^{2+}$  concentration increased in the experimented environments. At the higher  $\text{Ca}^{2+}$  concentration of 10,000ppm,  $\text{CaCO}_3$  formed on the surface along with  $\text{Fe}_x\text{Ca}_y\text{CO}_3$  ( $x+y=1$ ).



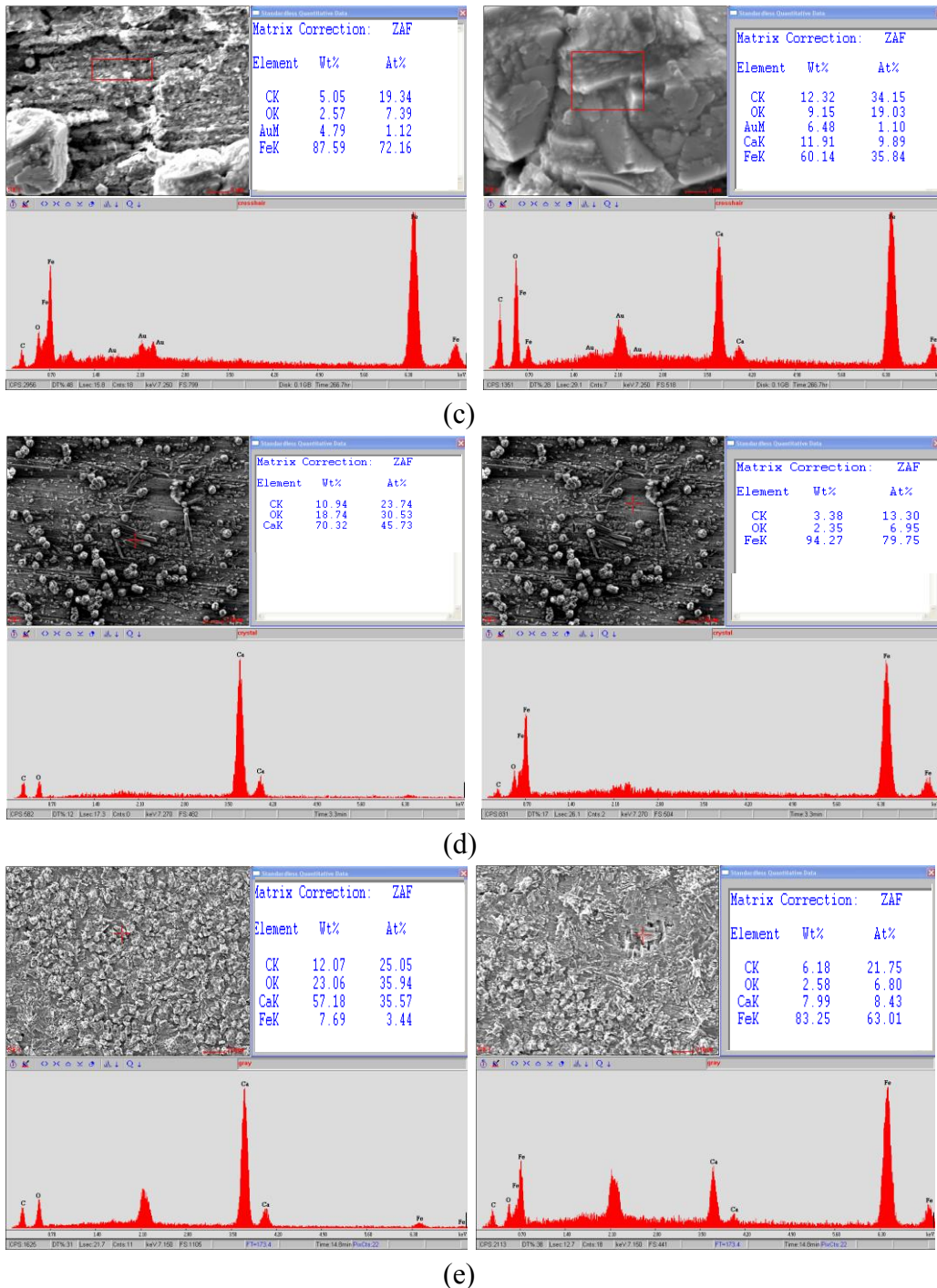


Figure 13. EDS spectra taken on carbon steel specimen (CS1018) surface of the bulk solution with 10 ppm  $\text{Fe}^{2+}$  (a) no  $\text{Ca}^{2+}$  (b) 10 ppm  $\text{Ca}^{2+}$  (c) 100 ppm  $\text{Ca}^{2+}$  (d) 1,000 ppm  $\text{Ca}^{2+}$  (e) 10,000 ppm  $\text{Ca}^{2+}$  at 80 °C and  $\text{pCO}_2$  0.5 bar after 7 days.

Figure 14 through Figure 18 represent the XRD patterns of the sample surface with different concentrations of  $\text{Ca}^{2+}$ . Due to the isostructural nature of  $\text{FeCO}_3$  and  $\text{CaCO}_3$  [2] and the potential for substitutional solid solutions ( $\text{Fe}_x\text{Ca}_y\text{CO}_3$  ( $x+y = 1$ )), a shift in the  $\text{FeCO}_3$  and  $\text{CaCO}_3$  peak positions in the XRD patterns was observed. Figure 15 and Figure 16 show a shift and broadening of the  $\text{FeCO}_3$  peaks toward the reference lines for  $\text{CaCO}_3$  for each of the recovered samples. The presented corrosion behavior plot in Figure 5 and the SEM images in Figure 12 (b) and (c) are a confirmation of the slight change observed in XRD data for these experiments. This is also the case for the very different corrosion behavior and surface morphology for the experiments conducted with 1,000 and 10,000 ppm  $\text{Ca}^{2+}$  in Figure 12 (d) and (e), which show significantly different XRD data shifted dramatically toward the reference lines for  $\text{CaCO}_3$  in Figure 17 and Figure 18 . According to the XRD data shown in Figure 17, a physical mixture of the  $\text{CaCO}_3$  and a solid solution of  $\text{Ca}_x\text{Fe}_y\text{CO}_3$  ( $x+y=1$ ) are presented on the surface Figure 18, which represents data for 10,000ppm  $\text{Ca}^{2+}$ , shows only one main peak of  $\text{CaCO}_3$  that is shifted and broadened toward the most intense reference line for  $\text{FeCO}_3$ . The high corrosion rate in this experiments (Figure 5) could be the result of the formation of a  $\text{Ca}_x\text{Fe}_y\text{CO}_3$  solid solution, with  $\text{Ca}^{2+}$  being dominant ( $x > y$ ), rather than  $\text{FeCO}_3$  on the surface. Ding *et al.* reported the shifted and broaden peaks for the XRD diffraction in their study[35]. They reported the formation of  $\text{Fe}_{1-x}\text{Ca}_x\text{CO}_3$  in the corrosion product. The maximum concentration of experimented condition was 512 ppm. They reported only a single layer on the surface with a shifted peak of  $\text{FeCO}_3$  toward the  $\text{CaCO}_3$  peak.

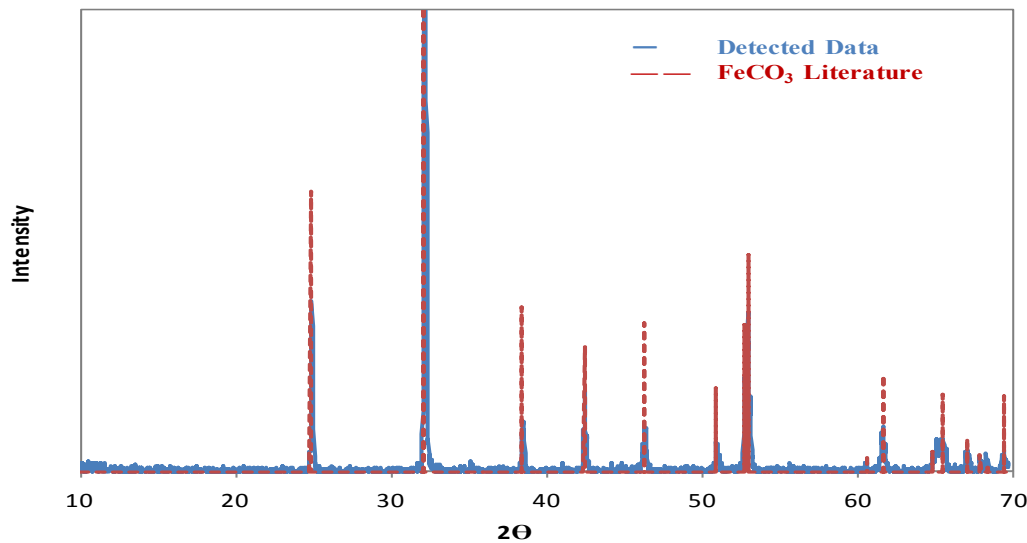


Figure 14. XRD data of recovered carbon steel specimen (CS1018) from bulk solution at 80°C and pCO<sub>2</sub> 0.5 bar with 10 ppm Fe<sup>2+</sup> and no Ca<sup>2+</sup>.

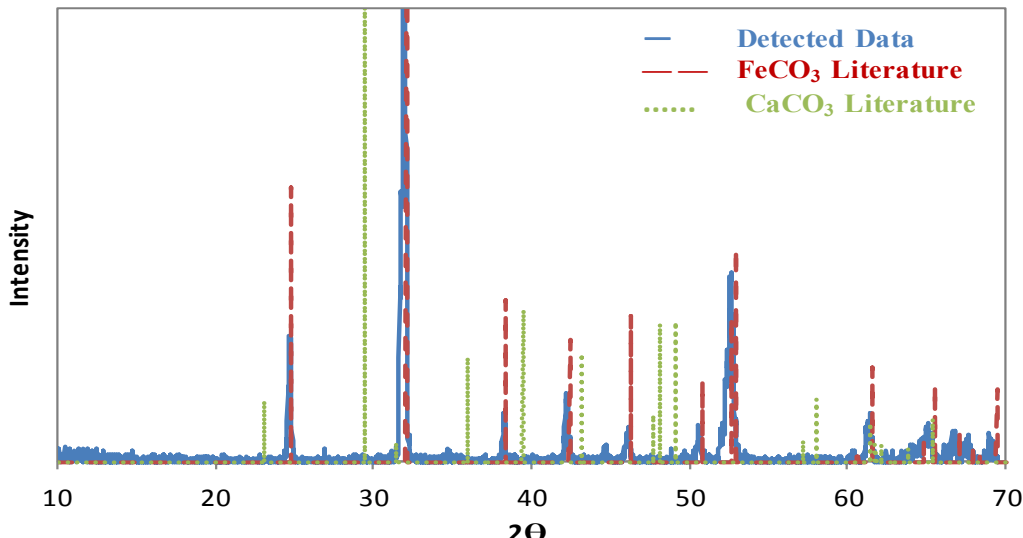


Figure 15. XRD data of recovered carbon steel specimen (CS1018) from bulk solution at 80°C and pCO<sub>2</sub> 0.5 bar with 10 ppm Fe<sup>2+</sup> and 10 ppm Ca<sup>2+</sup>.

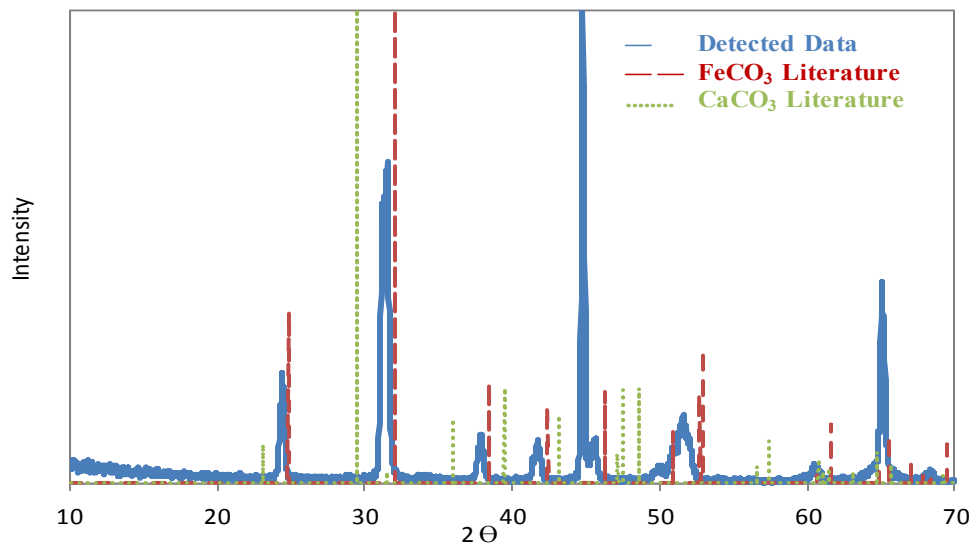


Figure 16. XRD data of recovered carbon steel specimen (CS1018) from bulk solution at 80°C and pCO<sub>2</sub> 0.5 bar with 10 ppm Fe<sup>2+</sup> and 100 ppm Ca<sup>2+</sup>.

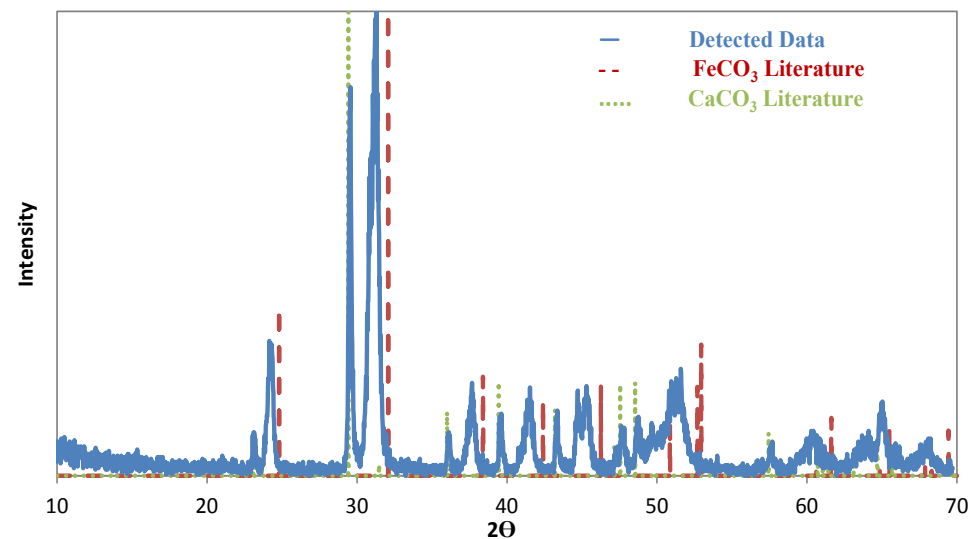


Figure 17. XRD data of recovered carbon steel specimen (CS1018) from bulk solution at 80°C and pCO<sub>2</sub> 0.5 bar with 10 ppm Fe<sup>2+</sup> and 1,000 ppm Ca<sup>2+</sup>.

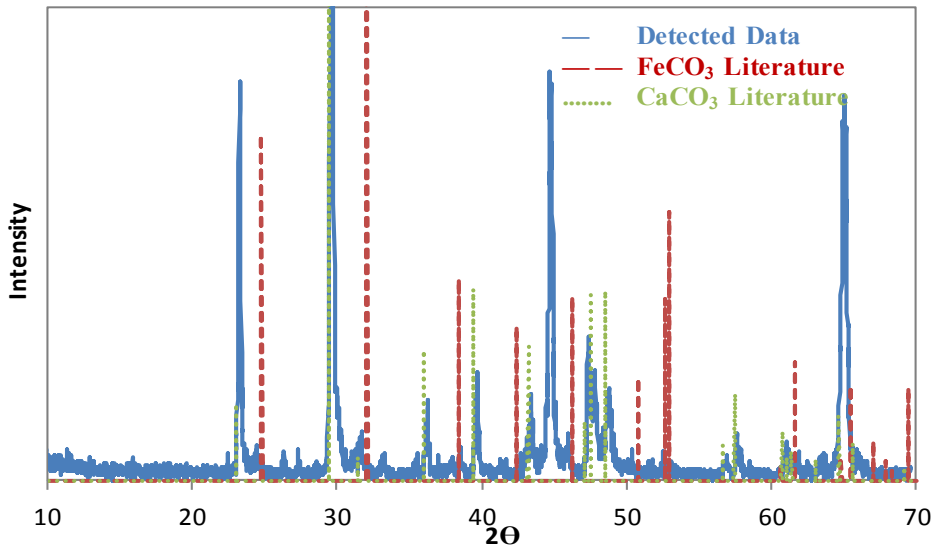
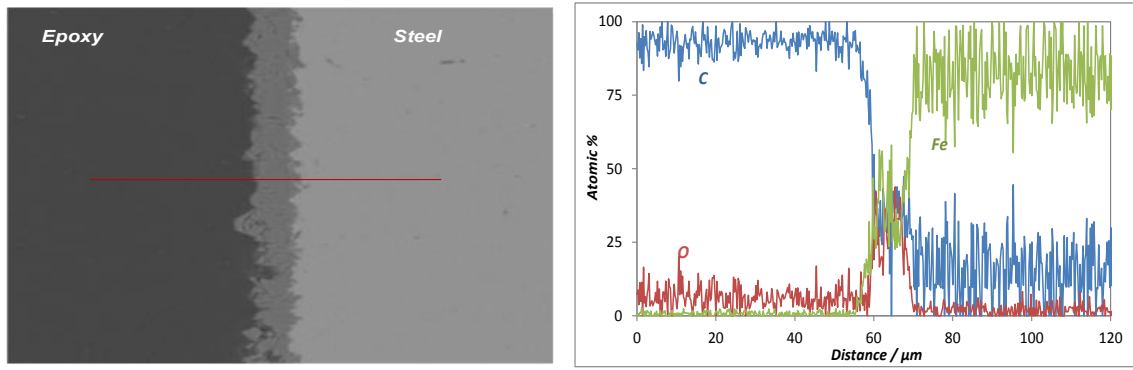


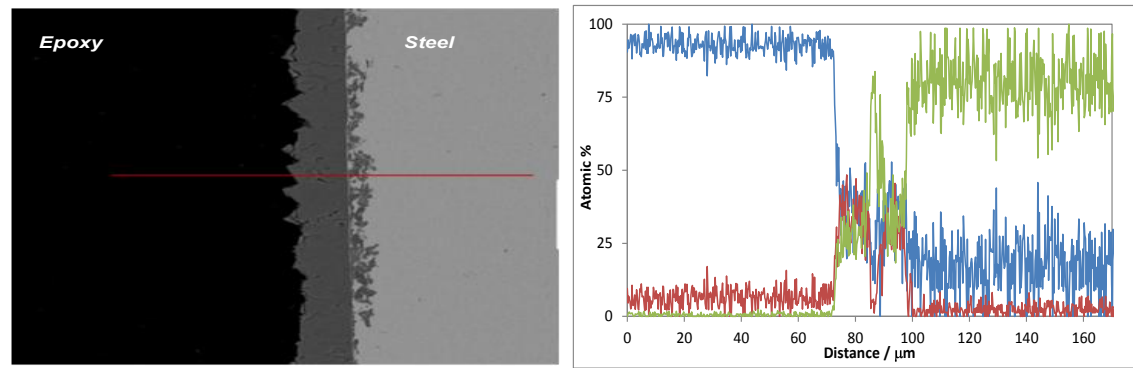
Figure 18. XRD data of recovered carbon steel specimen (CS1018) from bulk solution at 80°C and pCO<sub>2</sub> 0.5 bar with 10 ppm Fe<sup>2+</sup> and 10,000 ppm Ca<sup>2+</sup>.

Figure 19 shows the cross sectional analysis of the tested samples with 0, 10, 1,000 and 10,000 ppm Ca<sup>2+</sup>. According to Figure 19 (a) and (b), there is no significant difference in the layer on the surface with 0 and 10 ppm of Ca<sup>2+</sup>. On the other hand, in the presence of 1,000 ppm Ca<sup>2+</sup>, two different layers on the steel surface were detected. According to the EDS line scanning result in Figure 19(c), the concentration of Fe<sup>2+</sup> in the layer immediately adjacent to the steel surface is higher than for Ca<sup>2+</sup> whereas the layer on the outer surface is the opposite. Recall that the XRD data shows two distinct phases: Fe<sub>x</sub>Ca<sub>y</sub>CO<sub>3</sub> ( $x + y = 1$ ) and CaCO<sub>3</sub>. Taken in conjunction with the cross-section analysis, this would imply that a bilayer structure had formed with CaCO<sub>3</sub> scale growing from the surface of the Fe<sub>x</sub>Ca<sub>y</sub>CO<sub>3</sub> corrosion product. Figure 19(d), the cross section analysis of the experiment with 10,000 ppm Ca<sup>2+</sup>, does not show an obvious bilayer structure at the steel surface. There is, however, a significant Ca<sup>2+</sup>/Fe<sup>2+</sup> concentration

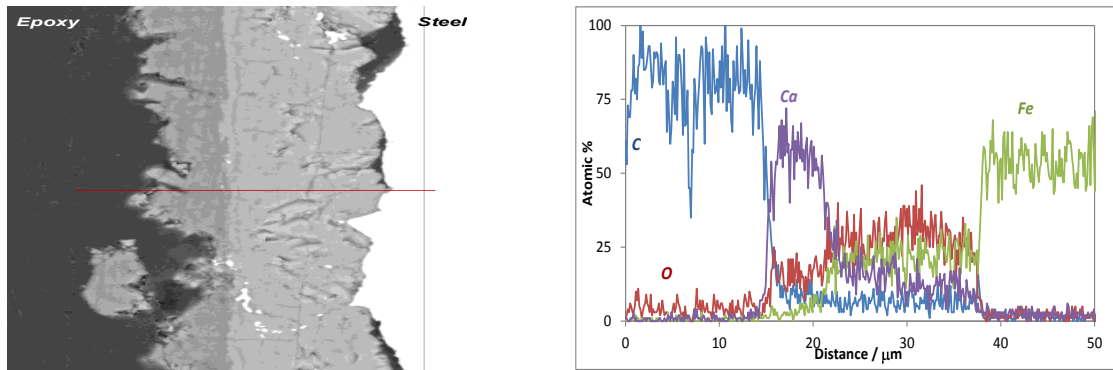
gradient, consistent with the XRD data. Note that the cross section image of the experiment with 10,000 ppm  $\text{Ca}^{2+}$  shows a non-uniform corrosion attack.



(a)



(b)



(c)

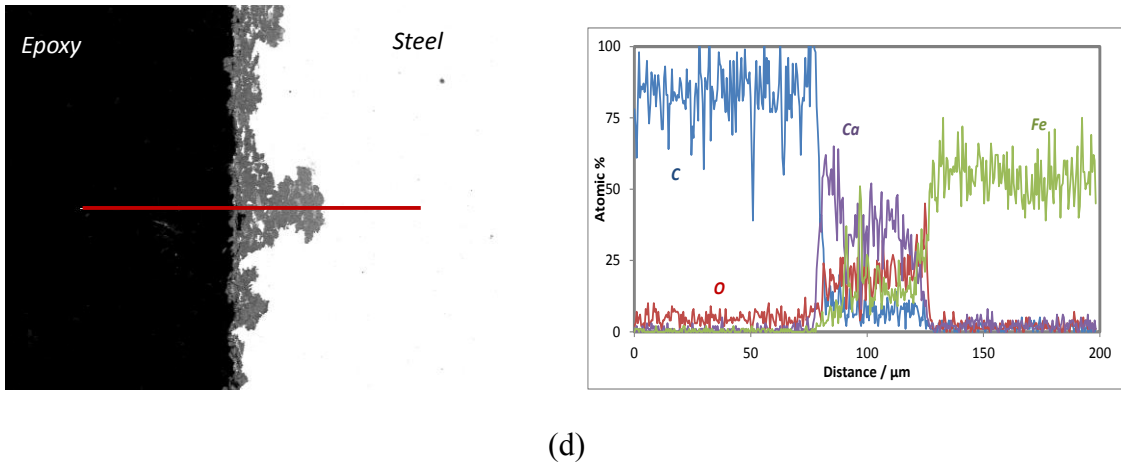


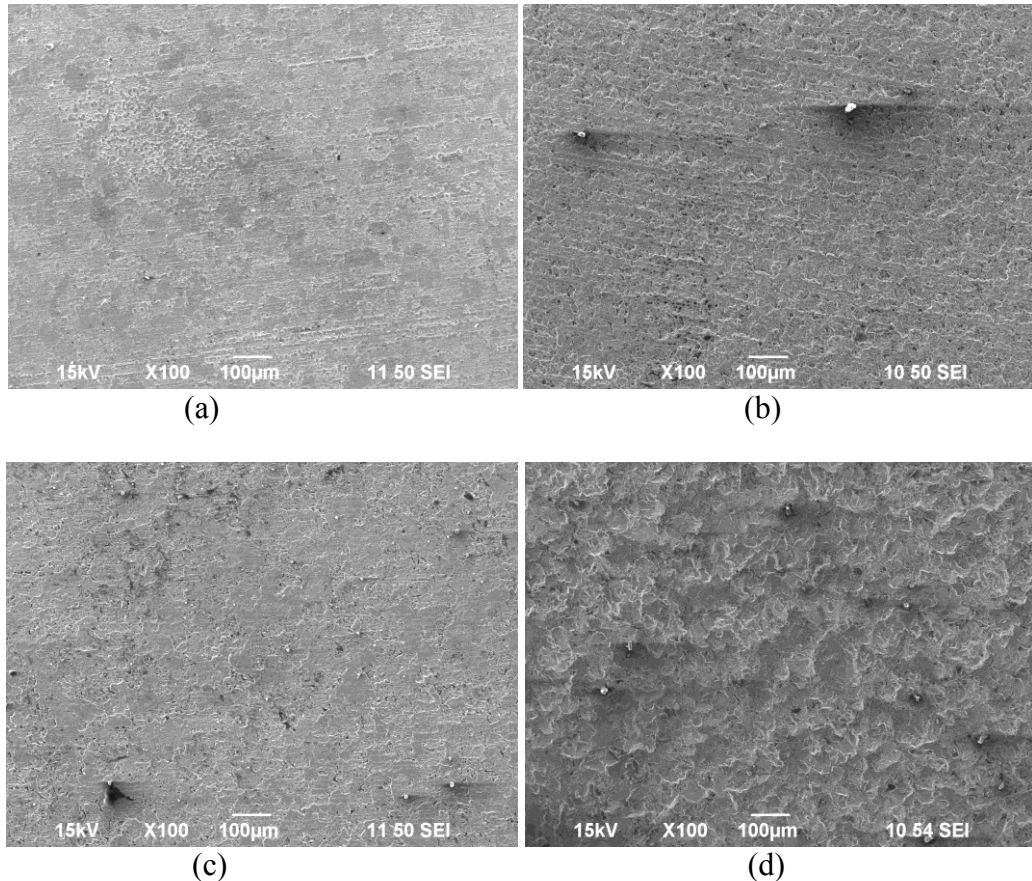
Figure 19. Cross section image and EDS spectra taken on carbon steel specimen (CS1018) surface of the bulk solution with 10 ppm  $\text{Fe}^{2+}$  (a) no  $\text{Ca}^{2+}$  (b) 10 ppm  $\text{Ca}^{2+}$  (c) 100 ppm  $\text{Ca}^{2+}$  (d) 10,000 ppm  $\text{Ca}^{2+}$  at 80 °C and  $\text{pCO}_2$  0.5 bar after 7 days.

One of the objectives of this study was to investigate the possibility of non-uniform corrosion behavior. In order to investigate the tested samples for localized attack, the precipitated layer was chemically removed by Clarke solution [41]. Figure 20 (a), (b), (c), and (d) show the surface of each sample after removing the corrosion product layers for experiments conducted at 0, 10, 100, 1,000 ppm  $\text{Ca}^{2+}$ , respectively. The corrosion attack was uniform for these conditions. However, the recovered sample from the bulk solution with 10,000 ppm  $\text{Ca}^{2+}$  revealed a non-uniform attack: Figure 20 (e). A non-uniform corrosion behavior was reported by Jiang *et al.*, Ren *et al.* and Zhu *et al.* in the presence of  $\text{CaCl}_2$ . However the non-uniform attack of corrosion was blamed on the effect of chloride not calcium[34], [36], [38].

Figure 21 shows the pit depths measured by IFM. The deepest pits were about 100  $\mu\text{m}$ . The non-uniform (pitting) corrosion rate is calculated according to Equation

(26), which gives a rate of 6 mm/yr. The weight loss corrosion rate according to Equation (12) was 0.7 mm/yr, which gives a pitting ratio of 8.5 based on Equation (13).

The comparison of weight loss corrosion rate and pitting corrosion rate helps to determine the dominant corrosion behavior. The ratio of pitting corrosion rate to weight loss corrosion rate indicates uniform *vs.* non-uniform corrosion behavior. To evaluate the behavior of corrosion in terms of whether it is uniform or non-uniform, a combination of factors should be taken into account[42]. Singer *et al.* proposed a criterion for pitting attack. A pitting ratio of 5 or larger is considered a pitting attack [43]. However, it is hypothesized that the ratio of 3 or larger is an indication of the localized attack [44].



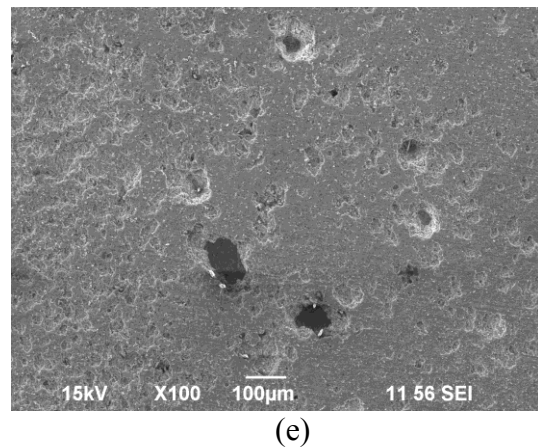


Figure 20. Surfaces after corrosion product removal of the carbon steel specimen (CS1018) surface of the bulk solution with 10 ppm  $\text{Fe}^{2+}$  (a) no  $\text{Ca}^{2+}$  (b) 10 ppm  $\text{Ca}^{2+}$  (c) 100 ppm  $\text{Ca}^{2+}$  (d) 1,000 ppm  $\text{Ca}^{2+}$  (e) 10,000 ppm  $\text{Ca}^{2+}$  at 80 °C and  $\text{pCO}_2$  0.5 bar after 7 days.

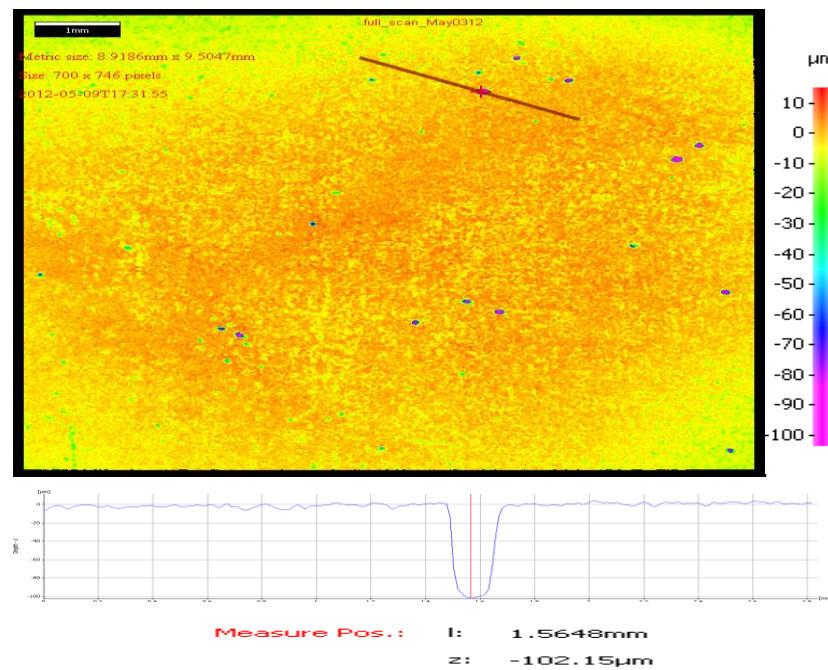


Figure 21. IFM of carbon steel specimen (CS1018) after removal of corrosion product for the experiment conducted at 80°C and  $\text{pCO}_2$  0.5 bar with 10 ppm  $\text{Fe}^{2+}$  + 10,000 ppm  $\text{Ca}^{2+}$ .

One of the concerns of the effect of  $\text{Ca}^{2+}$  on corrosion is that  $\text{Ca}^{2+}$ , even at low concentration, substitutes into the  $\text{FeCO}_3$  structure, as shown in Figure 13 b and c. If this substitution occurs inhomogeneously, the formed  $\text{Fe}_x\text{Ca}_y\text{CO}_3$  layer may not be uniformly stable under conditions where the pH fluctuates. Consequently, there is always a possibility of selective local dissolution of the corrosion product layer. Put another way, in the case of pure  $\text{FeCO}_3$  any dissolution of the lattice occurs uniformly. However, if  $\text{Ca}^{2+}$  is distributed inhomogeneously within the lattice, the structure would be liable to undergo selective dissolution. Consequently, the corrosion behavior in cases where  $\text{Ca}^{2+}$  is present in the  $\text{FeCO}_3$  lattice would be expected to be different. In the next set of experiments, this effect was studied by challenging the integrity of the corrosion product layer by varying the pH; studied electrolytes corresponded to 0, 10 and 100 ppm  $\text{Ca}^{2+}$ . As soon as the corrosion rate in these experiments reached a stable point as a result of the formation of a protective layer on the surface of the sample, the pH was slightly decreased by adding HCl. The results are presented in the following section.

### **Effect of pH fluctuation on corrosion in the presence of calcium**

Figure 22 shows the OCP variation over time for three different environments: 0, 10 and 100 ppm  $\text{Ca}^{2+}$ . The pH was slightly changed by the addition of deoxygenated HCl after a stable corrosion rate was obtained for each experiment. The corrosion potential behavior shows that all three systems were under anodic reaction control. The increase in the potential along with an increase in the corrosion rate as presented in Figure 23 for each case explains that the drop in pH promotes the oxidation of the steel surface.

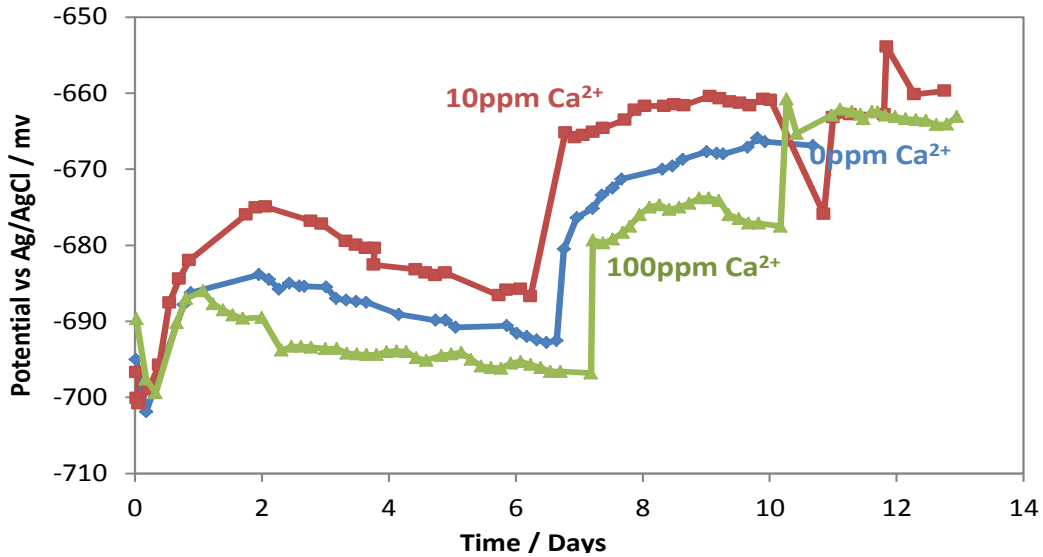


Figure 22. Variations of open circuit potential of carbon steel specimen (CS1018) for the experiments with different initial concentrations of  $\text{Ca}^{2+}$  (0, 10 and 100 ppm).

Figure 23 represents the corrosion behavior *versus* time. In each experiment, after the stable corrosion rate was achieved, the ferrous iron concentration was measured. Using Equation (15), the required concentration of  $\text{CO}_3^{2-}$  to have the system with a  $\text{FeCO}_3$  saturation degree between 1 and 2 was calculated in relation to the desired pH. Thus, when pH dropped the solution continued to be supersaturated with respect to  $\text{FeCO}_3$ . The electrolyte was undersaturated with respect to  $\text{CaCO}_3$ . Note that  $\text{CaCO}_3$  is more soluble than  $\text{FeCO}_3$  with 2 order of magnitude difference [30]. It made it achievable to have a supersaturated solution with respect to  $\text{FeCO}_3$  while it was under saturated with respect to  $\text{CaCO}_3$ , even if we assumed that the total amount of initially added  $\text{Ca}^{2+}$  (10 and 100 ppm) was still in the solution and not precipitated on the surface of the sample.

The corrosion rate increased in all three conditions. The higher increase in the corrosion rate of the systems with 10 and 100 ppm  $\text{Ca}^{2+}$  could be the result of the

presence of  $\text{Fe}_x\text{Ca}_y\text{CO}_3$  ( $x + y = 1$ ) on the surface along with the  $\text{FeCO}_3$ . Thus, drops in pH would lead to the dissolving of the more soluble components of the formed  $\text{Fe}_x\text{Ca}_y\text{CO}_3$  solid solution back into the electrolyte.

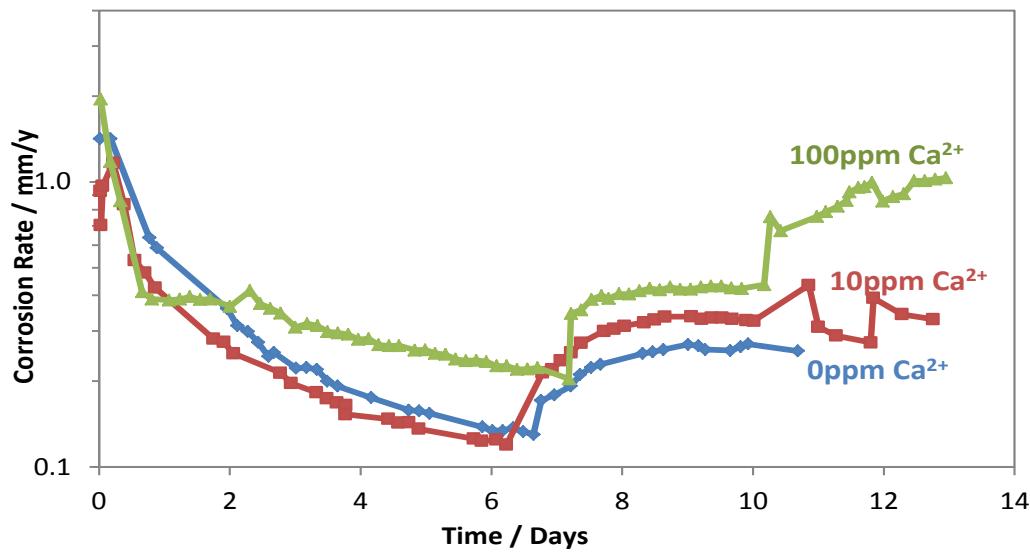


Figure 23. Variations of corrosion rate of carbon steel specimen (CS1018) for the experiments with different initial concentrations of  $\text{Ca}^{2+}$  (0, 10 and 100 ppm).

Figure 24 shows the pH behavior over time. The pH dropped after 6 days in all three tested conditions. For the experiments with 10 and 100 ppm  $\text{Ca}^{2+}$  pH was adjusted twice to ensure that the system remained under-saturated with respect to  $\text{CaCO}_3$ . Due to the higher corrosion rate for these two experiments the  $\text{C}(\text{Fe}^{2+})$  kept increasing.

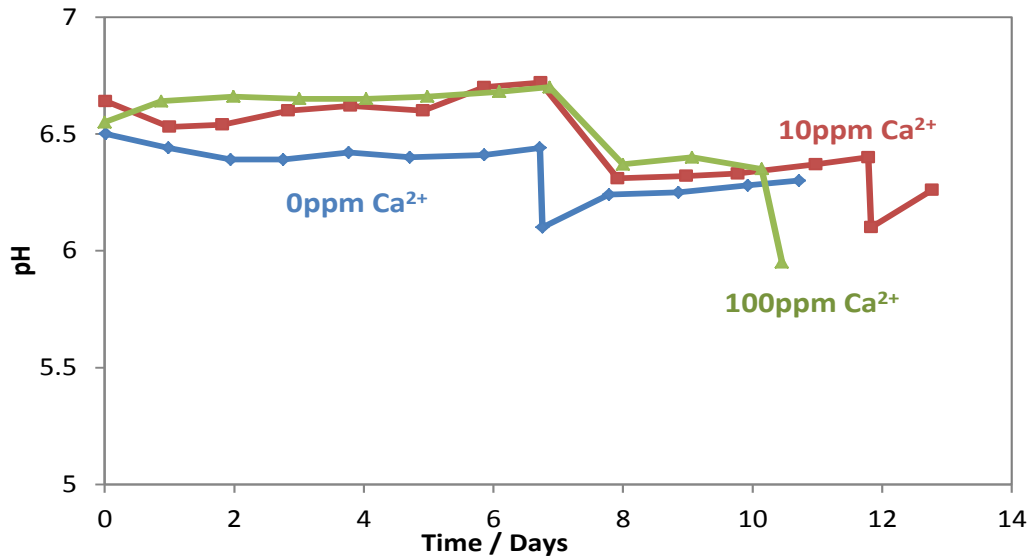


Figure 24. Variations of pH of the system for the experiments with different initial concentrations of  $\text{Ca}^{2+}$  (0, 10 and 100 ppm).

Figure 25 represents the  $\text{Fe}^{2+}$  concentrations over time. As is shown, the  $\text{C}(\text{Fe}^{2+})$  kept decreasing in the first 150 hours consistent with corrosion rate behavior. This is consistent with the formation of  $\text{FeCO}_3$ , thermodynamically plausible according to Figure 26; all three conditions were supersaturated with respect to  $\text{FeCO}_3$ . After the pH was decreased for each condition, the  $\text{C}(\text{Fe}^{2+})$  kept increasing due to the increase in corrosion rate.

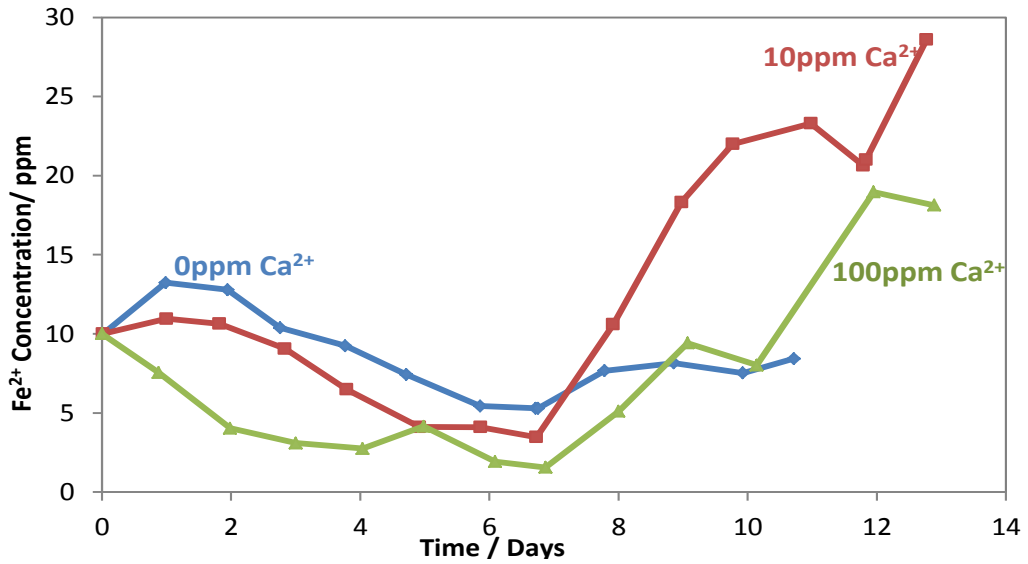


Figure 25. Variations of  $\text{Fe}^{2+}$  concentration of the system for the experiments with different initial concentrations of  $\text{Ca}^{2+}$  (0, 10 and 100 ppm).

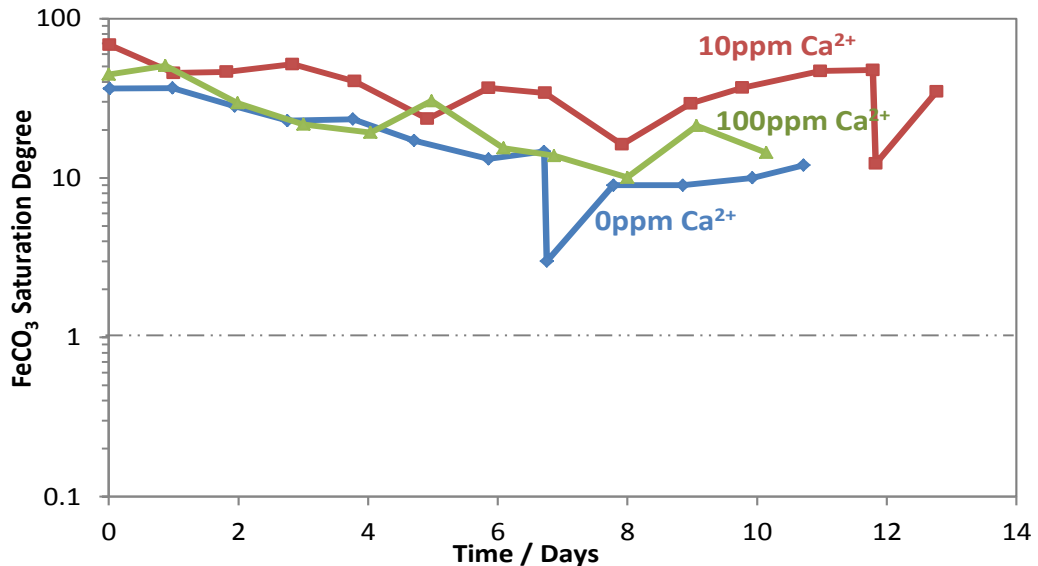


Figure 26. Variation of  $\text{FeCO}_3$  saturation degree for the experiments with different initial concentrations of  $\text{Ca}^{2+}$  (0, 10 and 100 ppm).

Figure 27 shows the SEM image and EDS spectra of the samples for the experiment with no  $\text{Ca}^{2+}$  before changing the pH to the value which results in , an under

saturated solution with respect to  $\text{CaCO}_3$ . In Figure 27 (a) the surface is incompletely covered by large prismatic crystals of  $\text{FeCO}_3$ . The EDS data in Figure 27 (b) indicates that even those areas uncovered actually have a thin corrosion product layer with a composition and morphology consistent with formation of either  $\text{FeCO}_3$  or  $\text{Fe}_2(\text{OH})_2\text{CO}_3$ [21], [45].

Figure 28 shows the SEM image and EDS spectra of the samples of the experiment with no  $\text{Ca}^{2+}$  after dropping the pH. Figure 28 (a) shows that even after changing the pH, the surface was covered by the  $\text{FeCO}_3$  crystals. EDS spectra in Figure 28 (b) support the presence of  $\text{FeCO}_3$  on the steel surface.

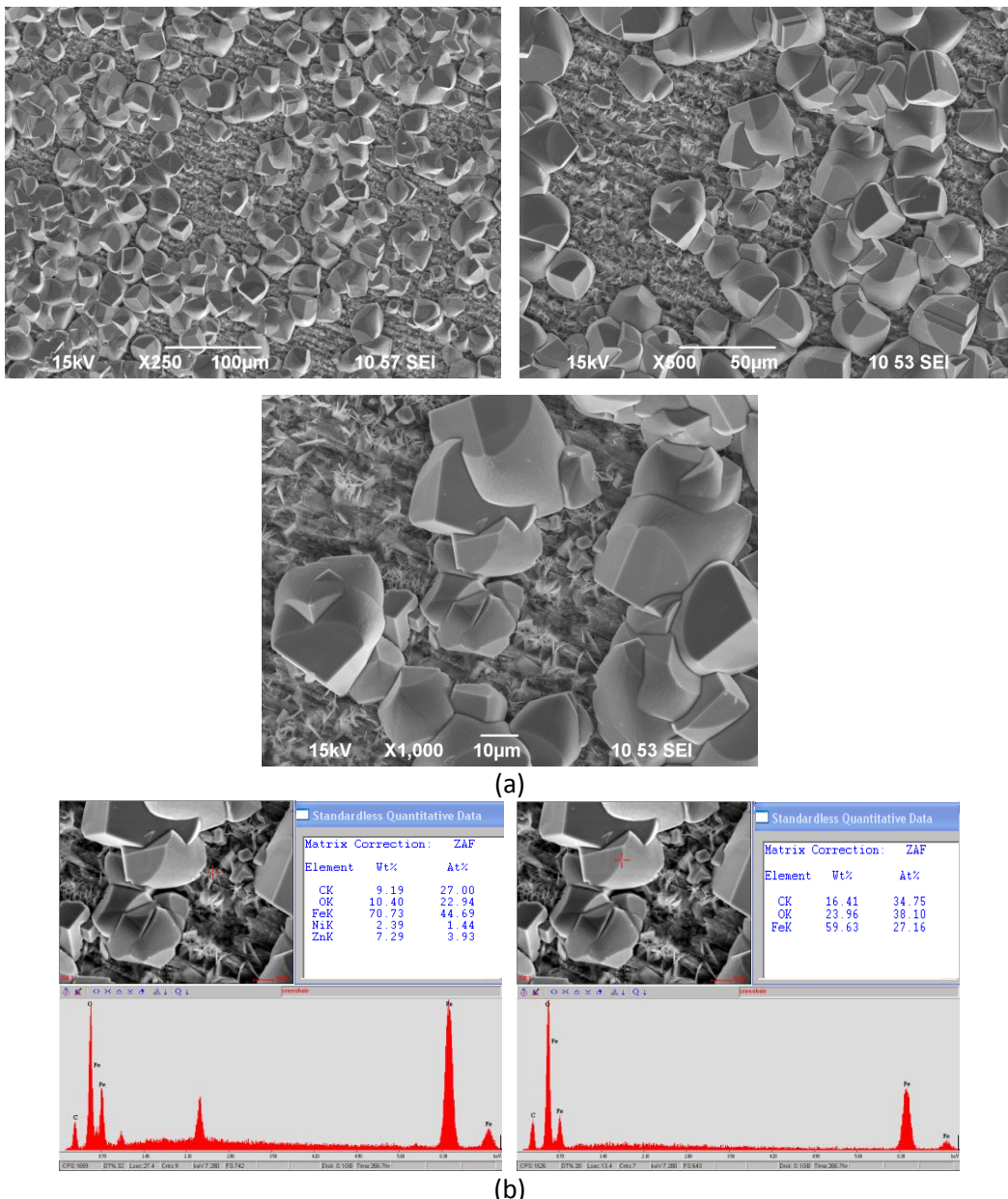


Figure 27. SEM images and EDS spectra taken on carbon steel specimen (CS1018) surface of the bulk solution with 10 ppm Fe<sup>2+</sup> and no Ca<sup>2+</sup> at 80 °C and pCO<sub>2</sub> 0.5 bar before changing the pH.

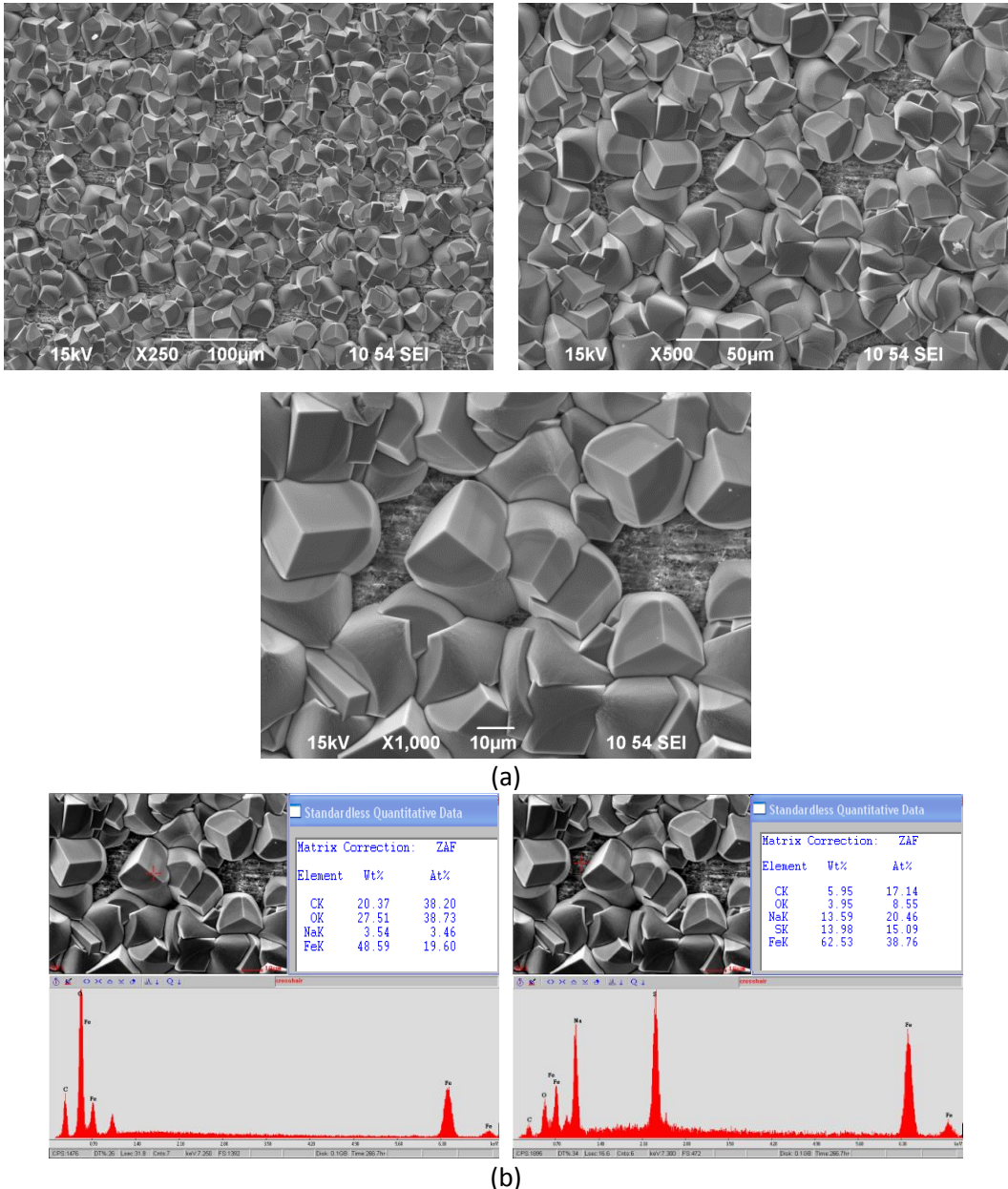


Figure 28. SEM images and EDS spectra taken on carbon steel specimen (CS1018) surface of the bulk solution with 10 ppm Fe<sup>2+</sup> and no Ca<sup>2+</sup> at 80 °C and pCO<sub>2</sub> 0.5 bar after changing the pH.

Figure 29 shows the cross sectional analysis of the sample in the experiment with no Ca<sup>2+</sup> removed at the end of the experiment. As was expected and shown in Figure 28 the surface was covered by the FeCO<sub>3</sub> layer.

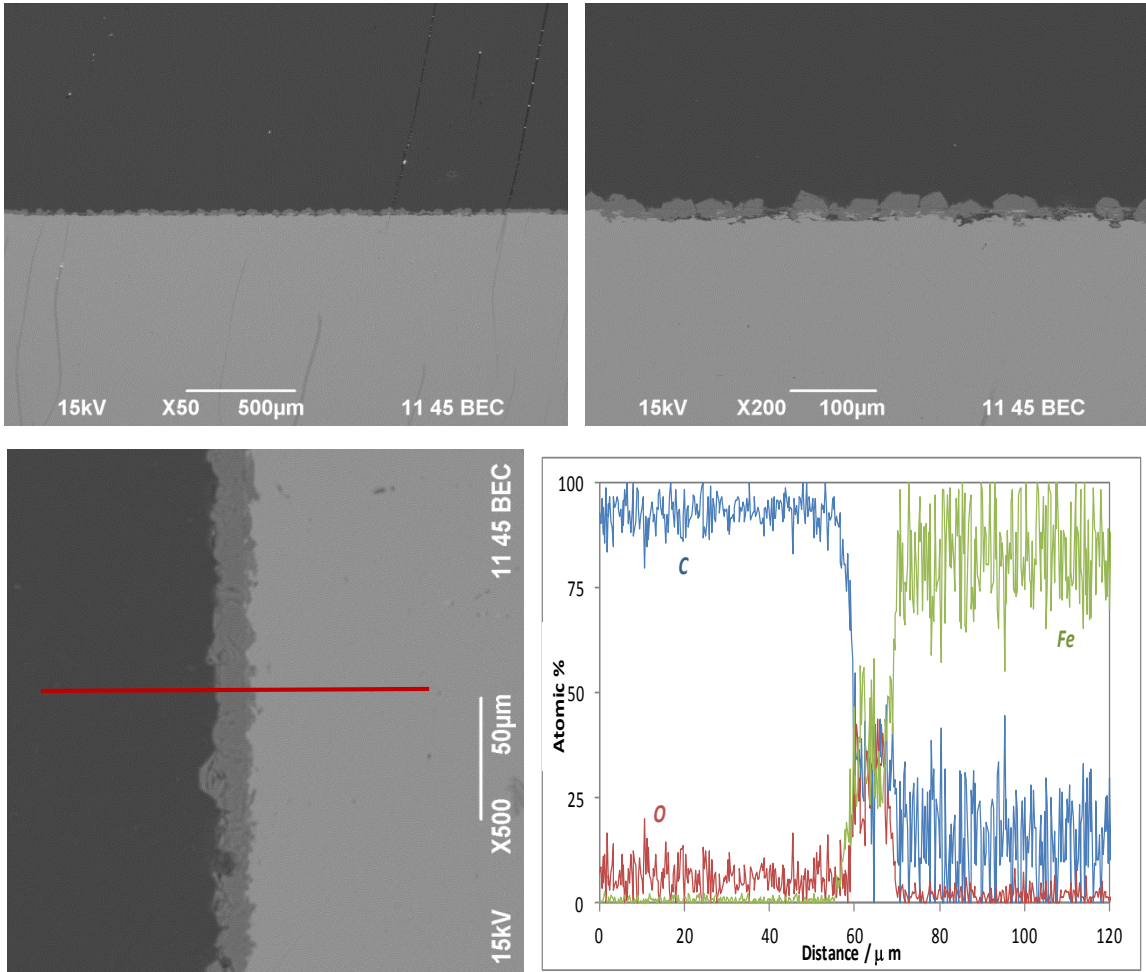


Figure 29. Cross section image and EDS spectra taken on carbon steel specimen (CS1018) of the bulk solution with 10 ppm  $\text{Fe}^{2+}$  and no  $\text{Ca}^{2+}$  at 80 °C and  $\text{pCO}_2$  0.5 bar.

Figure 30 shows the sample surfaces after specimens were treated with Clarke solution [41]. According to Figure 23 the corrosion rate increased due to the change in pH. However, the pH drop did not lead to non-uniform corrosion behavior.

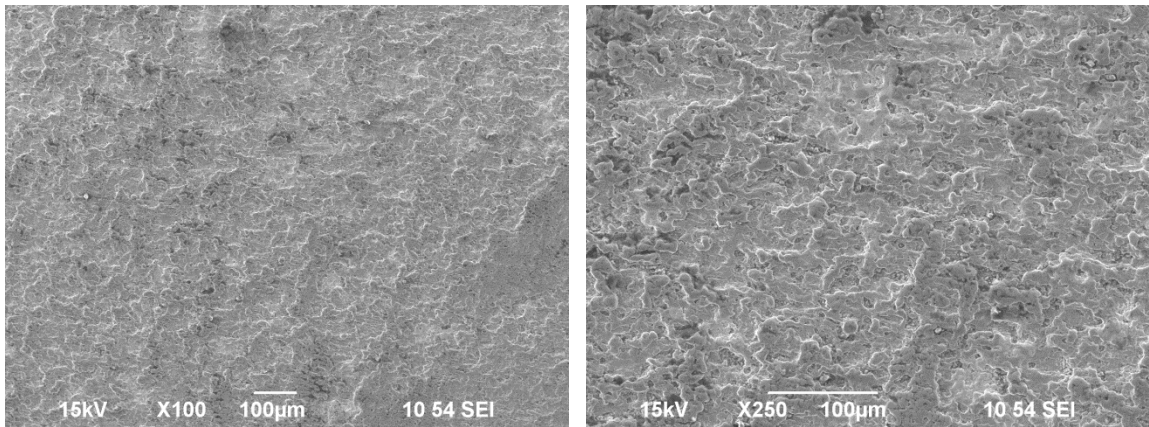


Figure 30. Surfaces after corrosion product removal of the carbon steel specimen (CS1018) surface of the bulk solution with 10 ppm  $\text{Fe}^{2+}$  and no  $\text{Ca}^{2+}$  at 80 °C and  $\text{pCO}_2$  0.5 bar.

Figure 31 shows the SEM image and EDS spectra of the sample from the experiment with 10 ppm  $\text{Ca}^{2+}$  before changing the pH. Figure 31 (a) shows a relatively similar morphology of crystals on the steel surface to what was previously shown for the calcium-free system. Figure 31 (b) shows substitution of  $\text{Ca}^{2+}$  into the structure of  $\text{FeCO}_3$ .

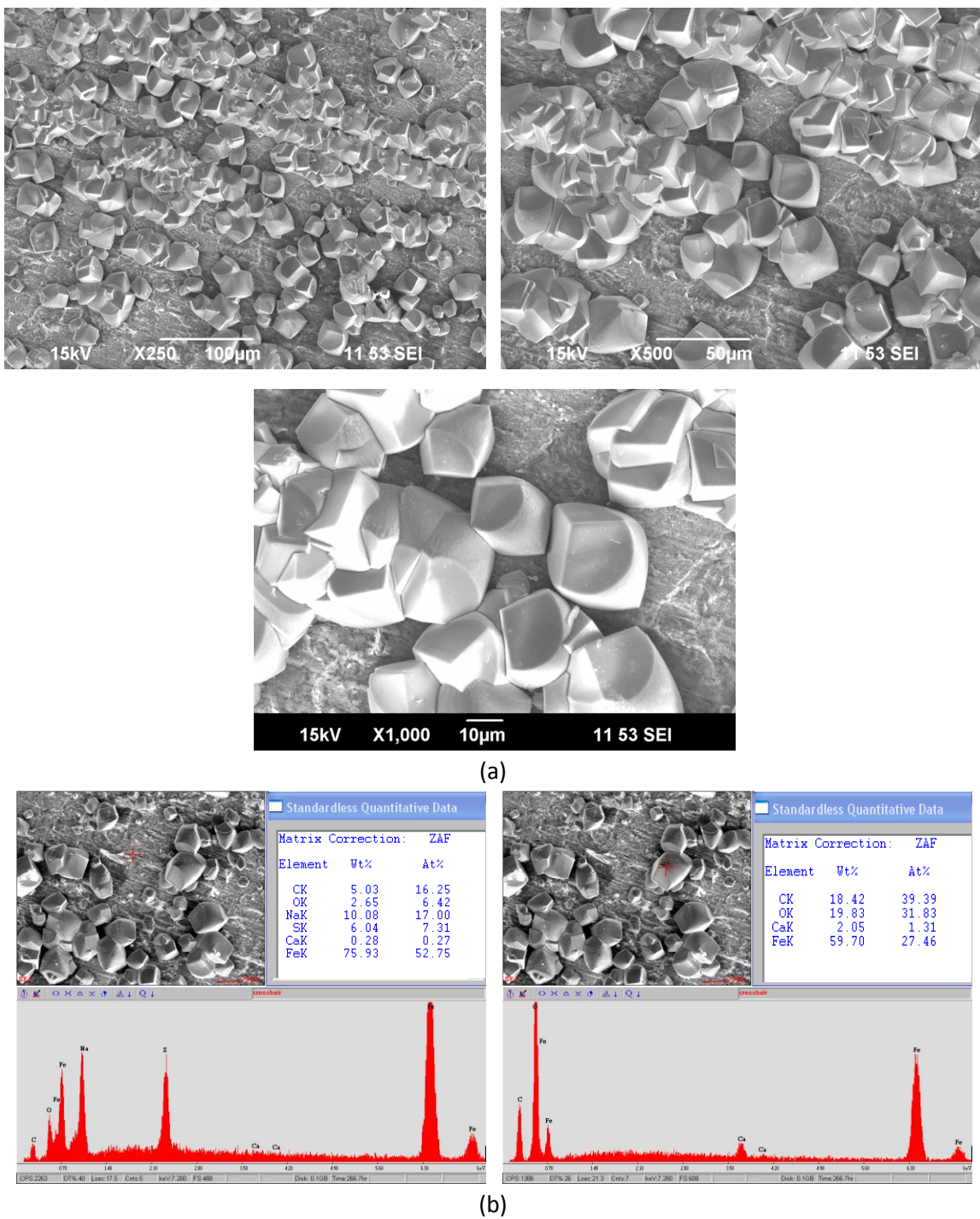


Figure 31. SEM images and EDS spectra taken on carbon steel specimen (CS1018) surface of the bulk solution with 10 ppm  $\text{Fe}^{2+}$  and 10 ppm  $\text{Ca}^{2+}$  at 80 °C and  $\text{pCO}_2$  0.5 bar before changing the pH.

The pH was decreased in two steps in the experiment with 10 ppm  $\text{Ca}^{2+}$ . Figure 32 shows the SEM image and EDS spectra of the sample from the experiment with 10 ppm  $\text{Ca}^{2+}$  after the first drop in the pH. Figure 32 (a) shows the distribution of the crystals on the surface after dropping the pH. According to Figure 32 (b), it seems even the visually uncovered area had a  $\text{FeCO}_3$  layer. A trace of  $\text{Ca}^{2+}$  could be detected by EDS in the crystals of  $\text{FeCO}_3$  even after changing the pH to a value in which the solution is under-saturated with respect to  $\text{CaCO}_3$ . This indicates that the solution was still supersaturated with respect to  $\text{Fe}_x\text{Ca}_y\text{CO}_3$  ( $x+y=1$ ). Figure 33 shows the SEM image and EDS spectra of the sample from the experiment with 10 ppm  $\text{Ca}^{2+}$  after the second drop in the pH. Figure 33 (a) shows the distribution of the crystals on the surface. Even after 2<sup>nd</sup> imposed drop in pH Figure 33 (b) shows a significant, if reduced, concentration of  $\text{Ca}^{2+}$  in the structure of the  $\text{FeCO}_3$ . This would be equivalent to substitution of ~2% of the  $\text{Fe}^{2+}$  with  $\text{Ca}^{2+}$  in the  $\text{FeCO}_3$  crystal lattice, down from a value of ~5% prior to and immediately after the first acidification; note that this would be consistent with the presence of calcium-substituted siderites with the formulae  $\text{Fe}_{0.98}\text{Ca}_{0.02}\text{CO}_3$  and  $\text{Fe}_{0.95}\text{Ca}_{0.05}\text{CO}_3$ , respectively. Note, too, the surface damage to the siderite crystals. Taken with the reduction in  $\text{Ca}^{2+}$  incorporation in the siderite lattice, this would be consistent with surface enrichment of the  $\text{FeCO}_3$  crystals with calcium and preferential dissolution due to this compositional inhomogeneity.

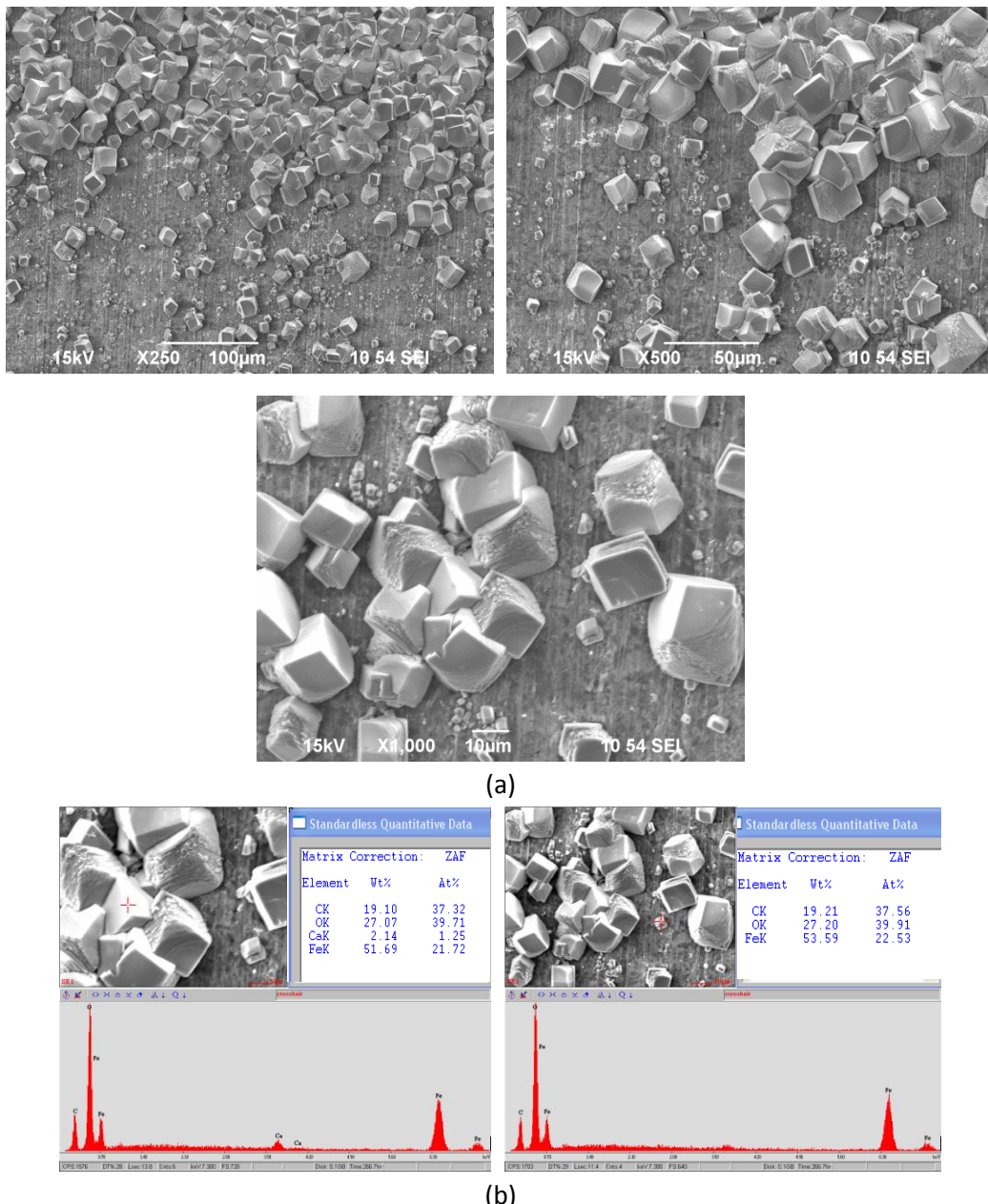


Figure 32. SEM images and EDS spectra taken on carbon steel specimen (CS1018) surface of the bulk solution with 10 ppm  $\text{Fe}^{2+}$  and 10 ppm  $\text{Ca}^{2+}$  at 80 °C and  $\text{pCO}_2$  0.5 bar after the 1<sup>st</sup> drop in the pH.

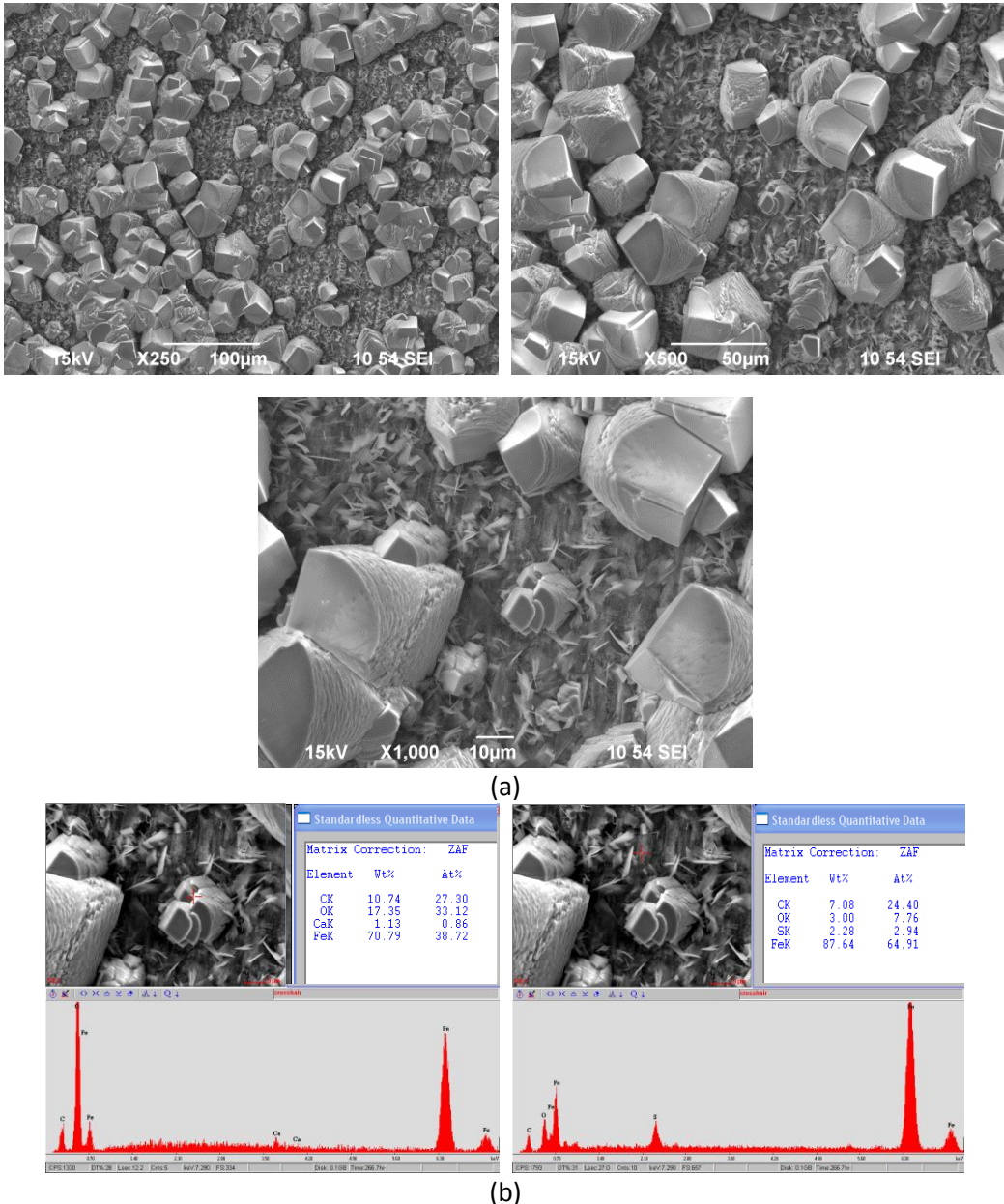


Figure 33. SEM images and EDS spectra taken on carbon steel specimen (CS1018) surface of the bulk solution with 10 ppm  $\text{Fe}^{2+}$  and 10 ppm  $\text{Ca}^{2+}$  at 80 °C and  $\text{pCO}_2$  0.5 bar after the 2<sup>nd</sup> drop in the pH.

Figure 34 shows the cross-sectional analysis of the sample in the environment with 10 ppm  $\text{Ca}^{2+}$  recovered at the end of the experiment. As was expected, and shown in

Figure 33, the surface was covered by an iron carbonate layer. However, the line scanning EDS did not detect  $\text{Ca}^{2+}$ . This further confirms that the trace of  $\text{Ca}^{2+}$  in the crystals is confined to a thin surface enrichment region when the pH was kept relatively low.

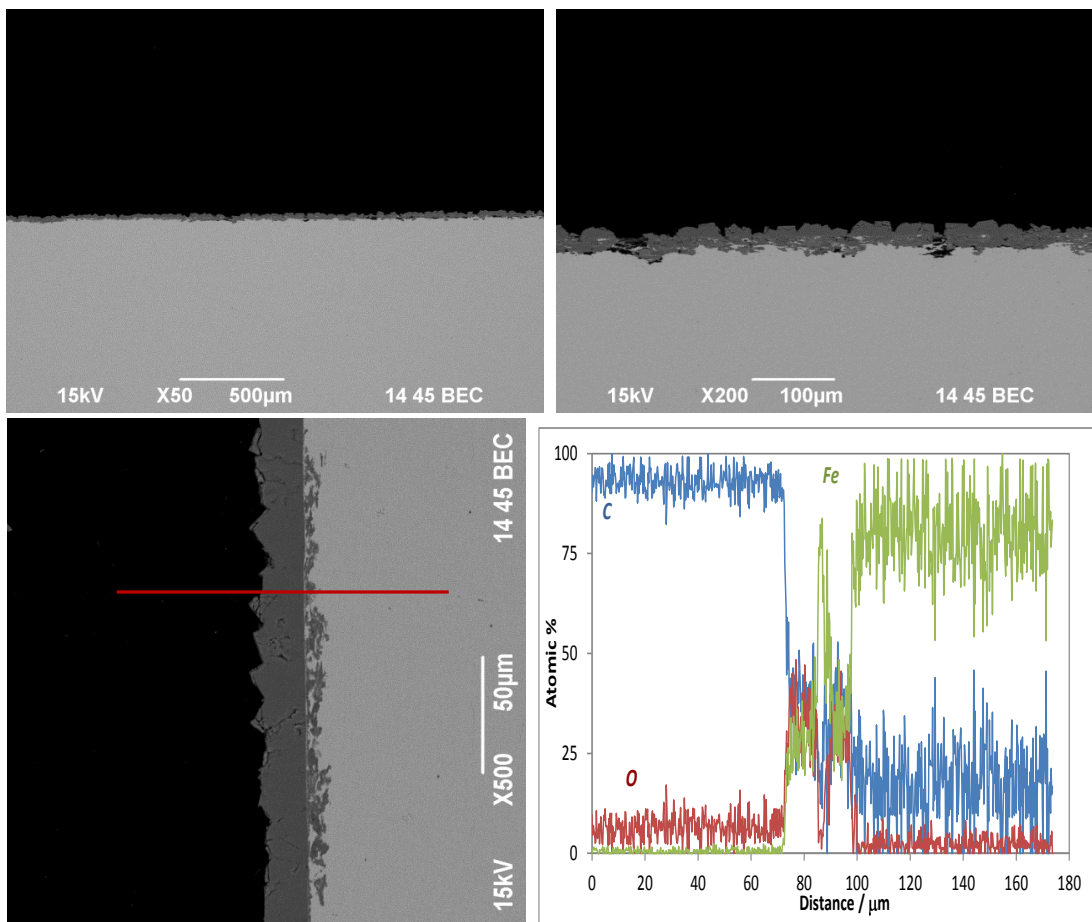


Figure 34. Cross section image and EDS spectra taken on carbon steel specimen (CS1018) of the bulk solution with 10 ppm  $\text{Fe}^{2+}$  and 10 ppm  $\text{Ca}^{2+}$  at 80 °C and  $\text{pCO}_2$  0.5 .

Figure 35 shows the sample surface after a specimen was treated with Clarke solution [41]. According to Figure 23 the corrosion rate increased due to the change in the pH and caused only a higher general corrosion rate.

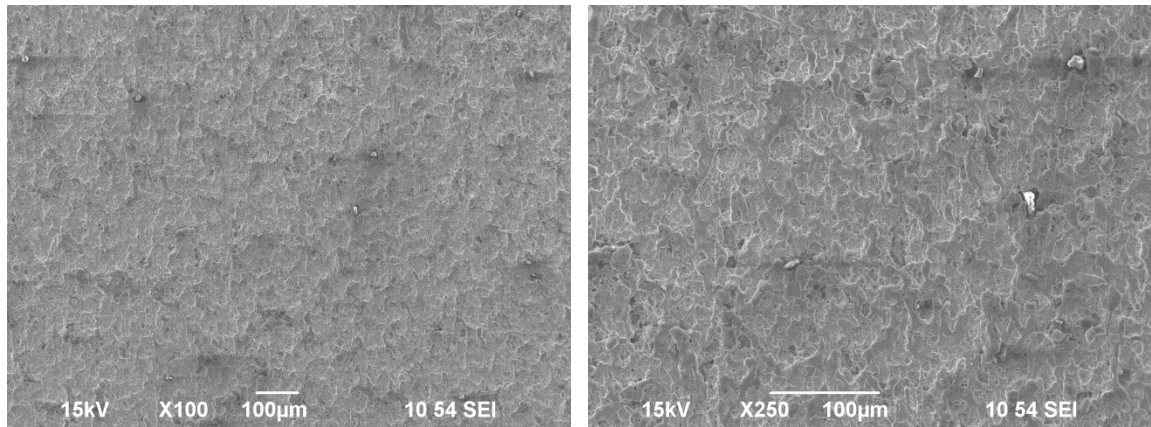


Figure 35. Surfaces after corrosion product removal of the carbon steel specimen (CS1018) surface of the bulk solution with 10 ppm  $\text{Fe}^{2+}$  and 10 ppm  $\text{Ca}^{2+}$  at 80 °C and  $\text{pCO}_2$  0.5 bar.

Figure 36 shows the SEM image and EDS spectra of the sample from the solution with 100 ppm  $\text{Ca}^{2+}$  before changing the pH. According to Figure 36 (a), before dropping the pH, the morphology of the crystals was slightly changed by the presence of  $\text{Ca}^{2+}$ . The corrosion rate, according to Figure 23, did not behave noticeably different. Figure 36 (b) shows more substitution of  $\text{Ca}^{2+}$  within the structure of  $\text{FeCO}_3$ . Given the values in the EDS spectrum, this would be consistent with formation of a calcium-substituted siderite with the formula  $\text{Fe}_{0.78}\text{Ca}_{0.22}\text{CO}_3$ .

Figure 37 shows the SEM image and EDS spectra of the sample from the experiment with 100 ppm  $\text{Ca}^{2+}$  after the first drop in the pH. Figure 37 (a) shows the crystal morphology, which again looks slightly different from the image in Figure 36.

Figure 37 (b) shows the presence of  $\text{Ca}^{2+}$  in the crystal structures, this data would again be consistent with the formation of  $\text{Fe}_{0.78}\text{Ca}_{0.22}\text{CO}_3$ .

Figure 38 shows the SEM image and EDS spectra of the sample from the experiment with 100 ppm  $\text{Ca}^{2+}$  after the second drop in the pH. Figure 38 (a) shows a relatively similar to the image in Figure 37 (a). Figure 38 (b) shows that even after dropping pH for two times there were still substitution of  $\text{Ca}^{2+}$  in the structure of the crystals. Again, based on the Fe/Ca atomic ratio, the EDS data would be consistent with the presence of  $\text{Fe}_{0.78}\text{Ca}_{0.22}\text{CO}_3$ .

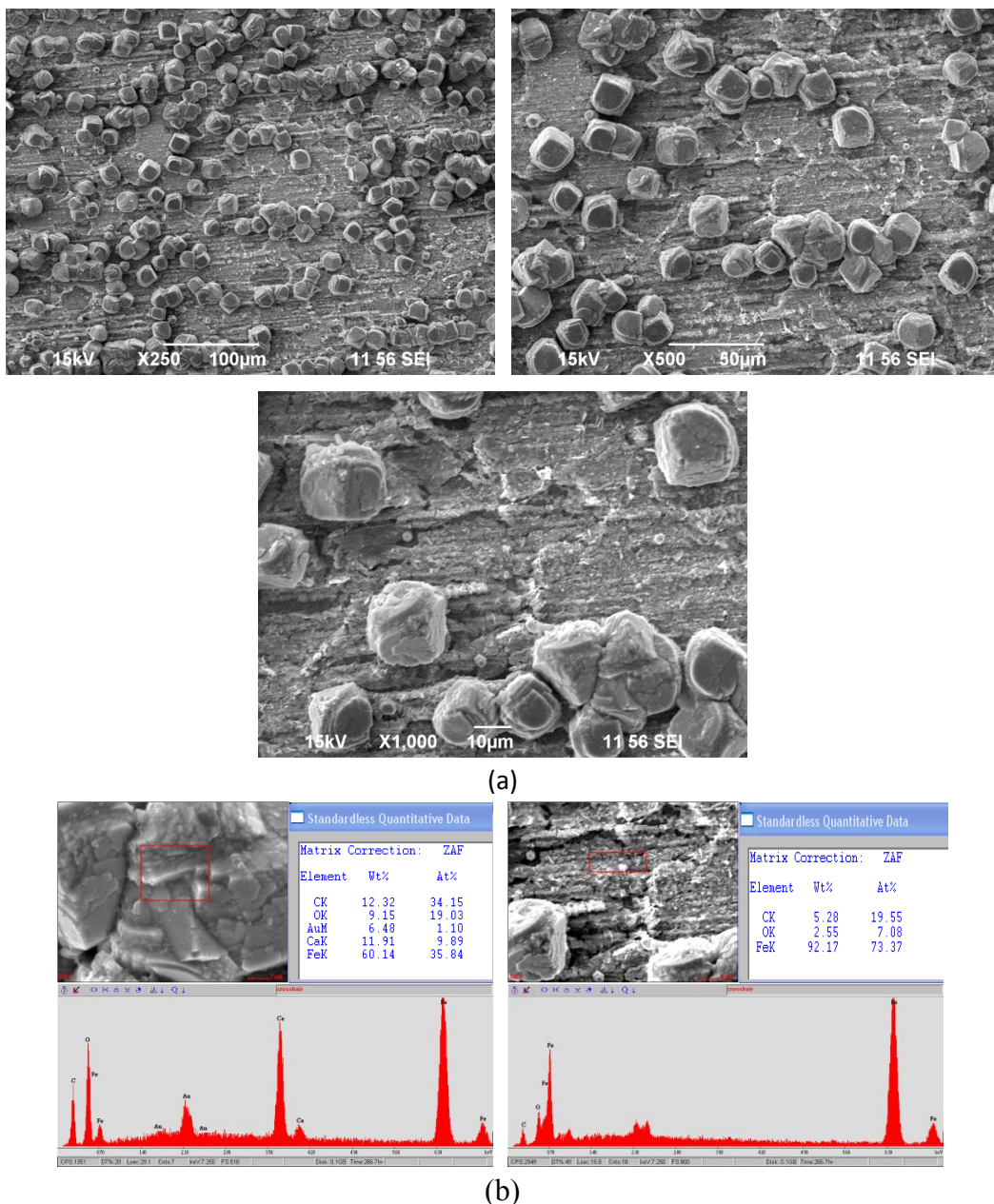


Figure 36. SEM images and EDS spectra taken on carbon steel specimen (CS1018) surface of the bulk solution with 10 ppm  $\text{Fe}^{2+}$  and 100 ppm  $\text{Ca}^{2+}$  at 80 °C and  $\text{pCO}_2$  0.5 bar before changing the pH.

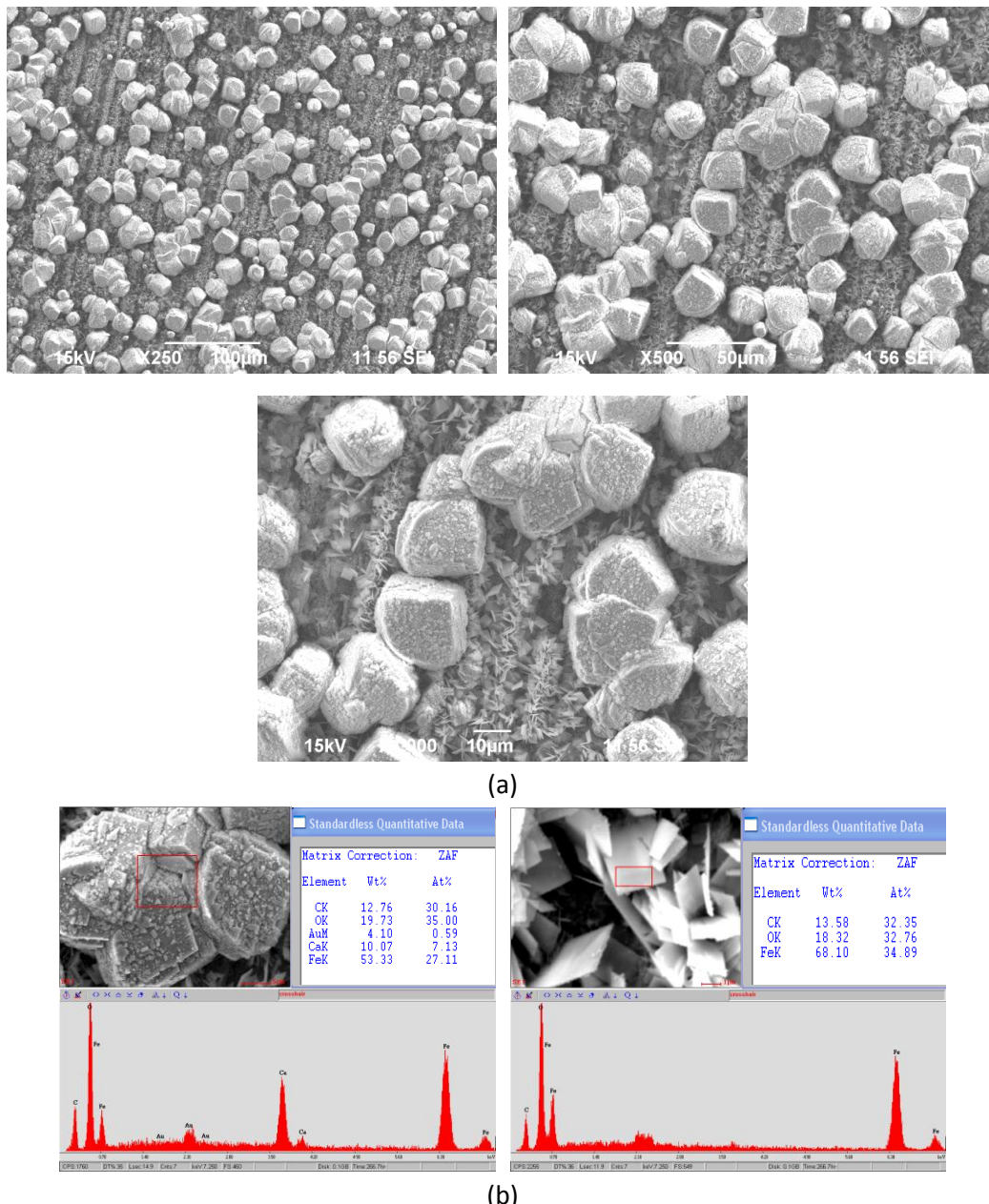


Figure 37. SEM images and EDS spectra taken on carbon steel specimen (CS1018) surface of the bulk solution with 10 ppm  $\text{Fe}^{2+}$  and 100 ppm  $\text{Ca}^{2+}$  at 80 °C and  $\text{pCO}_2$  0.5 bar after the 1<sup>st</sup> drop in the pH.

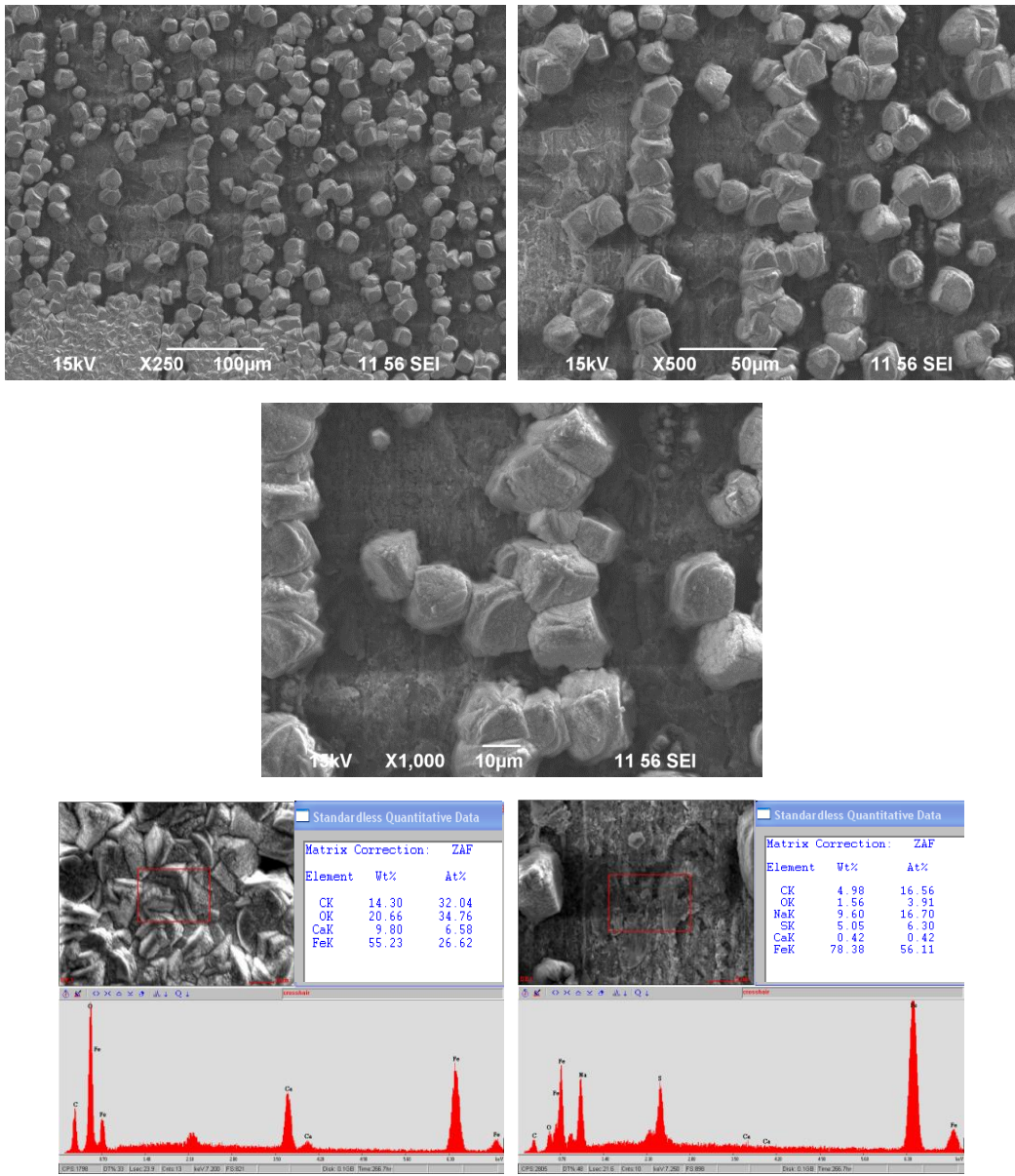


Figure 38. SEM images and EDS spectra taken on carbon steel specimen (CS1018) surface of the bulk solution with 10 ppm  $\text{Fe}^{2+}$  and 100 ppm  $\text{Ca}^{2+}$  at 80 °C and  $\text{pCO}_2$  0.5 bar after the 2<sup>nd</sup> drop in the pH.

Figure 39 shows the cross sectional analysis of the sample recovered from the electrolyte with 100 ppm  $\text{Ca}^{2+}$  at the conclusion of the experiment. As was expected and

shown in Figure 38 that the surface was covered by  $\text{FeCO}_3$  and  $\text{Fe}_x\text{Ca}_y\text{CO}_3$  ( $x+y=1$ ) layers.

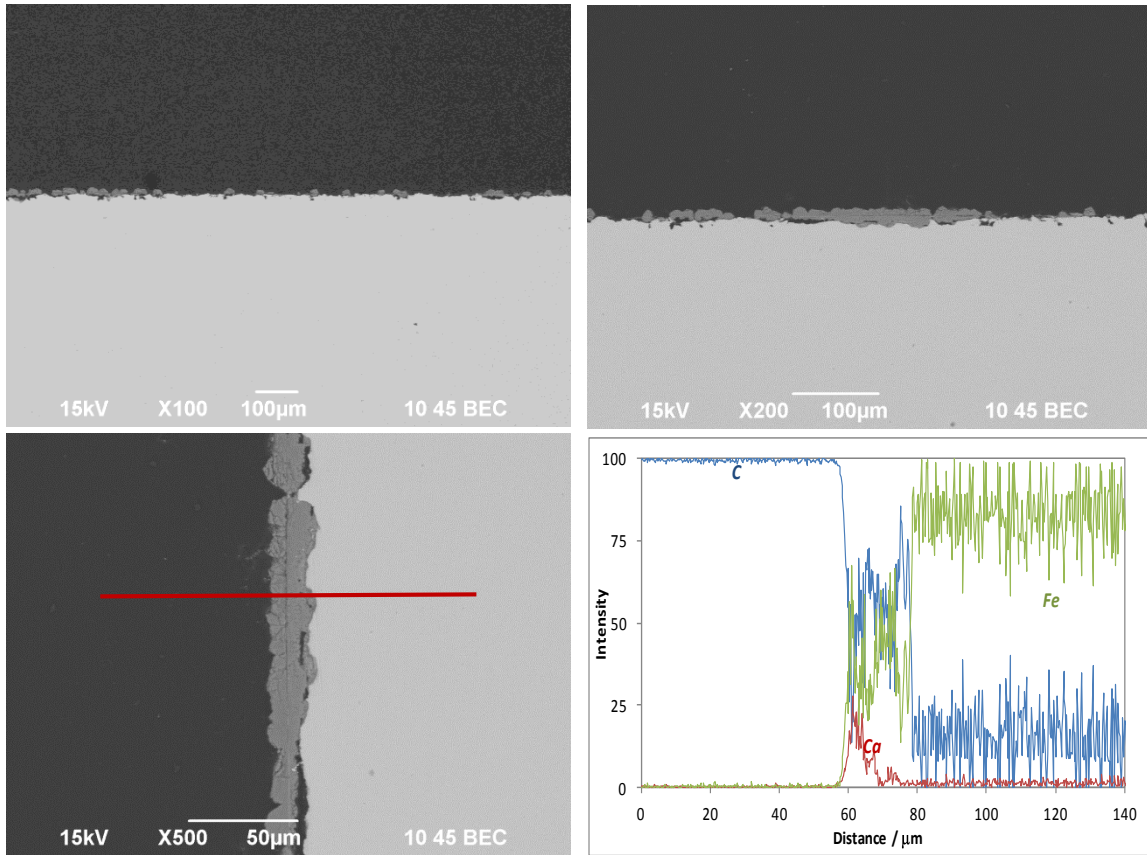


Figure 39. Cross section image and EDS spectra taken on carbon steel specimen (CS1018) of the bulk solution with 10 ppm  $\text{Fe}^{2+}$  and 100 ppm  $\text{Ca}^{2+}$  at 80 °C and  $\text{pCO}_2$  0.5.

Figure 40 shows sample surface after specimens were treated with Clarke solution [41]. According to Figure 23 the corrosion rate increased due to the change in pH. Similarly to the experiment with 10 ppm  $\text{Ca}^{2+}$ , the pH drop did not lead to pitting attack and caused only a higher general corrosion rate.

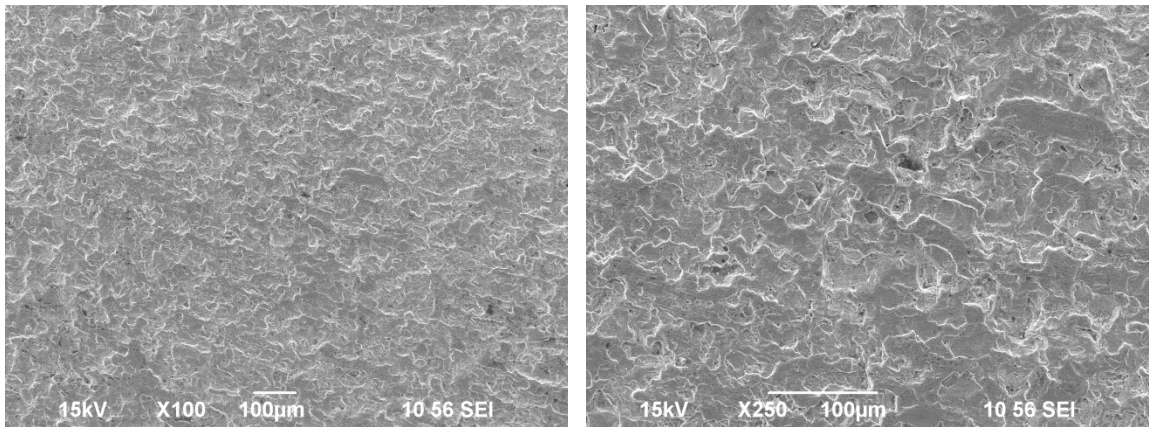


Figure 40. Surfaces after corrosion product removal of the carbon steel specimen (CS1018) surface of the bulk solution with 10 ppm  $\text{Fe}^{2+}$  and 100 ppm  $\text{Ca}^{2+}$  at 80 °C and  $\text{pCO}_2$  0.5 bar.

#### **Chloride or calcium; which one is to be blamed for localized attack**

At 10,000 ppm  $\text{Ca}^{2+}$ , the corrosion behavior was non-uniform as shown in Figure 20 (e). As mentioned earlier in the experiment procedure, the desired  $\text{Ca}^{2+}$  concentrations were added to the cell by addition of  $\text{CaCl}_2$ . In order to have 10,000 ppm  $\text{Ca}^{2+}$  in the bulk solution, 54.7 g  $\text{CaCl}_2$  was added into the cell (2 litres of electrolyte). This means that in addition to 10,000 ppm  $\text{Ca}^{2+}$ , 17,800 ppm  $\text{Cl}^-$  was added to the bulk. This can raise a concern that such a high  $[\text{Cl}^-]$  had an effect on the non-uniform corrosion behavior.

The next experimental set up was to investigate the effect of chlorides on the non-uniform behavior of the corrosion in the experiment with “10,000 ppm  $\text{Ca}^{2+}$  (54.7 g  $\text{CaCl}_2$ )”.

A 3 wt.%  $\text{NaCl}$  solution, for 2 litres of electrolyte, has the equivalent  $\text{Cl}^-$  concentration as 54.7 g  $\text{CaCl}_2$  (17,800 ppm). The initial pH for the experiment with 4 wt.%  $\text{NaCl}$  solution was set to pH 5.5, because as soon as 54.7 g  $\text{CaCl}_2$  was added to the

glass cell for the experiment with 10,000 ppm  $\text{Ca}^{2+}$  the pH dropped to pH 5.5 immediately due to the bulk precipitation of  $\text{CaCO}_3$ .

The solution, initially supersaturated with respect to  $\text{CaCO}_3$ , had high tendency for precipitation of  $\text{CaCO}_3$  which leads to a drop of the pH. This decreases the alkalinity of the solution and, affects the equilibria relating to the dissociation reactions. Figure 41 shows the corrosion behavior of the experiments conditions with 10,000 ppm  $\text{Ca}^{2+}$  and 0 ppm  $\text{Ca}^{2+}$ , in a pure NaCl electrolyte, having equal  $\text{Cl}^-$  concentrations. Even though the corrosion behavior during the experiments was different, after 6 days they both finished with the same corrosion rate. For the experiment with 10,000 ppm  $\text{Ca}^{2+}$ , the immediate formation of  $\text{CaCO}_3$  on the steel surface provided a diffusion barrier which limited corrosion. Although it was not a protective layer, it retarded the transportation of the corrosive species toward the surface. In the 4 wt.% NaCl solution, the corrosion rate started to decrease as soon as the solution became supersaturated with respect to  $\text{FeCO}_3$ . The formation of  $\text{FeCO}_3$  decreased the rate of corrosion as it also retarded the transportation of the corrosive species toward the surface. However, the formation of  $\text{FeCO}_3$  could not keep up with the corrosion rate. So, no protective layer could be formed, explaining the high general corrosion rate [11].

Figure 42 shows the corrosion potential behavior of the tested samples. The potential behavior appeared to be similar. As shown in Figure 41 for the experiment with 4% NaCl, the corrosion rate increased in the first day. By the potential plot it can be inferred that the corrosion rate was governed by the dissolution of the steel. After the

first day the cathodic reaction became retarded by the formation of a semi-protective layer on the surface since the potential kept increasing.

For the experiment with 10,000 ppm  $\text{Ca}^{2+}$ , based on the corrosion behavior and potential plot in Figure 41 and Figure 42, the corrosion behavior was governed by the cathodic reaction from the beginning. This also implies that the transportation of  $\text{H}^+$  toward the steel surface was retarded by formation of a semi-protective layer on the surface.

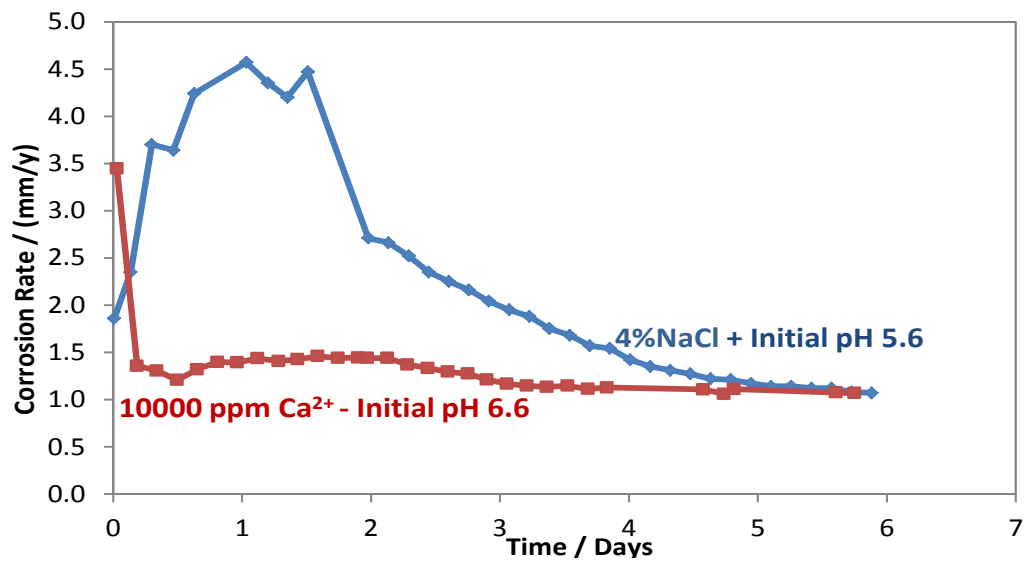


Figure 41. Variations of corrosion rate versus time of carbon steel specimen (CS1018) for two experiments with different initial concentrations of  $\text{Ca}^{2+}$  (0 and 10,000 ppm) and the same  $[\text{Cl}^-]$ .

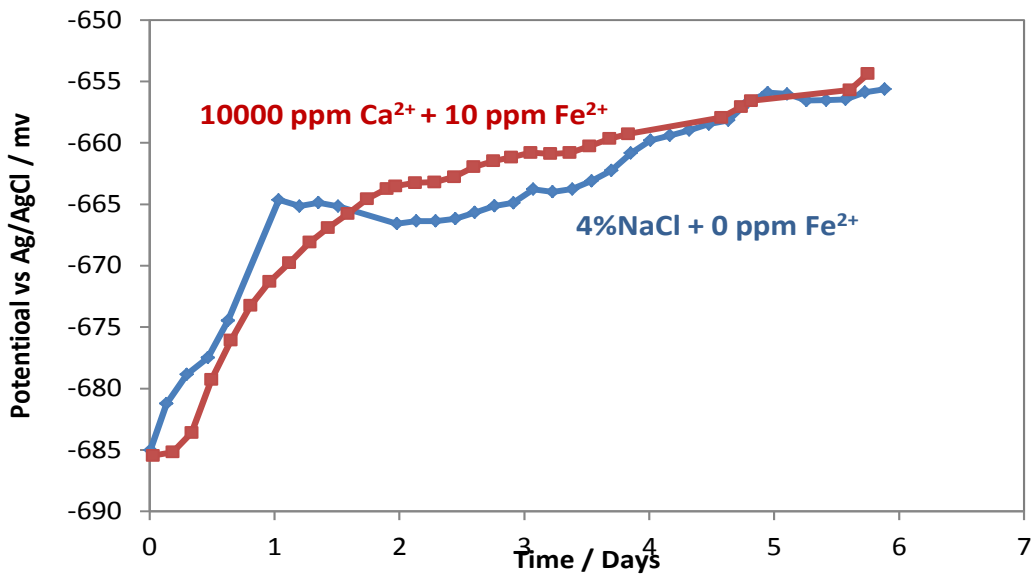


Figure 42. Variations of open circuit potential versus time of carbon steel specimen (CS1018) for two experiments with different initial concentrations of  $\text{Ca}^{2+}$  (0 and 10,000 ppm) and the same  $[\text{Cl}^-]$ .

Figure 43 corresponds to the pH behavior as a function of time for the tested conditions. In the experiment with 4 wt.% NaCl, the pH stabilized around 6.0 while for the solution with 10,000 ppm  $\text{Ca}^{2+}$  it stabilized at around 5.5. In the system where the formation of  $\text{FeCO}_3$  is the dominant reaction, pH stabilizes around 6.0 at which point the system reaches equilibrium. On the other hand, in the system where the formation of  $\text{CaCO}_3$  is the dominant reaction, the pH stabilization is around 5.5 for the same reason. Since the goal of this set up was to keep all the conditions but the  $\text{Ca}^{2+}$  concentration as close as possible, in the experiment with 4 wt.% NaCl it was attempted to keep the pH at around 5.5 by the addition of deoxygenated HCl. However, once adjusted the pH did not stay at this value and increased to 6.0, as explained earlier, because the equilibrium reactions drove system towards the increased the pH to reach the thermodynamic equilibrium value.

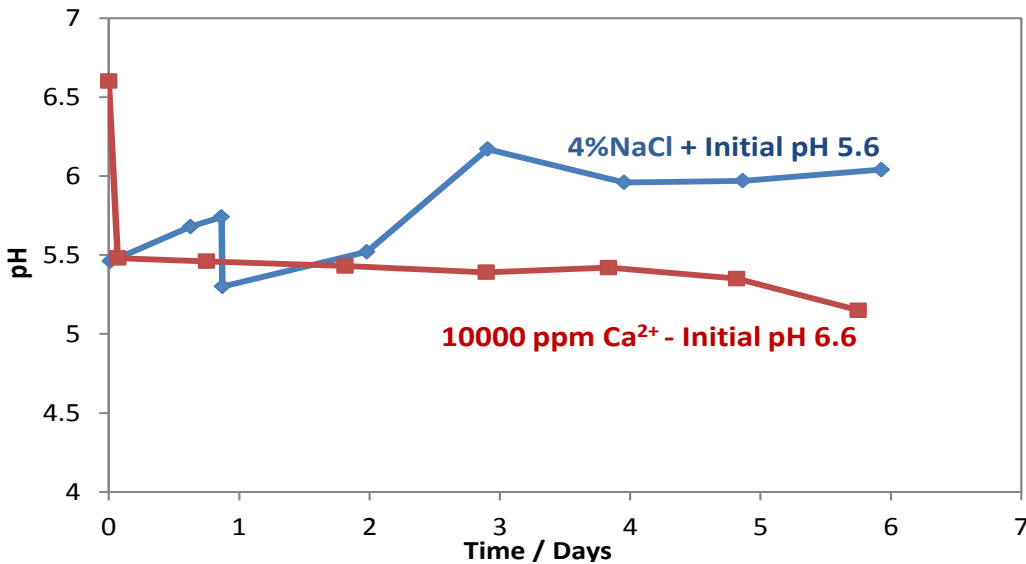


Figure 43. Variations of pH of the system for two experiments with different initial concentrations of  $\text{Ca}^{2+}$  (0 and 10,000 ppm) and the same  $[\text{Cl}^-]$ .

Figure 44 and Figure 45 shows the  $\text{Fe}^{2+}$  concentrations and the degree of  $\text{FeCO}_3$  saturation over time, respectively.

The solution with 10,000 ppm  $\text{Ca}^{2+}$  was under-saturated with respect to  $\text{FeCO}_3$  for the whole duration of the experiment, whereas the 4 wt.% NaCl solution reached the saturation degree of 1 after 2 days and remained supersaturated for the rest of the experiment. The high corrosion rate provided enough  $\text{Fe}^{2+}$  for the solution to stay supersaturated.

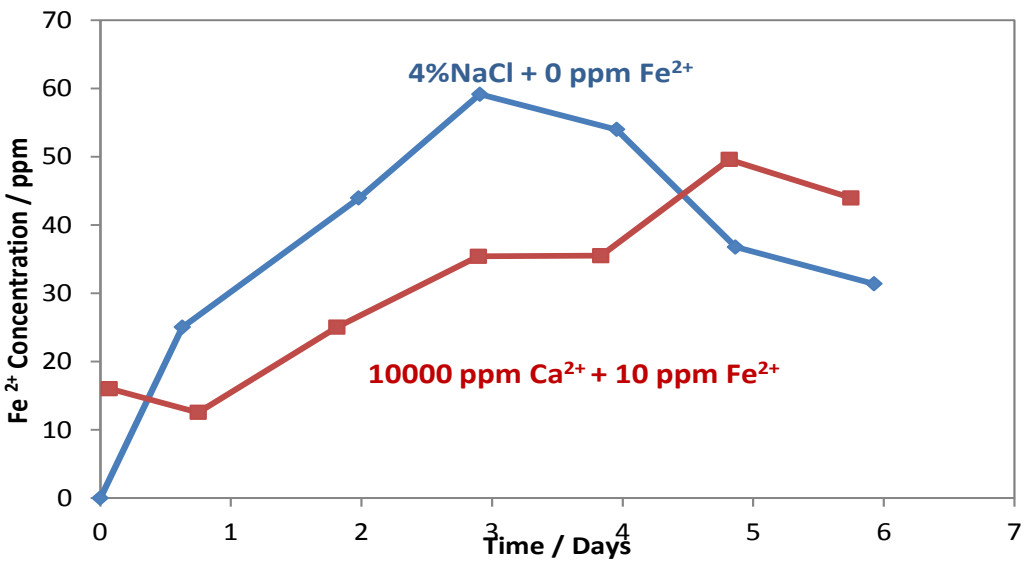


Figure 44. Variations of Fe<sup>2+</sup> concentration of the system for two experiments with different initial concentrations of Ca<sup>2+</sup> (0 and 10,000 ppm) and the same [Cl].

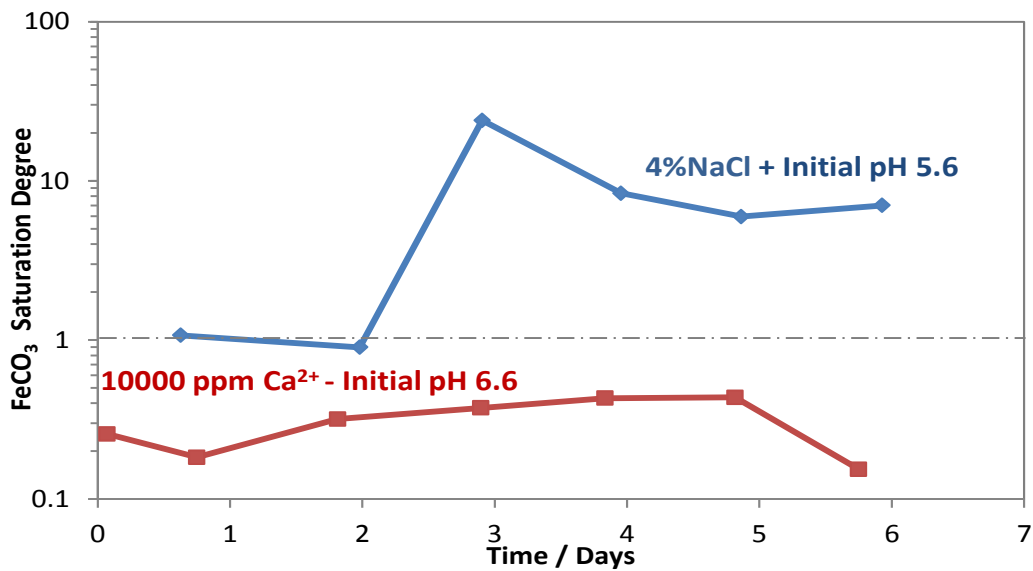


Figure 45. Variations of FeCO<sub>3</sub> saturation degree of the system for two experiments with different initial concentrations of Ca<sup>2+</sup> (0 and 10,000 ppm) and the same [Cl].

Figure 46 and Figure 47 shows the SEM images and EDS spectra of the samples. Figure 46 (a) represents the recovered sample from the solution with 4 wt.% NaCl. The surface was partially covered with relatively large, prismatic FeCO<sub>3</sub> crystals. According to Figure 46 (a) it seemed even the visually crystal free places had some degree of FeCO<sub>3</sub> surface coverage. However, this was not sufficiently protective based on the observed high general corrosion rate, as was shown in Figure 41 for this condition.

Figure 46 (b) represents the SEM images of the sample of the experiment with 10,000ppm Ca<sup>2+</sup>. As was discussed previously, the morphology of the layer is dramatically different. Figure 46 (b) shows the surface is covered with a non-protective layer which is dominated by Fe<sub>x</sub>Ca<sub>y</sub>CO<sub>3</sub> ( $x+y=1$ ); from EDS data the crystals would have the formula Fe<sub>0.09</sub>Ca<sub>0.91</sub>CO<sub>3</sub>.

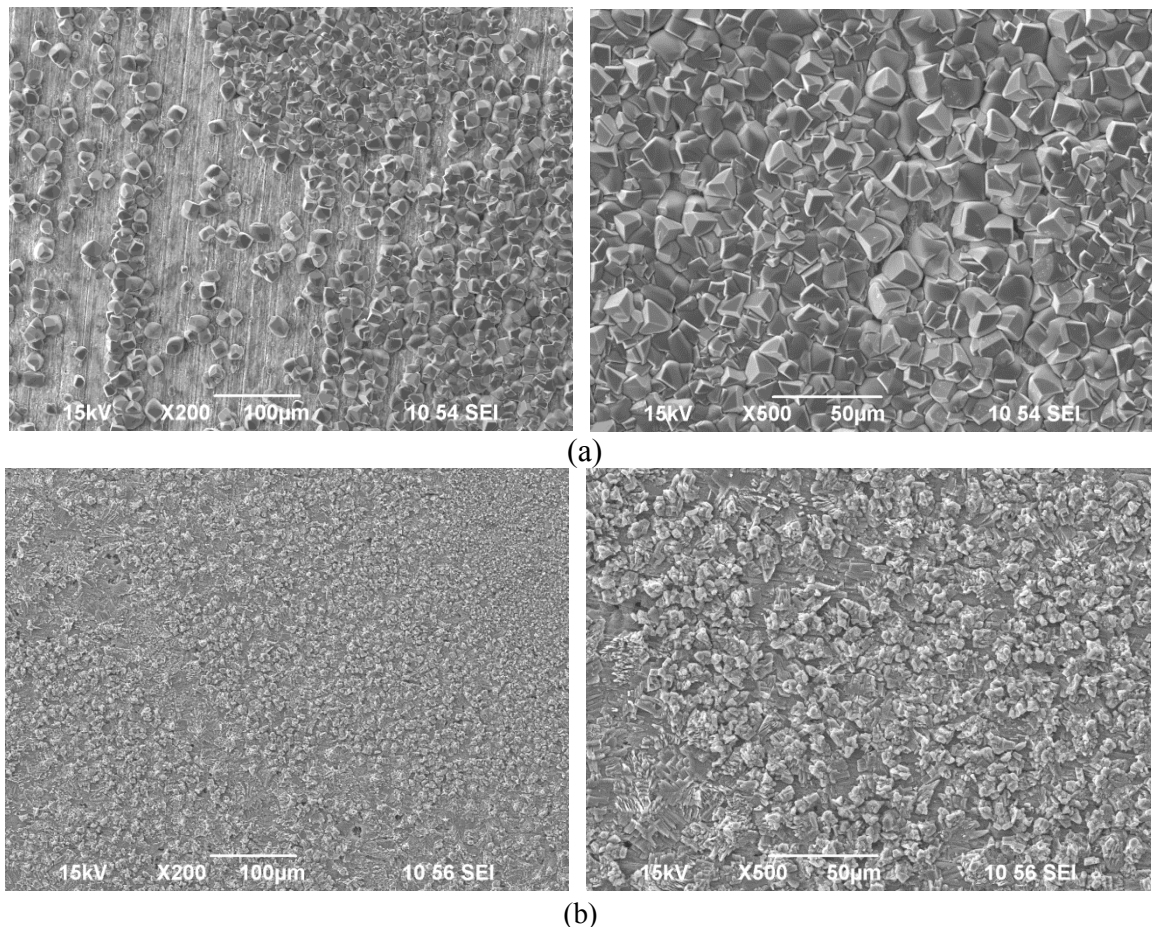


Figure 46. SEM images taken on carbon steel specimen (CS1018) surface of the bulk solution with (a) 4wt% NaCl (b) 10 ppm  $\text{Fe}^{2+}$  and 10,000 ppm  $\text{Ca}^{2+}$  at 80 °C and  $\text{pCO}_2$  0.5 bar after 6 days.

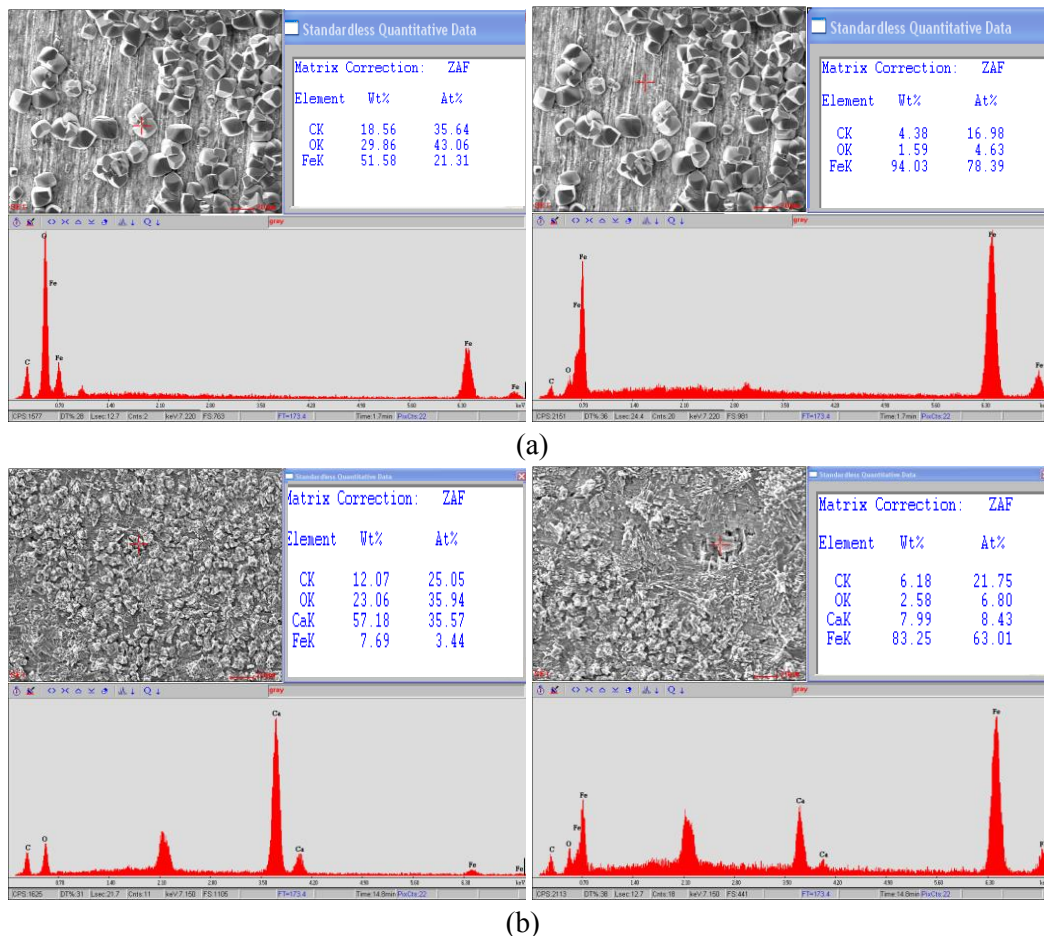


Figure 47. EDS spectra taken on carbon steel specimen (CS1018) surface of the bulk solution with (a) 4wt% NaCl (b) 10 ppm  $\text{Fe}^{2+}$  and 10,000 ppm  $\text{Ca}^{2+}$  at 80 °C and  $\text{pCO}_2$  0.5 bar after 6 days.

Figure 48 shows the cross-sectional analysis of the samples from the tested conditions. The sample from the bulk solution with 4 wt.% NaCl, Figure 48 (a), was covered with a thick layer of  $\text{FeCO}_3$ , whereas the surface of the specimen from the high  $\text{Ca}^{2+}$  experiment, see Figure 48 (b), was covered with a thin layer. The comparison of cross-section images reveals a non-uniform behavior of the corrosion in the presence of  $\text{Ca}^{2+}$ .

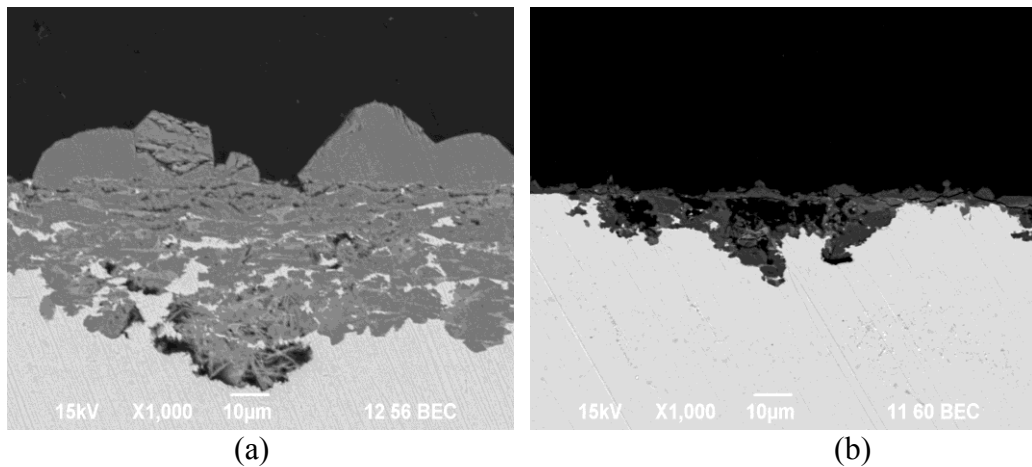


Figure 48. Cross section image taken on carbon steel specimen (CS1018) of the bulk solution with (a) 4wt% NaCl (b) 10 ppm  $\text{Fe}^{2+}$  and 10,000 ppm  $\text{Ca}^{2+}$  at 80  $^{\circ}\text{C}$  and  $\text{pCO}_2$  0.5 bar after 6 days.

Figure 49 corresponds to SEM images of the specimen surfaces after treatment with Clarke solution [41]. There was no localized attack in the 4 wt.% NaCl solution, Figure 49 (a), while the sample from the 10,000 ppm  $\text{Ca}^{2+}$  solution, Figure 49 (b), suffered from localized attack.

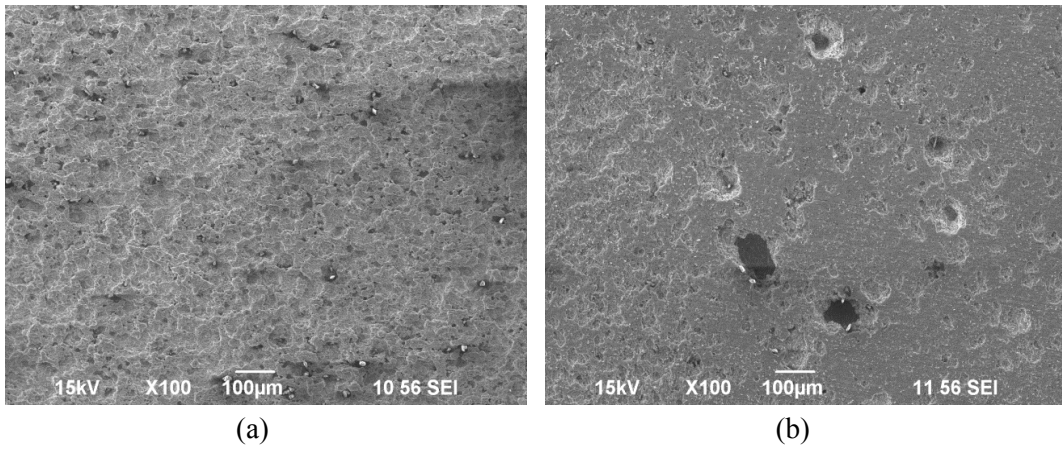


Figure 49. Surfaces after corrosion product removal of the carbon steel specimen (CS1018) surface of the bulk solution with (a) 4wt% NaCl (b) 10 ppm  $\text{Fe}^{2+}$  and 10,000 ppm  $\text{Ca}^{2+}$  at 80°C and  $\text{pCO}_2$  0.5 bar.

As mentioned in the literature review chapter, Jiang et al., Ren et al. and Zhu et al. reported the negative effect of  $\text{Cl}^-$  on the non-uniform corrosion behavior in their studies. They believed it was  $\text{Cl}^-$  which caused the non-uniform attack and not  $\text{Ca}^{2+}$  [34], [36], [38]. From the above findings, it is concluded that the non-uniform corrosion behavior is due to the presence of  $\text{Ca}^{2+}$  on the formation of the  $\text{FeCO}_3$  layer. The addition of 17,800 ppm  $[\text{Cl}^-]$ , as such, is not believed to have caused the non-uniform corrosion behavior.

Calcium at the higher concentrations of 1,000 and 10,000 ppm altered the corrosion behavior and caused a non-uniform corrosion behavior at the 10,000 ppm concentration. So far, the effect of  $\text{Ca}^{2+}$  was studied at an initial pH of 6.6. At this pH, the solution is highly supersaturated with respect to  $\text{CaCO}_3$ . As a result, the rapid formation of  $\text{CaCO}_3$  in the first hours of experiment, and consequently the prompt change in the water chemistry, may play a major role in the different corrosion behavior. Thus, the next

experimental set up was set to lower the initial pH to study its effect at 10,000ppm  $\text{Ca}^{2+}$  on the corrosion behavior.

### **Effect of initial pH at 10,000 ppm $\text{Ca}^{2+}$ on corrosion behavior**

It was discussed in the previous sections that the higher  $\text{Ca}^{2+}$  concentrations (1,000 and 10,000 ppm) changed the corrosion behavior as well as the morphology of the crystals that grew on the steel surface. The  $\text{CaCO}_3$  saturation degree of a  $\text{CO}_2$  saturated solution with 10,000ppm  $\text{Ca}^{2+}$  at 80°C and a pH of 6.6 is around 10,000. Thus, the solution is highly supersaturated with respect to  $\text{CaCO}_3$ . A second experiment was carried out with the initial pH set to 5.3, such that the saturation degree of  $\text{CaCO}_3$  is about 10; *i.e.*, a considerably lower degree of super-saturation. No  $\text{Fe}^{2+}$  was added into the cell.

Figure 50 represents the corrosion potential of the two experiments. For the experiment with higher initial pH, the potential increased with time. This is assumed to be a result of the formation of a mass transfer limiting layer on the surface which retarded the dissolution of the iron. However, this barrier layer was not particularly protective, according to the final corrosion rate shown in Figure 51 corresponds to the corrosion behavior of the tested conditions with 10,000ppm  $\text{Ca}^{2+}$  with initial pH values of 6.6 and pH 5.3. Despite the different initial corrosion behavior of the two tested conditions, they reached the same corrosion rate at the end of the experiments. The immediate drop of corrosion rate at higher initial pH was due to an instant formation of  $\text{CaCO}_3$  on the surface of the tested specimen. For the experiment with initial pH 5.3, the surface nucleation and crystal growth processes that govern the formation of  $\text{CaCO}_3$  were not as

rapid as for the experiment with the initial pH of 6.6, therefore it took longer for the corrosion rate to drop.

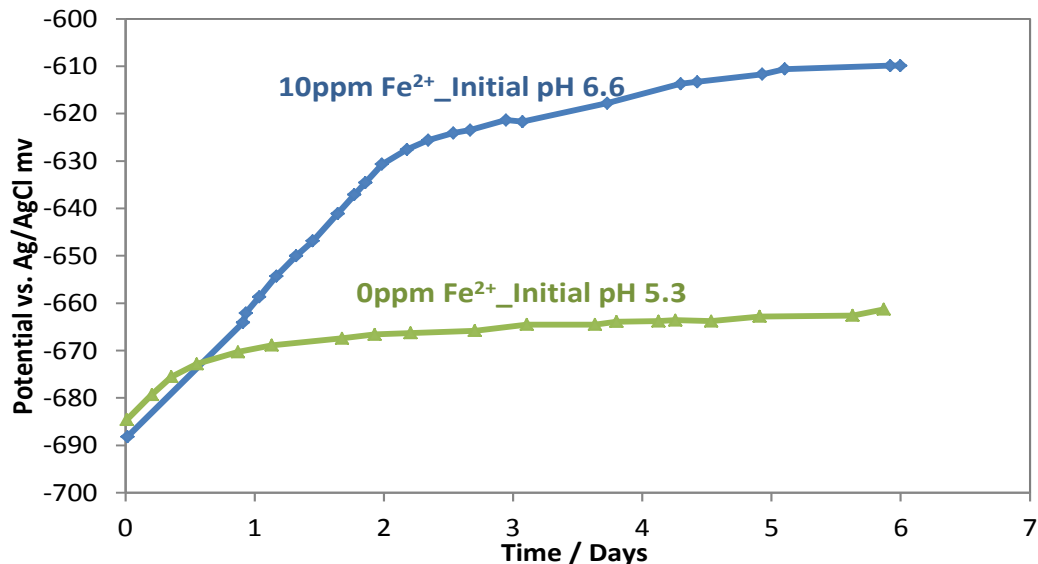


Figure 50. Variations of open circuit potential of carbon steel specimen (CS1018) for the experiments with 10,000 ppm  $\text{Ca}^{2+}$  at different initial pH (pH 6.6 or pH 5.3).

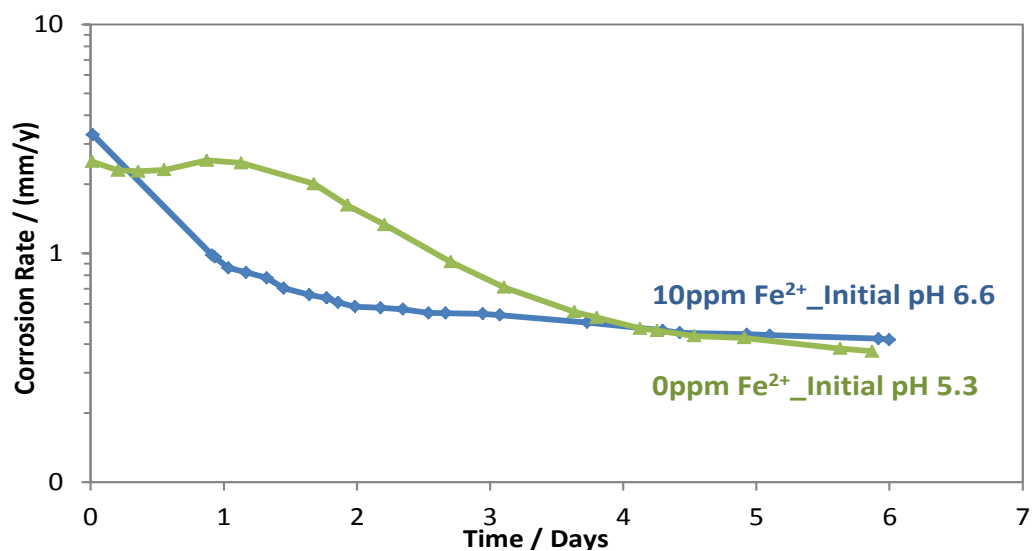


Figure 51. Corrosion rate versus time of carbon steel specimen (CS1018) for the experiments with 10,000 ppm  $\text{Ca}^{2+}$  at different initial pH (pH 6.6 or pH 5.3).

Figure 52 shows the variation of pH over time for the tested conditions. After the initial drop in pH for the system with the initial pH of 6.6, relatively stable pH values were achieved for both conditions after the first few hours. It is noteworthy that for the experiment with the lower initial pH unit the acidity slightly decreased over the first 96 hours, whereas for the higher initial pH condition the acidity continued to increase.

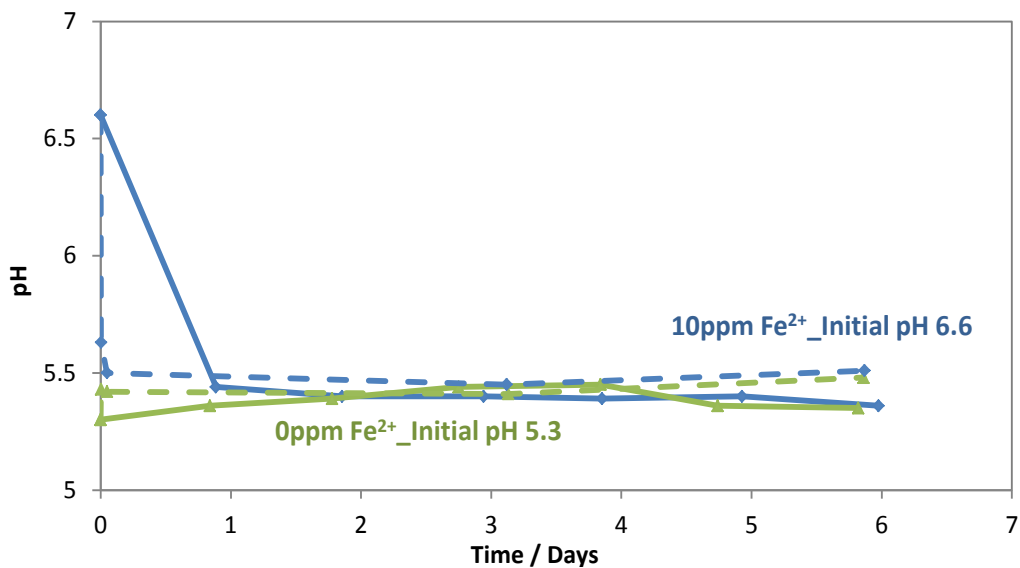


Figure 52. Variations of pH of the system for the experiments with 10,000 ppm Ca<sup>2+</sup> at different initial pH (pH 6.6 or pH 5.3).

Figure 53 and Figure 54 represent the concentration of Fe<sup>2+</sup> and degree of FeCO<sub>3</sub> saturation over time, respectively. The plot for Fe<sup>2+</sup> concentration versus time implies that the heterogeneous precipitation of Fe<sup>2+</sup> as either FeCO<sub>3</sub> or Fe<sub>x</sub>Ca<sub>y</sub>CO<sub>3</sub> ( $x+y=1$ ) was insufficiently fast to rapidly develop a protective corrosion product layer; this was the case for both experiments.

Figure 54 shows, for both conditions, the solutions were under-saturated with respect to  $\text{FeCO}_3$  for the entire duration of the experiments.

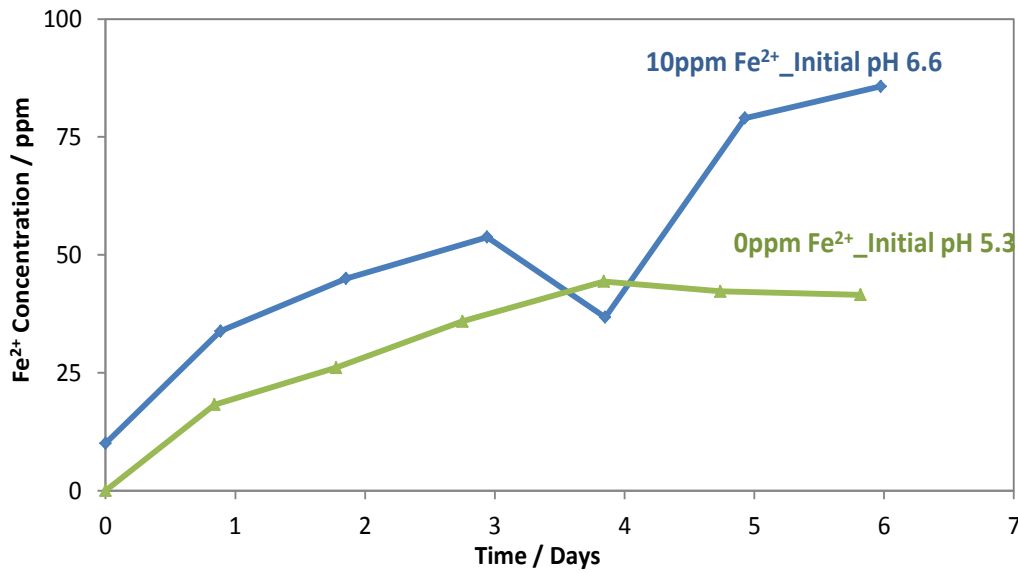


Figure 53. Variations of  $\text{Fe}^{2+}$  concentration of the system for the experiments with 10,000 ppm  $\text{Ca}^{2+}$  at different initial pH (pH 6.6 or pH 5.3).

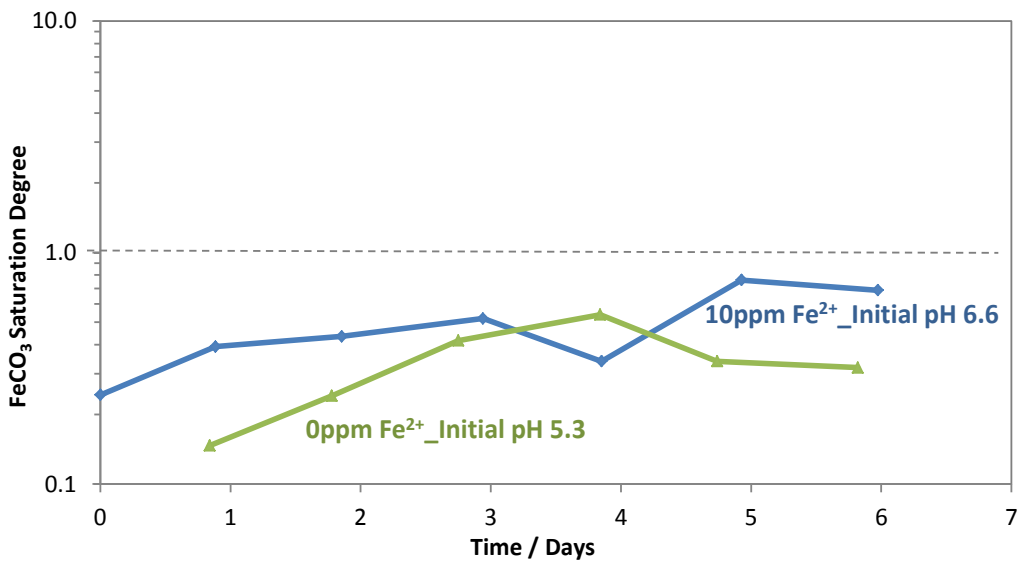


Figure 54. Variations of degree of  $\text{FeCO}_3$  saturation of the system for the experiments with 10,000 ppm  $\text{Ca}^{2+}$  at different initial pH (pH 6.6 or pH 5.3).

Figure 55 shows the variation of  $\text{Ca}^{2+}$  concentration as a function of time for two experiments with initial 10,000 ppm  $\text{Ca}^{2+}$  concentrations at different initial pH values. The presented data for  $\text{Ca}^{2+}$  concentration correspond to repeated experiments of those performed for identical conditions; 10,000 ppm  $\text{Ca}^{2+}$  at initial pH values of 5.3 and 6.6. An ICP spectrometer was used to measure the  $\text{Ca}^{2+}$  concentration. The variation of pH for both experiments, plotted in Figure 52, was discussed above. Figure 56 shows that the experiment with the higher initial pH was highly supersaturated ( $\sim 9,000$ ) with respect to  $\text{CaCO}_3$ . Thus, an abrupt homogeneous precipitation of  $\text{CaCO}_3$ , with an accompanying drop in pH, pushed the system towards thermodynamic equilibrium. This process corresponds to the chemical reaction (28).

For the experiment with the lower initial pH value, the saturation degree of the solution with respect to  $\text{CaCO}_3$  was stable during the 6 days of the experiment. The abrupt precipitation of  $\text{CaCO}_3$  resulted in the decrease in the  $\text{Ca}^{2+}$  concentration only for the experiment with the higher initial pH value.

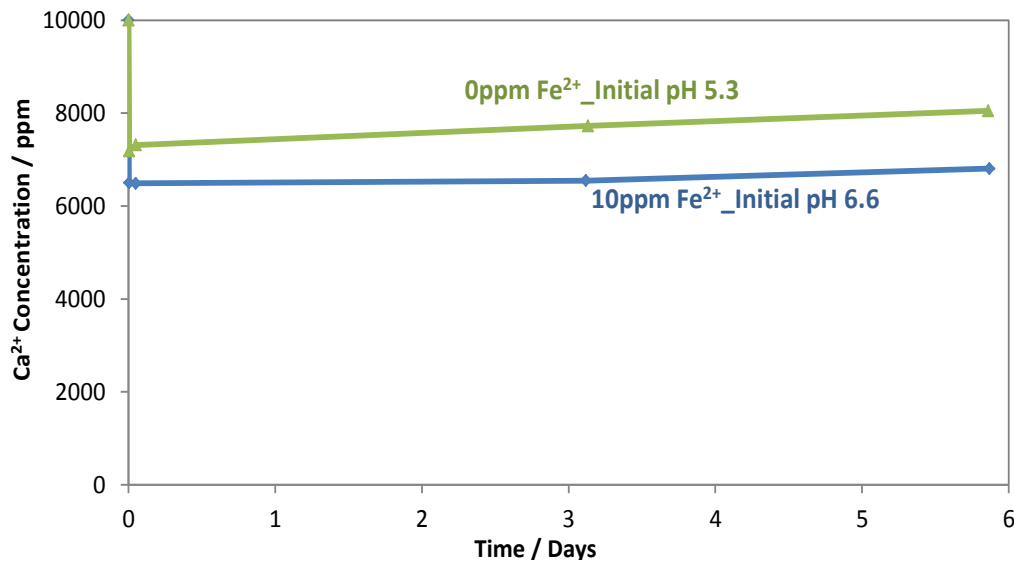


Figure 55. Variations of  $\text{Ca}^{2+}$  concentration of the system for the experiments with 10,000 ppm  $\text{Ca}^{2+}$  at different initial pH (pH 6.6 or pH 5.3).

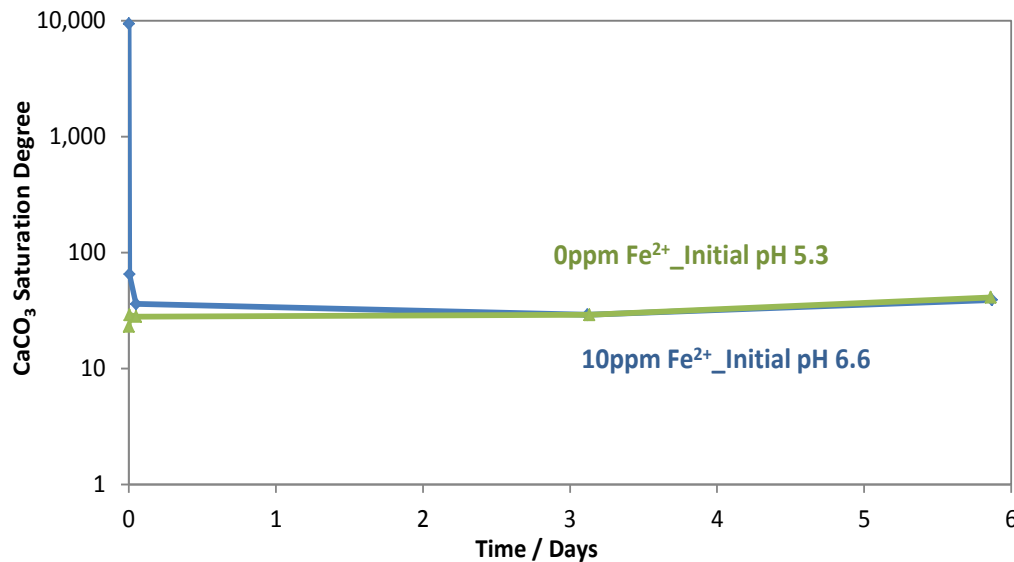


Figure 56. Variations of degree of  $\text{CaCO}_3$  saturation of the system for the experiments with 10,000 ppm  $\text{Ca}^{2+}$  at different initial pH (pH 6.6 or pH 5.3).

Figure 57 and Figure 58 show the SEM images and EDS spectra of the recovered sample from the solution with 10,000ppm  $\text{Ca}^{2+}$  at pH 5.3. As shown, the morphology of the formed layer has local variations.

Figure 58 shows the EDS spectra of the sample. Regions of the surface that still exhibit polishing marks seem to be covered by a thin layer with a chemistry consistent with a calcium-substituted siderite solid solution. The crystals have a composition consistent with being an iron-substituted calcite.

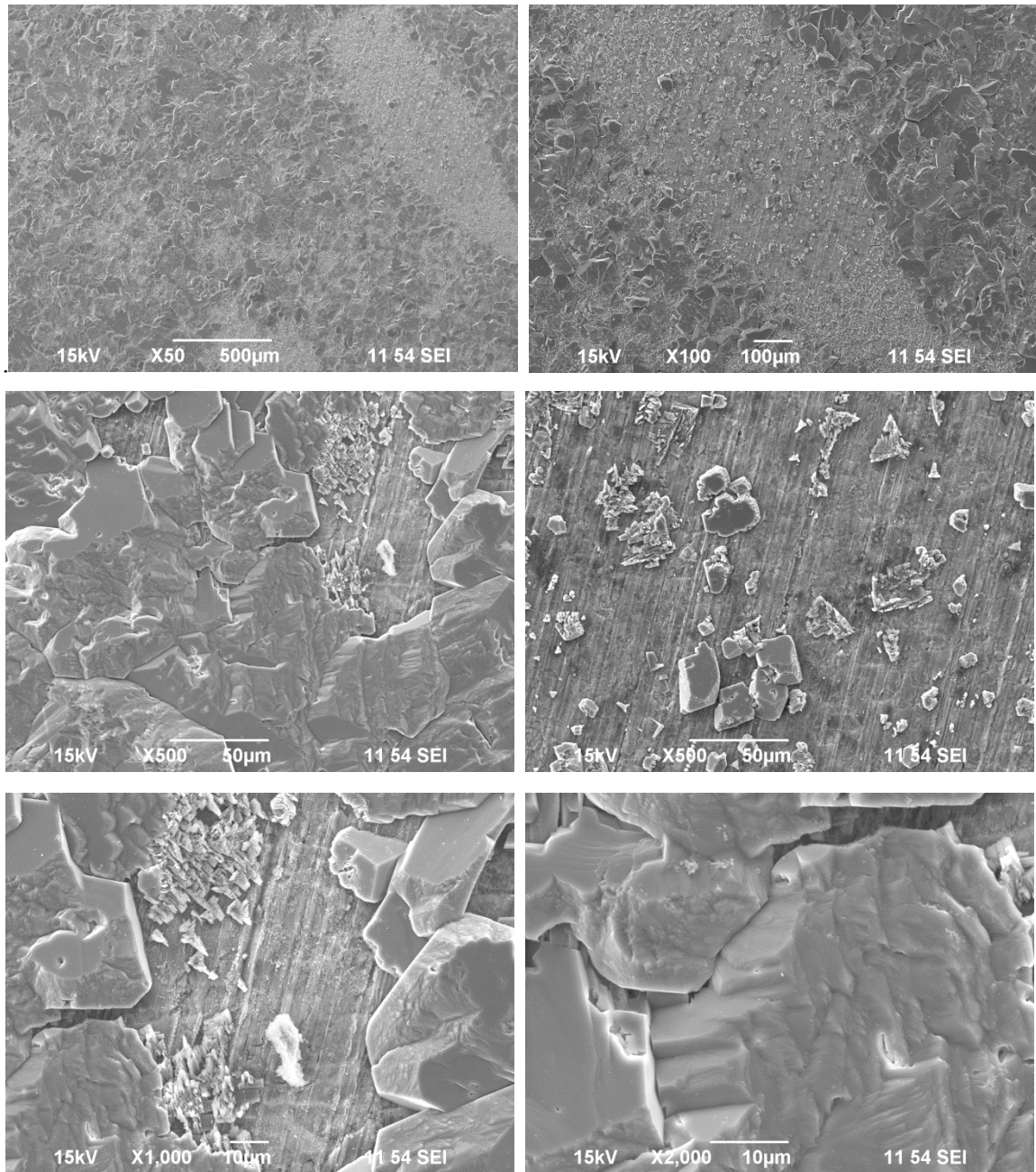


Figure 57. SEM images taken on carbon steel specimen (CS1018) surface of the bulk solution with 10,000 ppm  $\text{Ca}^{2+}$  and initial pH 5.3 at 80°C and  $\text{pCO}_2$  0.5.

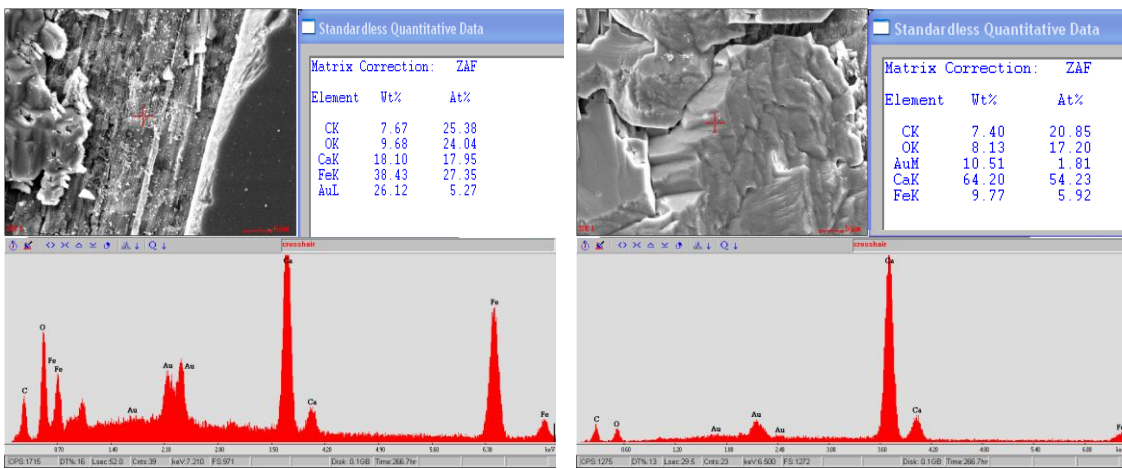


Figure 58. EDS spectra taken on carbon steel specimen (CS1018) surface of the bulk solution with 10,000 ppm  $\text{Ca}^{2+}$  and initial pH 5.3 at 80°C and  $\text{pCO}_2$  0.5.

Figure 59 is a comparison of the SEM images for the recovered specimens from the bulk solutions with 10,000 ppm  $\text{Ca}^{2+}$  with initial pH values of (a) 6.6 and (b) 5.3. As is shown, they had a very different surface morphology. The sample from the solution with lower initial pH was covered with different crystal morphologies in particular areas. Unlike  $\text{FeCO}_3$ ,  $\text{CaCO}_3$  can form with many different crystal structures. Regardless of the different morphology, EDS spectra in Figure 60 showed data consistent with the formation of substitutional solid solutions in both conditions.

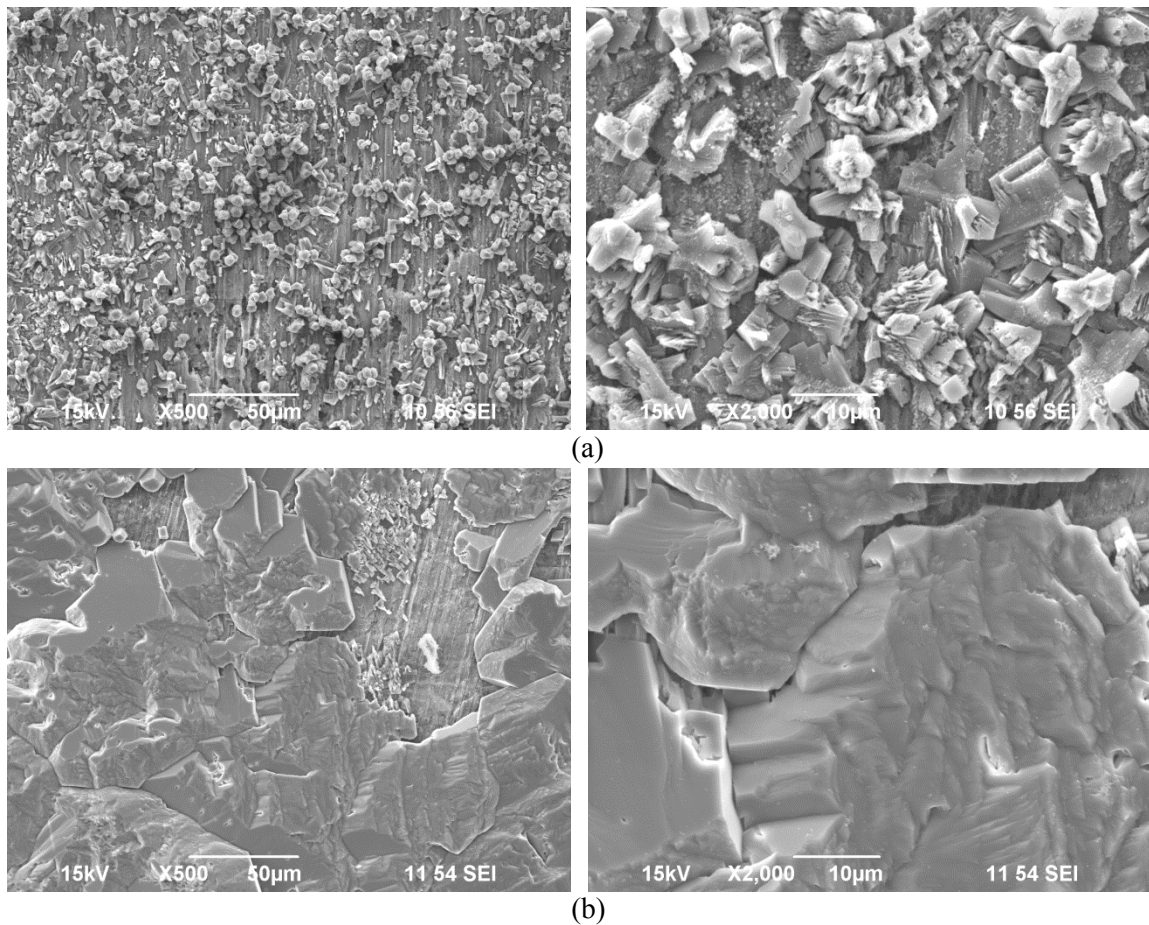


Figure 59. SEM images taken on carbon steel specimen (CS1018) surface of the bulk solution with 10,000 ppm  $\text{Ca}^{2+}$  at 80°C and  $\text{pCO}_2$  0.5 bar (a) initial pH 6.6 (b) initial pH 5.3.

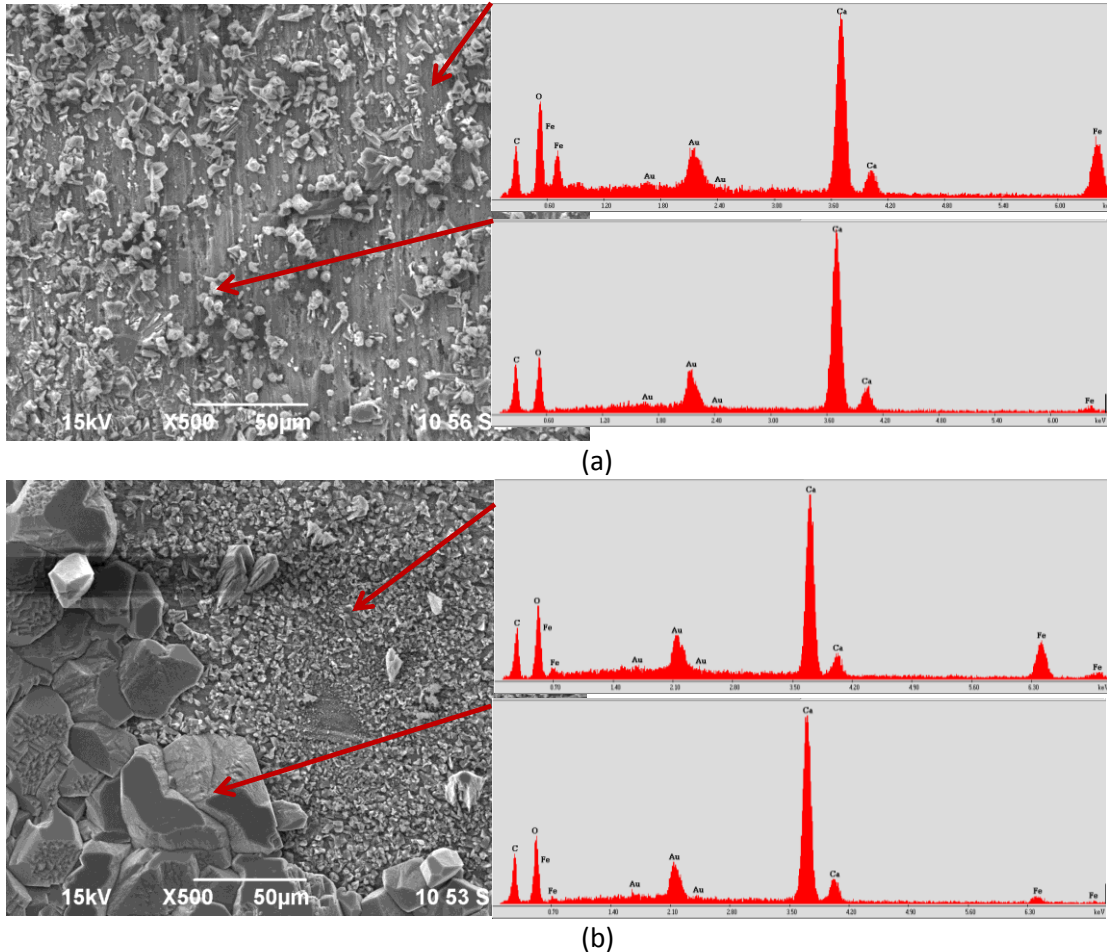


Figure 60. EDS spectra taken on carbon steel specimen (CS1018) surface of the bulk solution at 80°C and pCO<sub>2</sub> 0.5 bar with 10,000 ppm Ca<sup>2+</sup> (a) pH 6.6 (b) and pH 5.3.

Figure 61 shows the cross-section data for both conducted experiments. Non-uniform corrosion attack was found for both conditions. The line scanning EDS in Figure 61 (a) showed a different concentration of Ca<sup>2+</sup> in the layer filling the pit. Figure 61 (b) shows a gradient of Ca<sup>2+</sup> with the higher concentration on top of the steel surface and a lower concentration adjacent to the surface, while the gradient with respect to Fe<sup>2+</sup> was *vice versa*.

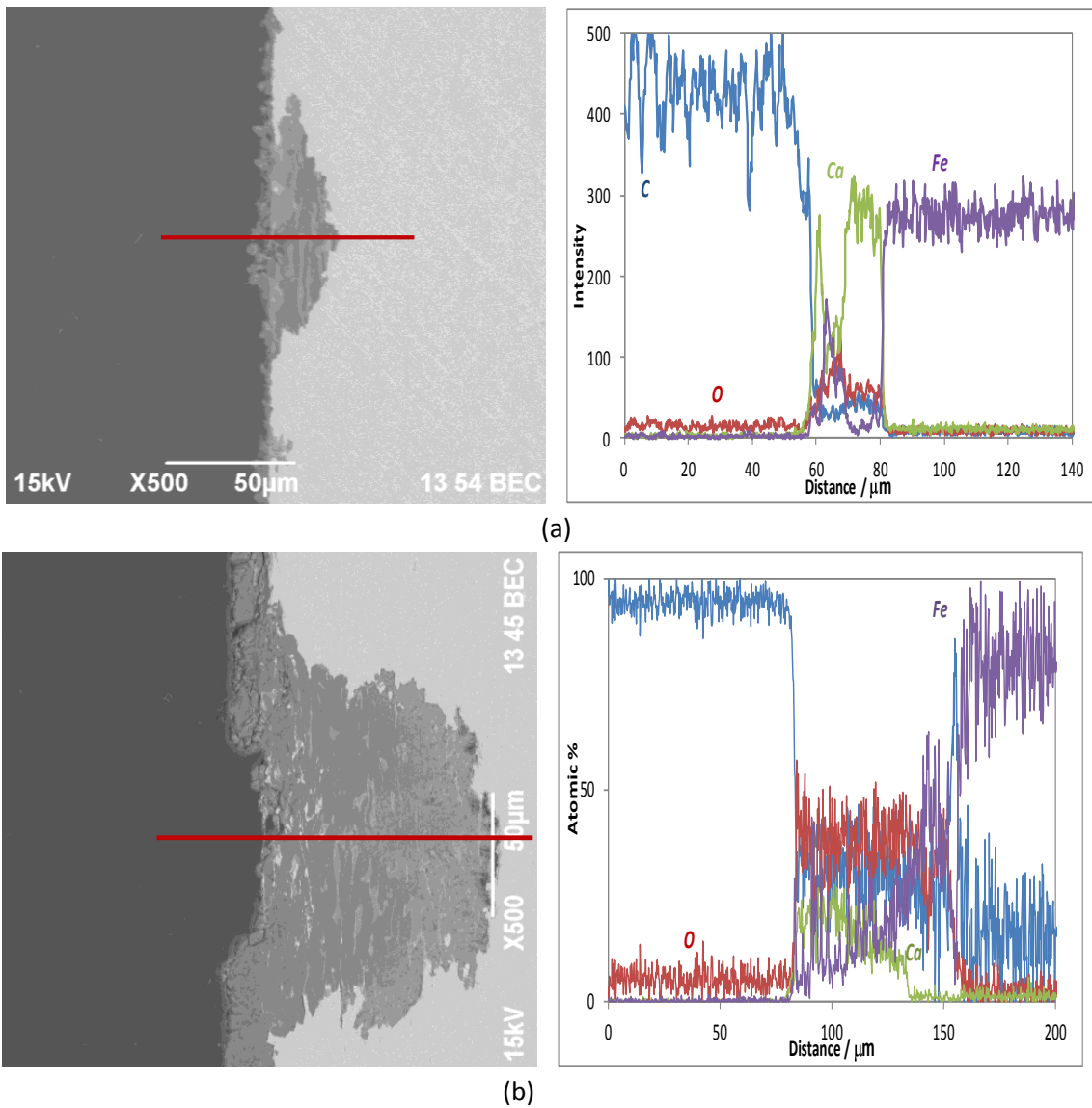


Figure 61. Cross section image taken on carbon steel specimen (CS1018) of the bulk solution at 80°C and pCO<sub>2</sub> 0.5 bar with 10000 ppm Ca<sup>2+</sup> (a) pH 6.6 (b) and pH 5.3.

Figure 62 corresponds to SEMs of sample surfaces after the corrosion product layer was removed with Clarke solution [41]. As is shown, the surface of the samples corresponding to the tested conditions revealed non-uniform corrosion attack.

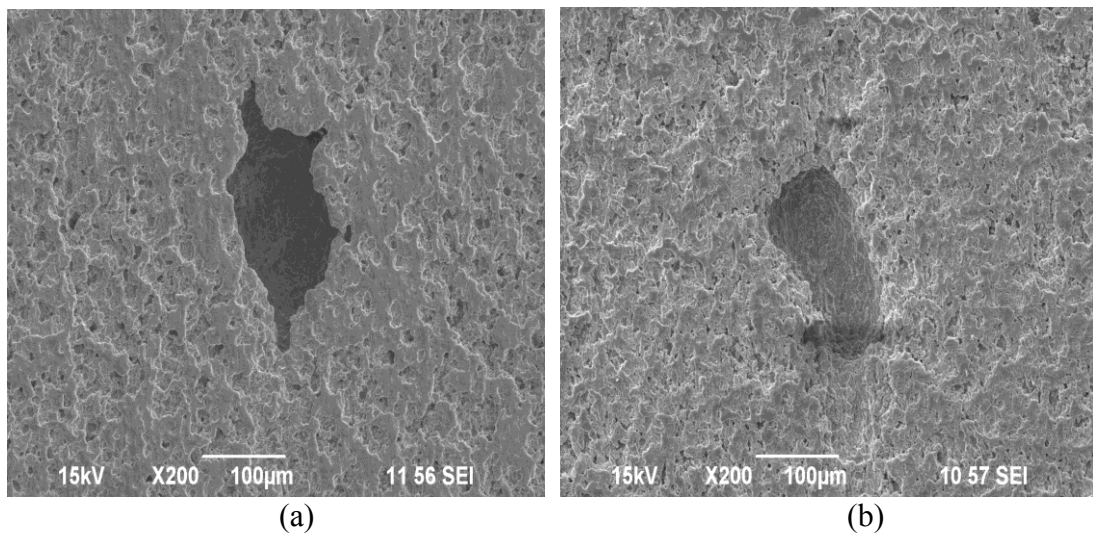


Figure 62. Surfaces after corrosion product removal of the carbon steel specimen (CS1018) surface of the bulk solution at 80°C and pCO<sub>2</sub> 0.5 bar with 10,000 ppm Ca<sup>2+</sup> (a) pH 6.6 (b) and pH 5.3.

Figure 63 corresponds to the IFM data for samples with the corrosion product layer removed from the surface. The pitting corrosion rate was calculated according to the maximum measured depth of pits and is shown in Table 8.

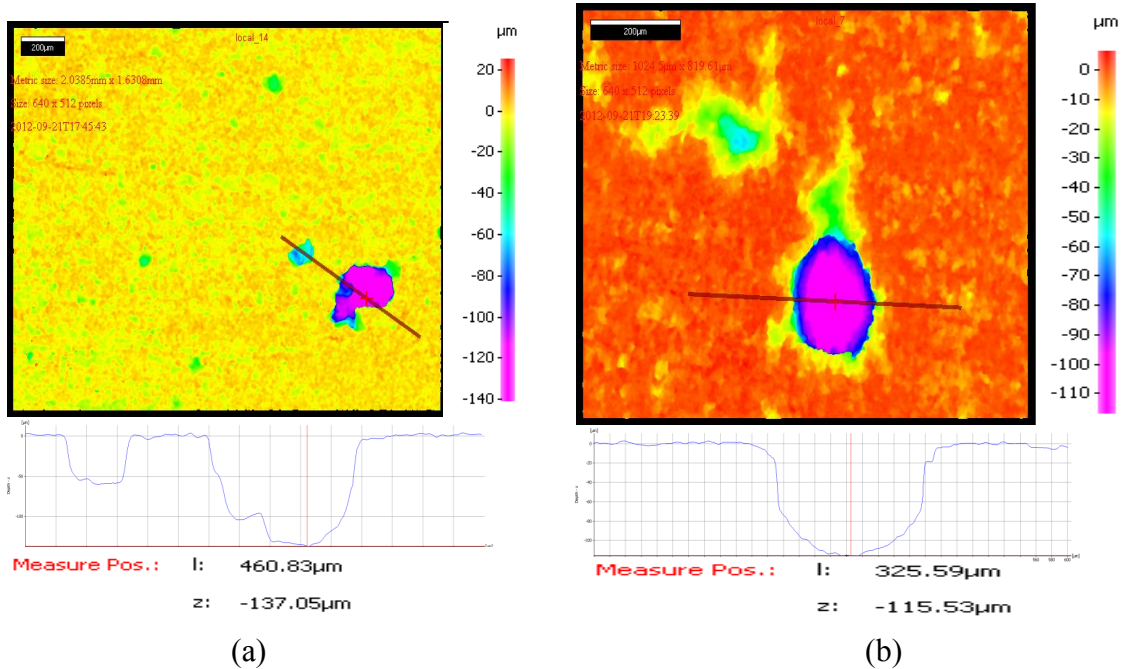


Figure 63. IFM of carbon steel specimen (CS1018) after removal of corrosion product for the experiment conducted at 80°C and pCO<sub>2</sub> 0.5 bar with different initial pH (a) pH 6.6 (b) pH 5.3.

Table 8. Corresponded data to the tests with 10,000 ppm Ca<sup>2+</sup> with different initial pH.

Initial pH	Depth of Pit / (μm)	Pitting CR / (mm/yr)	Weight Loss CR / (mm/yr)	Pitting Ratio
6.6	137	8.3	0.9	8.7
5.3	115	7.2	0.8	8.7

Figure 64 and Figure 65 represent the specimen XRD data for the tested conditions. As is shown, in spite of the different surface morphology of the formed layer in Figure 59, the XRD patterns are consistent with formation of  $\text{CaCO}_3$  on the surface. Note that more line broadening is observed for the higher pH experiment, consistent with great compositional inhomogeneity of incorporated Fe in the calcite lattice. Also, a little  $\text{FeCO}_3$  present in the low pH experiment.

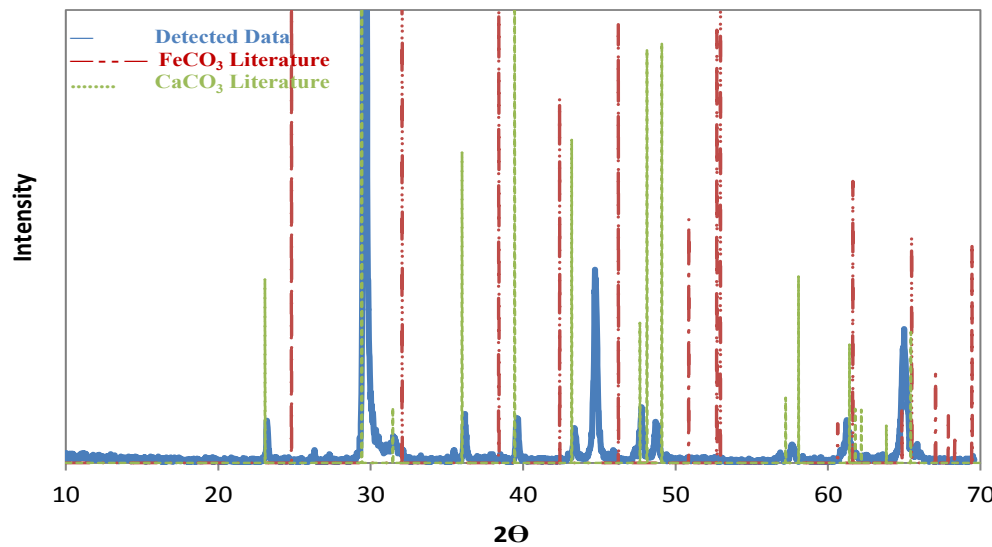


Figure 64. XRD data of recovered carbon steel specimen (CS1018) from bulk solution at 80°C and  $\text{pCO}_2$  0.5 bar with 10,000 ppm  $\text{Ca}^{2+}$  with initial pH 6.6.

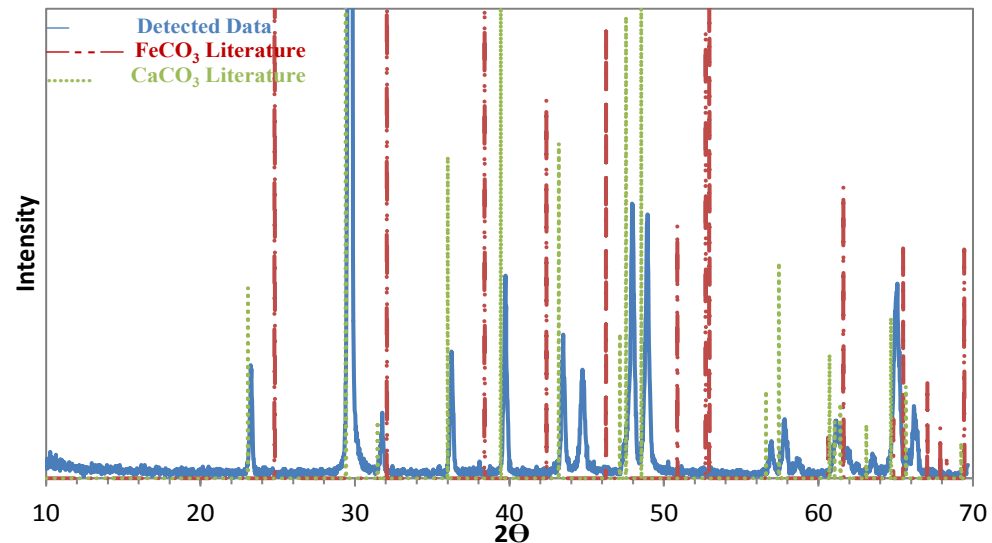


Figure 65. XRD data of recovered carbon steel specimen (CS1018) from bulk solution at 80°C and  $\text{pCO}_2$  0.5 bar with 10,000 ppm  $\text{Ca}^{2+}$  with initial pH 5.3.

According to the results obtained from the initial 10,000 ppm  $\text{Ca}^{2+}$  experiment with either a high or low initial iron carbonate saturation degree, the non-uniform corrosion behavior occurred regardless of the initial pH.

### **Quantitative XRD analysis**

By using the XRD data in Figure 14, Figure 15, Figure 16, Figure 17, Figure 18, Figure 64 and Figure 65 the concentration of  $\text{Ca}^{2+}$  in the structure of the solid solution can be calculated. Figure 67 shows the hexagonal Bravais lattice corresponding to the fundamental crystal structure of  $\text{FeCO}_3$ ,  $\text{CaCO}_3$  and  $\text{Ca}_x\text{Fe}_y\text{CO}_3$  ( $x+y=1$ ); each phase is isostructural(calcite-type). Figure 66 shows the calcite and siderite structure.. The “a” and “c” unit cell parameters can be calculated using Equation (29) [46]. The “d” in Equation (29) is calculated from Bragg’s law in Equation (30) [46]. Using h, k, and l values, or Miller indices corresponding to particular lattice planes, and the XRD data using calculated “d” values from Equation (30) , “a” and “c” unit cell edges can be calculated. Assuming linear behavior [47], [48] for  $\text{Ca}^{2+}$  incorporation in the solid solution structure *versus* the unit cell parameters, x can be found from the plotted x value *versus* either of the unit cell parameters. Figure 68 shows the plotted x value versus “c” for the pure  $\text{FeCO}_3$  and  $\text{CaCO}_3$  literature data [49]. The calculated unit cell parameter “c” for each tested condition is located on the line in Figure 68 and the corresponding x value determined. The red points are extracted data from the literature [48], which confirms the accuracy of the calculated data. As was shown in Figure 17 the 1,000 ppm  $\text{Ca}^{2+}$  experiment has two peaks. This is consistent with the presence of two layers on the surface of the sample. The second layer has the same concentration of  $\text{Ca}^{2+}$  as the

experiment with 10,000 ppm  $\text{Ca}^{2+}$ , thus the points are overlapped. The obtained results are listed in Table 9.

The same procedure was followed to calculate the unit cell parameters and consequently the concentration of  $\text{Ca}^{2+}$  in the structure of the solid solution for the experiments with the initial 10,000 ppm  $\text{Ca}^{2+}$  and different initial pH. The results are plotted in Figure 69 and summarized in Table 10.

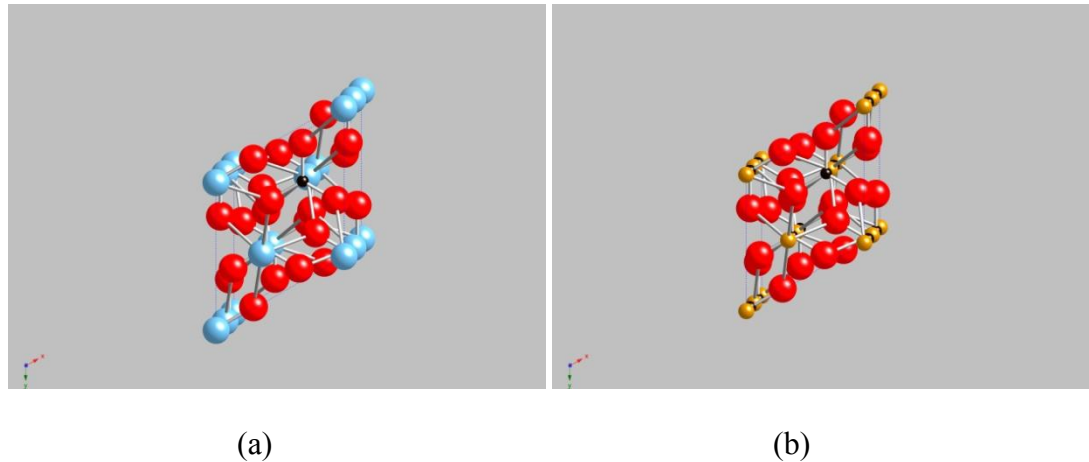


Figure 66. lattice image of (a) calcite ( $\text{CaCO}_3$ ; blue = Ca, red = O, black =C) (b) siderite ( $\text{FeCO}_3$ ; tan = Fe, red = O, black =C).

$$\frac{1}{d^2} = \frac{4}{3} \left( \frac{h^2 + hk + k^2}{a^2} \right) + \frac{l^2}{c^2} \quad (15)$$

$$d = \frac{n\lambda}{2 \sin \theta} \quad (30)$$

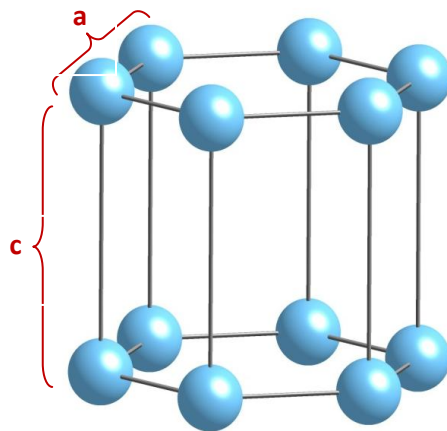


Figure 67. Hexagonal unit cell.

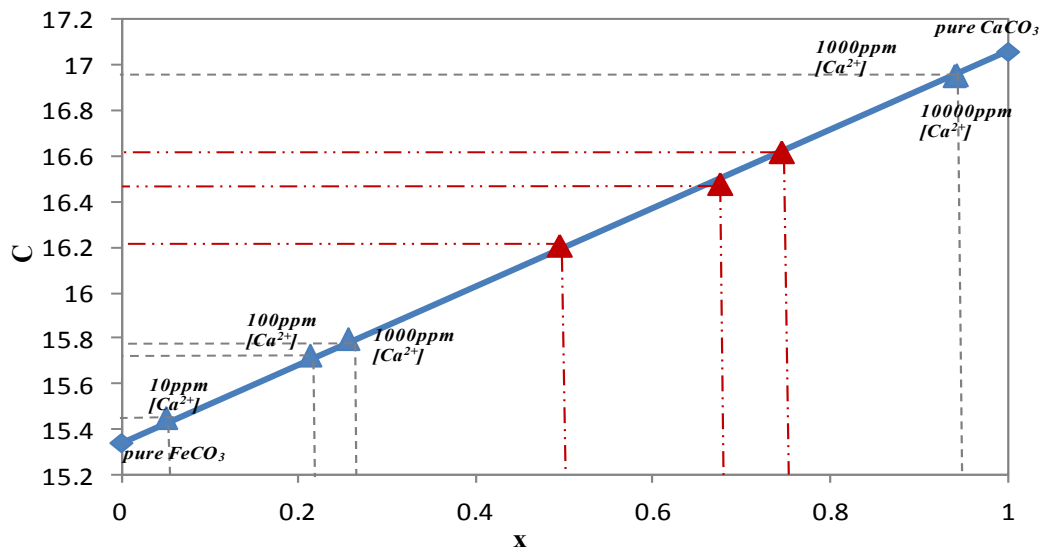


Figure 68. Unit cell parameter  $c$  versus the concentration of  $Ca^{2+}$  in the structure of solid solution for experiments with different initial conditions of 0, 10, 100, 1000, 10000 ppm  $Ca^{2+}$ .

The quantitative analysis of XRD data are summarized in Table 9 and Table 10.

Although the analyses in Table 9 do not show any specific trends relating general

corrosion behavior to  $\text{Ca}^{2+}$  concentration in the corrosion product solid solution, they revealed that when the concentration of  $\text{Ca}^{2+}$  is above 90% therein the steel surface suffers from localized attack. These results are confirmed in Table 10. Note that the calculated concentrations from EDS spectra, Table 9, are in a good agreement with the obtained data from XRD.

Table 9. Composition of the solid solution for the experiments with different initial  $\text{Ca}^{2+}$ .

Initial $\text{Ca}^{2+}/\text{ppm}$	Calculated $x$ <i>from XRD Data</i>	Calculated $x$ from <i>EDS Spectra</i>	$\text{Ca}_x\text{Fe}_{(1-x)}\text{CO}_3$	Weight Loss Corrosion Rate / (mm/yr)	Pitting
10	0.05	0.045	$\text{Ca}_{0.05}\text{Fe}_{0.95}\text{CO}_3$	0.6	-
100	0.22	0.22	$\text{Ca}_{0.22}\text{Fe}_{0.78}\text{CO}_3$	NA	-
1,000	0.25	-	$\text{Ca}_{0.25}\text{Fe}_{0.75}\text{CO}_3$	1.3	-
	0.94	-	$\text{Ca}_{0.94}\text{Fe}_{0.06}\text{CO}_3$		-
10,000	0.94	0.91	$\text{Ca}_{0.94}\text{Fe}_{0.06}\text{CO}_3$	0.7	✓

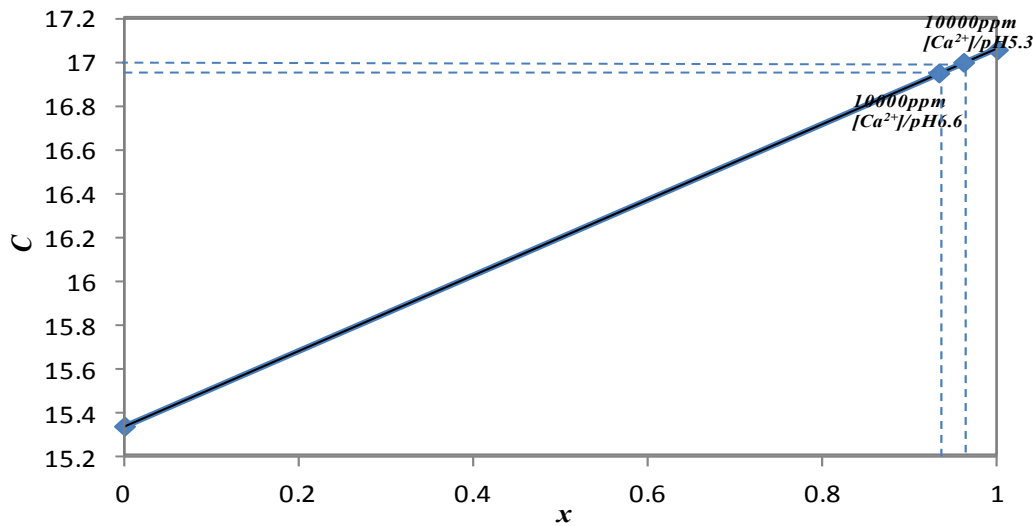


Figure 69. Unit cell parameter “c” versus concentration of  $\text{Ca}^{2+}$  in the structure of corrosion products for experiments with 10,000 ppm  $\text{Ca}^{2+}$  and initial pH values of 5.3 and 6.6.

Table 10. Composition of the solid for 10,000 ppm  $\text{Ca}^{2+}$  experiments with different initial pH.

Initial pH	Calculated $x$ from XRD Data	Calculated $x$ from EDS Spectra	$\text{Ca}_x\text{Fe}_{(1-x)}\text{CO}_3$	Weight Loss Corrosion Rate / (mm/yr)	Pitting
6.6	0.93	0.91	$\text{Ca}_{0.93}\text{Fe}_{0.07}\text{CO}_3$	0.9	✓
5.3	0.96	0.90	$\text{Ca}_{0.96}\text{Fe}_{0.04}\text{CO}_3$	0.8	✓

## CHAPTER 5: CONCLUSIONS AND FUTURE WORK

### **Conclusions**

Based on the obtained results from these experiments:

- The presence of  $\text{Ca}^{2+}$  affects the corrosion behavior as it changes the water chemistry.
- $\text{Ca}^{2+}$  concentrations below 100 ppm did not affect the corrosion rate.
- At high concentration of  $\text{Ca}^{2+}$  ( $\geq 1,000$  ppm) the corrosion behavior was dramatically different.
- At 10,000 ppm, the presence of  $\text{Ca}^{2+}$  may cause pitting.
- $\text{CaCO}_3$  is not nearly as protective as  $\text{FeCO}_3$ .
- The presence of chlorides did not have an effect on the non-uniform corrosion.
- The non-uniform behavior of corrosion at 10,000 ppm  $\text{Ca}^{2+}$  occurred regardless of the initial pH used in the experiments.

### **Future work**

For any future work the following is recommended.

- Low Pressure  $\text{CO}_2$ 
  - ❖ Studying the effect of  $\text{Ca}^{2+}$  on corrosion in the presence of  $\text{H}_2\text{S}$ , since the corrosion mechanism in the presence of  $\text{H}_2\text{S}$  is different
  - ❖ Studying the effect of  $\text{Ca}^{2+}$  on corrosion in flowing solutions.
- High Pressure  $\text{CO}_2$

- ❖ Study the effect of  $\text{Ca}^{2+}$  on  $\text{FeCO}_3$  formation at different  $\text{Ca}^{2+}$  concentrations at higher pressure  $\text{CO}_2$  (80 to 100 bar).
- Due to the isostructularity between  $\text{MgCO}_3$  and  $\text{FeCO}_3$ , studying the effect of  $\text{Mg}^{2+}$  on  $\text{CO}_2$  corrosion is recommended.

## REFERENCES

- 1 B. Zerai, B. Z. Saylor, and G. Matisoff, “Computer simulation of CO<sub>2</sub> trapped through mineral precipitation in the Rose Run Sandstone, Ohio.” *Applied Geochemistry*, vol. 21, pp. 223–240, Feb. 2006.
- 2 J. E. Wajon, G. E. Ho, and P. J. Murphy, “Rate of precipitation of ferrous iron and formation of mixed iron-calcium carbonates by naturally occurring carbonate materials,” *Water Research*, vol. 19, pp. 831–837, Jan. 1985.
- 3 J. Gale and J. Davison, “Transmission of CO<sub>2</sub>—safety and economic considerations.” *Energy*, vol. 29, pp. 1319–1328, Jul. 2004.
- 4 A. Pfennig and A. Kranzmann, “Reliability of pipe steels with different amounts of C and Cr during onshore carbon dioxide injection.” *International Journal of Greenhouse Gas Control*, vol. 5, pp. 757–769, Jul. 2011.
- 5 D. Young, Y.S. Choi, and S. Nešić, “Review of wellbore integrity and corrosion of carbon steel in CO<sub>2</sub> geologic storage environments.” in Proc. NACE, 2011.
- 6 S. Nešić, “Key issues related to modeling of internal corrosion of oil and gas pipelines – A review.” *Corrosion Science*, vol. 49, pp. 4308–4338, Dec. 2007.
- 7 J. N. Butler, “Carbon dioxide equilibria and their applications,” 1<sup>st</sup> ed. Chelsea, LEWIS, 1981, pp. 1-40.
- 8 A. M. Nor, M. F. Suhor, M.F. Mohamed, M. Singer and S. Nešić, “Corrosion of carbon steel in high CO<sub>2</sub> environment: flow effect.” in Proc. NACE, 2011, pp. 1–18.
- 9 Y.S. Choi and S. Nešić, “Corrosion behavior of carbon steel in supercritical CO<sub>2</sub>-water environments.” in Proc. NACE, 2009, pp. 1–20.

- 10 M. Gao, X. Pang, and K. Gao, “The growth mechanism of CO<sub>2</sub> corrosion product films,” *Corrosion Science*, vol. 53, pp. 557–568, Oct. 2010.
- 11 S. Nešić, M. Nordsveen, R. Nyborg, and A. Stangeland “A mechanistic model for carbon dioxide corrosion of mild steel in the presence of protective iron carbonate films — part 2 : a numerical experiment.” *Corrosion Science*, vol. 59, pp. 489–497, Jun. 2003.
- 12 A. Dugstad, “Mechanism of protective film formation during CO<sub>2</sub> corrosion of carbon steel,” in Proc. *NACE*, 1998, pp. 1–11.
- 13 R. Nyborg, “Initiation and growth of mesa corrosion attack during CO<sub>2</sub> corrosion of carbon steel,” in Proc. *NACE*, 1998, pp. 1–11.
- 14 J. Han, Y. Yang, B. Brown, and S. Nešić, “Electrochemical investigation of localized CO<sub>2</sub> corrosion on mild steel.” in Proc. *NACE*, 2007, pp. 1–25.
- 15 J. K. Heuer, and J. F. Stubbins, “An XPS characterization of FeCO<sub>3</sub> films from CO<sub>2</sub> corrosion,” *Corrosion Science*, vol. 41, pp. 1231–1243, 1999.
- 16 M. Nordsveen, S. Nešić, R. Nyborg, and A. Stangeland “A mechanistic model for carbon dioxide corrosion of mild steel in the presence of protective iron carbonate films — part 1 : theory and verification.” *Corrosion Science*, vol. 59, pp. 443–456, Dec. 2002.
- 17 W. Sun and S. Nešić, “Basics revisited: kinetics of iron carbonate scale precipitation in CO<sub>2</sub> corrosion.” in Proc. *NACE*, 2006, pp. 1–21.
- 18 S. Nešić, “Carbon Dioxide Corrosion of Mild Steel,” in *Uhlig’s Corrosion Handbook*, 2011, pp. 229–245.
- 19 M. B. Kermani and A. Morshed, “Carbon dioxide corrosion in oil and gas production—a compendium,” *Corrosion*, vol. 59, pp. 659–683, 2003.

- 20 S. Nešić, and L. Lunde, “Carbon dioxide corrosion of carbon steel in two-phase flow,” *Corrosion Science*, vol. 50, pp. 717–727, 1994.
- 21 R. De Marco, Z. T. Jiang, B. Pejcic, and E. Poinen, “An in situ synchrotron radiation grazing incidence X-ray diffraction study of carbon dioxide corrosion,” *Journal of The Electrochemical Society*, vol. 152, pp. B389, Aug. 2005.
- 22 G. F. Lin, M. S. Zheng, Z. Q. Bai, and Y. R. Feng “Wear resistance of CO<sub>2</sub> corrosion product scale formed at high temperature,” *J. Iron & Steel Res. , Int.* , vol. 13, pp. 47–52, 2006.
- 23 G. Schmitt, and M. Hörstemeier, “Fundamental aspects of CO<sub>2</sub> metal loss corrosion – part II: Influence of different parameters on CO<sub>2</sub> corrosion mechanisms,” in Proc. *NACE*, 2006, pp. 1–26.
- 24 F. Yu, K. W. Gao, Y. J. Su, J. X. Li, L. J. Qiao, W. Y. Chu, and M. X. Lu, “The fracture toughness of CO<sub>2</sub> corrosion scale in pipeline steel,” *Materials Letters*, vol. 59, pp. 1709–1713, Jan. 2005.
- 25 B. Ingham, M. Ko, N. Laycock, J. Burnell, P. Kappen, J. A. Kimpton, and D. E. Williams, “In situ synchrotron X-ray diffraction study of scale formation during CO<sub>2</sub> corrosion of carbon steel in sodium and magnesium chloride solutions,” *Corrosion Science*, vol. 56, pp. 96–104, Dec. 2011.
- 26 D. Postma, “Formation of siderite and vivianite and the pore-water composition of recent bog sediment in Denmark.” *Chemical Geology*, vol. 31, pp. 225–244, 1981.

- 27 T. Li, Y. Yang, K. Gao, and M. Lu, "Mechanism of protective film formation during CO<sub>2</sub> corrosion of X65 pipeline steel," *Journal of University of Science and Technology Beijing*, vol. 15, pp. 702–706, Dec. 2008.
- 28 C. A. Palacios, and J. R. Shadley, "Characteristics of corrosion scales on steels in a CO<sub>2</sub>-saturated NaCl brine," *Corrosion*, vol. 47, pp. 122–127, Feb. 1991.
- 29 Z. D. Cui, S. L. Wu, S. L. Zhu, and X. J. Yang, "Study on corrosion properties of pipelines in simulated produced water saturated with supercritical CO<sub>2</sub>," *Applied Surface Science*, vol. 252, pp. 2368–2374, May. 2005.
- 30 L. N. Plummer and E. Busenberg, "The solubilities of calcite, aragonite and vaterite in CO<sub>2</sub>-H<sub>2</sub>O solutions between 0 and 90° C, and an evaluation of aqueous model for the system CaCO<sub>3</sub>-CO<sub>2</sub>-H<sub>2</sub>O." *Geochimica et Cosmochimica Acta*, vol. 46, pp. 1011–1040, Feb. 1982.
- 31 E. Eriksrud, and T. Sontvedt, "Effect of flow on CO<sub>2</sub> corrosion rates in real and synthetic formation waters." in Proc. *NACE*, 1984, pp. 20–38.
- 32 G. Zhao, X. Lu, J. Xiang, and Y. Han, "Formation characteristic of CO<sub>2</sub> corrosion product layer of P110 steel investigated by SEM and electrochemical techniques." *J. Iron & Steel Res., Int.*, vol. 16, pp. 89–94, Jul. 2009.
- 33 G. Zhao, J. L I, S. Hao, X. L U, and H. L I "Effect of Ca<sup>2+</sup> and Mg<sup>2+</sup> on CO<sub>2</sub> corrosion behavior of tube steel." *J. Iron & Steel Res., Int.*, pp. 35–53, Jan. 2005.
- 34 X. Jiang, Y. G. Zheng, D. R. Qu, and W. Ke, "Effect of calcium ions on pitting corrosion and inhibition performance in CO<sub>2</sub> corrosion of N80 steel," *Corrosion Science*, vol. 48, pp. 3091–3108, Oct. 2006.

- 35 C. Ding, K-W. Gao, and C-F. Chen, "Effect of  $\text{Ca}^{2+}$  on  $\text{CO}_2$  corrosion properties of X65 pipeline steel," *International Journal of Minerals, Metallurgy and Materials*, vol. 16, pp. 661–666, Dec. 2009.
- 36 C. Q. Ren, X. Wang, L. Liu, H. E. Yang, and N. Xian, "Lab and field investigations on localized corrosion of casing," *Materials and Corrosion*, vol. 63, pp. 168–172, Feb. 2012.
- 37 Z. F. Yin, W. Z. Zhao, Y. R. Feng, and S. D. Zhu, "Characterization of  $\text{CO}_2$  corrosion scale in simulated solution with  $\text{Cl}^-$  ion under turbulent flow conditions," *Corrosion Engineering, Science and Technology*, vol. 44, pp. 453–461, Dec. 2009.
- 38 S. D. Zhu, J. F. Wei, Z. Q. Bai, G. S. Zhou, J. Miao, and R. Cai, "Failure analysis of P110 tubing string in the ultra-deep oil well," *Engineering Failure Analysis*, vol. 18, pp. 950–962, Apr. 2011.
- 39 K. Gao, F. Yu, X. Pang, G. Zhang, L. Qiao, W. Chu, and M. Lu, "Mechanical properties of  $\text{CO}_2$  corrosion product scales and their relationship to corrosion rates," *Corrosion Science*, vol. 50, pp. 2796–2803, Oct. 2008.
- 40 D. A. Jones, "Principles and Prevention of Corrosion." in *Chem. and Metal. Eng.*, 2<sup>nd</sup> ed., NJ: Prentice-Hall, 1996, ch. 3, pp. 75–115.
- 41 Standard Practice for Preparing, Cleaning, and Evaluating Corrosion Test, ASTM Standard, Reapproved 1999.
- 42 Standard Guide for Examination and Evaluation of Pitting Corrosion 1, ASTM Standard Reapproved 1999.
- 43 M. Singer, D. Hinkson, Z. Zhang, H. Wang, and S. Nešić, " $\text{CO}_2$  top of the line corrosion in presence of acetic acid, a parametric study," in Proc. *NACE*, 2009.

- 44 B. Brown, "Corrosion product film characteristics in H<sub>2</sub>S / CO<sub>2</sub> corrosion," ICMT, Athens, OH, Tech. Rep. Nov. 2010.
- 45 T. Tanupabrungsun, D. Young, B. Brown, and S. Nešić, "Construction and verification of pourbaix diagrams for CO<sub>2</sub> corrosion of mild steel valid up to 250°C," in Proc. *NACE*, 2012.
- 46 A. R. West, *Solid state chemistry and its applications*. Aberdin, Scotland: John Wiley & Sons, 1998, pp. 694.
- 47 L. Chai, and A. Navrotsky, "Synthesis, characterization, and enthalpy of mixing of the (Fe,Mg)C0<sub>3</sub> solid solution," *Geochimica et Cosmochimica Acta*, vol. 60, pp. 4377–4383, Nov. 1996.
- 48 P. M. Davidson, G. H. Symmes, B. A. Cohen, R. J. Reeder, and D. H. Lindsley, "Synthesis of the new compound CaFe (CO<sub>3</sub>)<sub>2</sub> and experimental constraints on the (Ca,Fe)CO<sub>3</sub> join," *Geochimica et Cosmochimica Acta*, vol. 58, pp. 5105–5109, 1994.
- 49 "Mineralogy Database," 2012. [Online]. Available: <http://webmineral.com/>
- 50 J. W. Morse, and W. H. Casey, "Ostwald processes and mineral paragenesis in sediment," *American Journal of Science*, vol. 288, pp. 537–560, Jun. 1988.
- 51 J. W. Morse, R. S. Arvidson, and A. Lüttge, "Calcium carbonate formation and dissolution," *Chemical reviews*, vol. 107, pp. 342–81, Feb. 2007.

## APPENDIX 1: KINETIC STUDY OF THE SCALE FORMATION

In the process of each experiment the first sample was taken out after 4 days for the initial surface analysis. The second and third samples were taken out at the end of each experiment at day 7<sup>th</sup>. Among all tested conditions the experiment with 1,000 ppm Ca<sup>2+</sup> showed a different morphology of crystals for day 4<sup>th</sup> and 7<sup>th</sup>.

In nucleation process, as it was reported by Morse and Casey, the Ostwald step rule says, the first formed product is less stable and as it goes through the unstable phases it turns to a stable form [50].

Figure 70 (a) shows the morphology of the crystals contain the elongated form, which according to literature stands for the formation of aragonite [51]. The XRD diffraction in Figure 71 proves the formation of aragonite along with Fe<sub>x</sub>Ca<sub>y</sub>CO<sub>3</sub> ( $x+y=1$ ). However, the surface of the sample after 7 days in Figure 70 (b) does not have the elongated form of crystals. Figure 66 shows the XRD diffraction for the sample at the end of experiment. There is no sign of aragonite on the surface of the sample. However, calcite along with Fe<sub>x</sub>Ca<sub>y</sub>CO<sub>3</sub> ( $x+y=1$ ) was detected on the surface after 7 days.

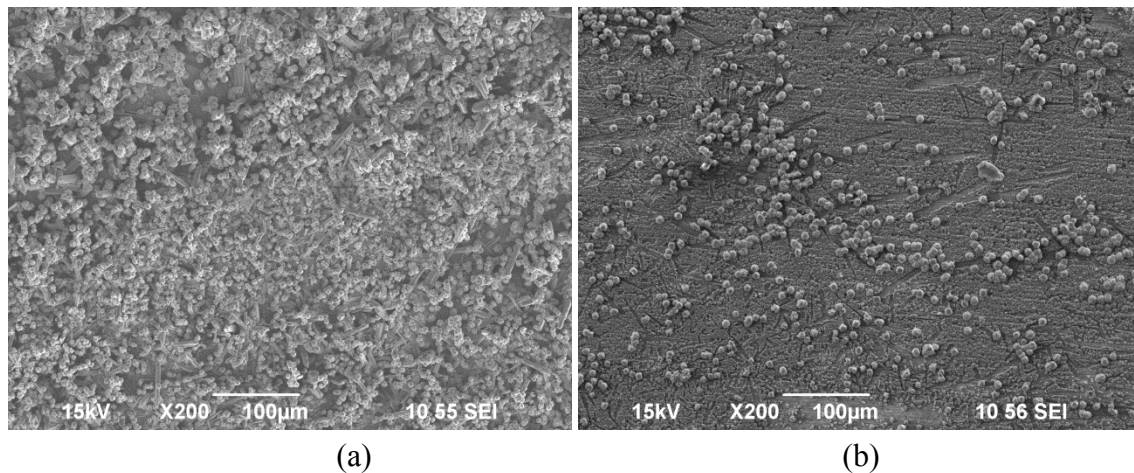


Figure 70. SEM images taken on carbon steel specimen (CS1018) surface of the bulk solution with 10,000 ppm  $\text{Ca}^{2+}$  and initial pH 6.6 at 80°C,  $\text{pCO}_2$  0.5 bar and 10 ppm  $\text{Fe}^{2+}$  and 1,000 ppm  $\text{Ca}^{2+}$  (a) after 4 days, (b) after 7 days.

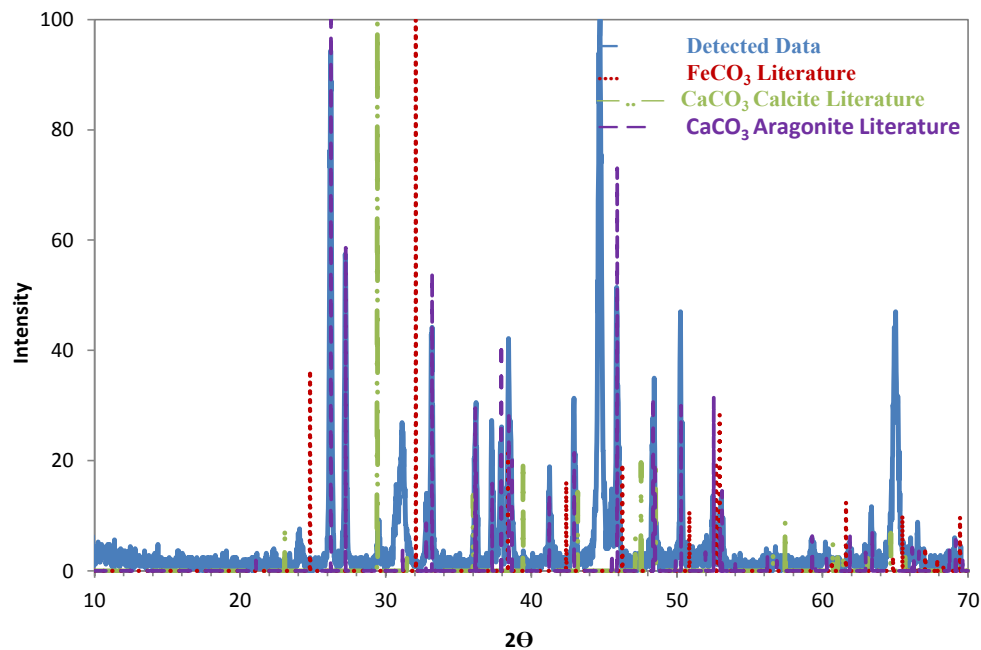


Figure 71. XRD data taken on carbon steel specimen (CS1018) surface of the bulk solution with 10,000 ppm  $\text{Ca}^{2+}$  and initial pH 6.6 at 80°C,  $\text{pCO}_2$  0.5 bar and 10 ppm  $\text{Fe}^{2+}$  and 1,000 ppm  $\text{Ca}^{2+}$  after 4 days.

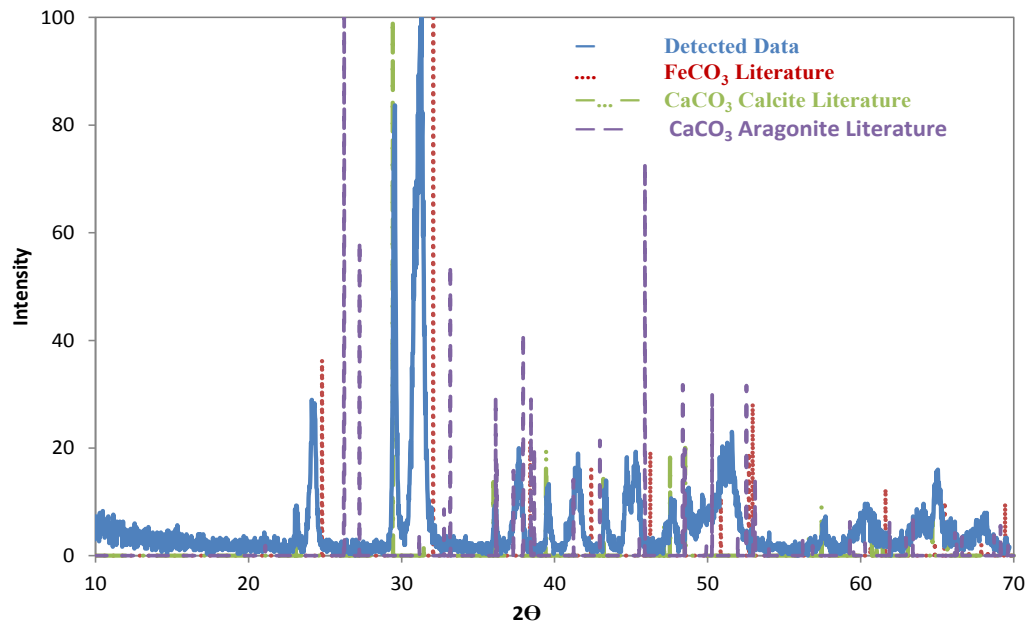


Figure 72. XRD data taken on carbon steel specimen (CS1018) surface of the bulk solution with 10,000 ppm  $\text{Ca}^{2+}$  and initial pH 6.6 at 80°C,  $\text{pCO}_2$  0.5 bar and 10 ppm  $\text{Fe}^{2+}$  and 1,000 ppm  $\text{Ca}^{2+}$  after 7 days.



Thesis and Dissertation Services